Experimental Investigation Of Free-Space Optical Routing Systems Using Static And Dynamic Binary Holographic Elements

Andrew John Stevens

Submitted for the degree of PhD.

Department of Physics & Astronomy
The University of Edinburgh

1995

Abstract

Many optical systems require free-space routing to direct signals to modulators, detectors, or output channels. As one of the main advantages of optics is the high degree of parallelism achievable in optical systems, it is often desirable to increase the number of channels or beams in a system, whether the system performs image recognition, optical computing, or telecommunications switching. However there are many factors which limit the scalability of the optical interconnects which provide optical multiplexing/demultiplexing and beam routing functions. Fixed optical interconnection may be achieved by passive elements such as binary phase holograms, Fresnel lenses, and microlens arrays. However, more complex dynamic interconnects require an active element to perform the optical switching. This active element is commonly a Spatial Light Modulator (SLM).

In this thesis a fabrication technique for manufacturing passive binary phase holograms is presented. This technique utilises standard microfabrication technology to produce the required phase patterns in silicon nitride deposited on a sapphire substrate. The robust process results in a high yield of elements showing near optimum performance. Diffraction efficiencies of 77% have been achieved with wafers containing 32 holograms showing almost identical optical performance. This high yield compares very favourably to those of other fabrication techniques.

Two prototype dynamic optical routing systems are then discussed. The first experimental test system models a 256 channel optical crossbar, using cascaded binary phase holograms manufactured using the aforementioned process, and a planarised 256×256 pixel ferroelectric liquid crystal over silicon SLM which acts as the switching element. The second optical system uses the same device to act as a dynamic holographic element which routes one beam into any one or many of an array of eight output fibres.

The scalability of these routing systems is critically dependant upon both the performance of the spatial light modulators and other passive elements in the system. The performance of all the critical elements is assessed, and the results used to discuss the scalability of these systems. The results are also used to draw conclusions about the performance requirements for full implementations of the test systems. Finally, the performance of crossbars and dynamic holographic routing systems, implemented using ferroelectric liquid crystal over silicon spatial light modulators, are compared and conclusions drawn about the applications of each type of system.

Declaration

I declare that the composition of this thesis, and all of the work described within it, was carried out by me, except where otherwise acknowledged.

28th August 1995

Acknowledgements

First, I wish to thank my supervisers; Will Hossack, for his practical help and advice, and David Vass for his enthusiastic support and assistance in finding the money to support my work. Tom Stevenson, from the Department of Electrical Engineering, also deserves a special mention for acting as my mentor whilst working in the microfabrication laboratory.

The expert technical support of Andrew Garrie, Andrew Downie, and Peter Tuffy are also gratefully acknowledged.

During my three years with the Applied Optics Group, almost everyone has helped me or given me advice at some point, and I would like to thank them all. The following people deserve a special credit:

Peter McCowan for his advice and company when I first started.

James Gourlay for his help and for acting as a catalyst for my ideas during many coffee breaks.

Mike Snook for his cynical wit and knowledge of all things associated with VLSI silicon.

George Bodammer for keeping such an ordered library of research papers.

Sergei Samus, for developing such fine hologram design software, and for telling such hilarious Russian jokes.

Finally I must thank EPSRC for funding my PhD studentship.

Contents

Chapter 1

Introduction

1.1 Background

As computer systems become larger and more powerful and global telecommunications networks come into operation, the limitations of electronics are becoming more evident. The high-bandwidth signals are prone to noise, crosstalk, and attenuation over long distances. Photonics has become recognised as an alternative to electronics since by their very nature photons are less susceptible to many of the problems encountered by electrons. Photons, which are neutral bosons, do not suffer from crosstalk and can propagate through matter with little attenuation occuring. However charged electrons interact strongly with matter and each other due to Coulomb Forces. Low power laser sources and detectors already allow most long distance telecommunications signals to be transmitted optically at high data rates through fibre optic cables. However optics is much more powerful than a simple means of transmitting information at high data rates. Powerful optical systems can be constructed which perform tasks such as image/target recognition, data processing and optical computing, taking advantage of the massive inherent parallelism of optics.

In order for these complex optical systems to be developed further, and for optics to become the major information transport mechanism of the future, it is necessary for optical routing elements/networks to be developed which can

interconnect optical fibres, electro-optic devices and optical sub-systems. As optical systems use more and more channels to achieve higher data throughput and greater processing power, optical interconnects need to be able to route not only single beams, but large arrays of beams. Two types of interconnect are required, passive elements which perform fixed routing operations on input beams or arrays of beams, and dynamic routing networks which can dynamically interconnect channels, changing the routing paths under the instruction of electrical or optical control signals. An important measure of the performance of a routing element is its scalability, i.e. how many input/output channels can be simultaneously routed by the element/network. This is vital as optical systems need to be able to operate on as many channels as possible in order to outperform electronics.

Passive elements can be fabricated from binary phase elements, using either Fresnel or Fourier diffraction to route the beams. The phase modulating pattern of these elements is generally optimised by computer algorithm and then fabricated using a variety of techniques such as photography or microfabrication processing. Dynamic routing networks are more complex as they require an active element. This element may be a *spatial light modulator*, which as its name suggests spatially modulates the phase, polarisation, or amplitude of the light. Many different types of spatial light modulator have been developed using several different modulating materials. The University of Edinburgh has pioneered the technology of ferroelectric liquid crystal over silicon spatial light modulators. These devices are at the forefront of spatial light modulator technology at present.

1.2 Objectives

The objectives of this project were as follows:

1. To develop a fabrication process for binary phase elements, which can be used to manufacture elements of high optical efficiency whilst retaining a high process yield.

2. To investigate dynamic free-space routing systems implemented using the 256×256 pixel ferroelectric liquid crystal over silicon spatial light modulator developed at The University of Edinburgh.

3. Using test systems, make an assessment of the scalability of free-space routing systems implemented using ferroelectric liquid crystal spatial light modulators, and consider their applications.

1.3 Thesis Outline

The following chapter reviews three major spatial light modulator technologies, digital micromirror devices, self-electro-optic-devices, and ferroelectric liquid crystal over silicon spatial light modulators. At present these devices show the most promise, for different applications, as spatial light modulators. The 256×256 pixel ferroelectric lquid crystal over silicon device which has been used in the experimental work presented in this thesis is described in some detail, and the planarisation process which has improved the performance of this device is discussed.

In Chapter 3 a fabrication technique for the manufacture of binary phase holograms will be presented, which uses the controlled deposition of silicon nitride on sapphire to produce the phase modulating layer. It will be shown that this technique produces optical elements with a high optical efficiency and a process yield much greater than any other published fabrication process.

In Chapters 4 and 5 experimental results of two free-space routing test systems will be presented. These systems are implemented using the 256×256 pixel ferroelectric liquid crystal over silicon spatial light modulator. In Chapter 4 a 256 channel crossbar test system will be described. This system uses the amplitude modulating properties of the spatial light modulator to perform the routing, whilst in Chapter 5 a system is presented which uses the phase modulating properties to route an input beam into one, several, or all the channels of a 4×2 output fibre array. In both of these chapters the performance and scalability of the systems is discussed, using the optical results to establish the critical elements in the systems.

Finally, in Chapter 6 the results presented in chapters 4 and 5 will be drawn together, and used to compare the two optical systems and to consider suitable applications of free-space routing systems implemented using ferroelectric over silicon spatial light modulators.

Chapter 2

FLC/Si SLMs

2.1 Introduction

A key element in the development of coherent optical systems is the Spatial Light Modulator (SLM). These devices provide a means of transferring information from the outside world into a coherent optical system. They perform this by spatially modulating the phase, amplitude, or polarisation of an optical wave, depending upon input information supplied to the device. This information may optically input in the case of an optically addressed SLM (OASLM) [1], or provided as electrical signals, an electrically addressed SLM (EASLM). It is the latter class of device which is used in the experimental work presented in this thesis, and so only EASLMs shall be discussed in this chapter. Although some *smart* devices allow both optical and electrical input [2][3].

In this chapter an overview of the major EASLM technologies being developed and a description of the operation of the Ferroelectric Liquid Crystal over Silicon Spatial Light Modulator (FLC/Si SLM) used within this thesis will be presented. A brief description of each technology will be given along with a discussion of its performance. However, should the reader require more detailed information, sufficient references will be supplied.

2.2 Spatial Light Modulator Technologies

Many different modulating materials and devices have been developed in recent years, using the optical, electrical, or magnetic properties of materials to spatially modulate light. Most of these materials/devices, with the exception of photorefractive crystals and acousto-optic modulators, are pixellated, and it is these pixellated devices which will be considered.

These include magneto-optic devices, Si-PLZT devices, electro-optic crystal devices, and adapted active matrix liquid crystal displays. For SLM review papers and descriptions of other SLM materials, the reader is directed to Applied Optics special issues on spatial light modulators [4][5].

Magneto-optic devices [6][7] are electrically addressed solid-state devices, which can operate in transmission or reflection. They operate by utilising the Faraday effect to rotate the polarisation of incident light. Pixels are etched into a magneto-optic substrate such as gallium garnate, and the magnetic domains are aligned perpendicularly to the film surface. The creation of a bistable magnetic domain in the pixel areas is achieved by applying an electrical current through the film via address lines. Arrays of 128×128 pixels have been fabricated, and are commercially available. Although these devices should theoretically exhibit high contrast ratios, in practice their performance is poor. Due to the high heat dissipation of these devices, cooling is required and parallel addressing difficult, reducing the frame rate.

Si/PLZT devices [8]-[11] use Lead Lathanum Zirconate Titanate (PLZT), which is a transparent, electro-optic, ferroelectric, ceramic material. Optical phase and amplitude modulation is achieved by applying an electric field across the PLZT material. This alters the refractive index of the material, modulating the phase. Amplitude modulation can then be achieved by placing the device between crossed polarisers. The electric field is applied by *flip-chip* bonding the PLZT substrate onto a silicon substrate. The mature silicon processing technology allows electrical processing and control circuitry to be easily realised, although large arrays of these devices have yet to be demonstrated.

There are a wide range of crystals and polymers which exhibit electro-optic effects such as the Pockels effect [12][13], many such materials are being investigated for use as spatial light modulators. Adapted liquid crystal displays will be briefly discussed in Section 2.3, and Table 2.2 in Section 2.7 summarises the performance of all the devices decribed in this chapter.

There are two types of device which, along with FLC/Si SLMs, offer the most potential (for different applications), and high degree of parallelism required for high performance optical systems. These devices are Digital-Micromirror-Devices (DMDs), and SElf Electro-optic Devices (SEEDs), and will be described in more detail.

2.2.1 Digital Micromirror Devices

The Digital Micromirror Devices (formerly known as Deformable Mirror devices), developed by Texas Instruments [14]-[17], consist of arrays of micromechanical mirrors which are monolithically fabricated onto silicon substrates. The mirrors are electrostatically deflected, and depending on how the mirror is hinged, can produce either phase (flexure beam) or amplitude (torsion beam) modulation. Cantilever hinges can produce both phase and amplitude modulation to some extent.

Torsion beam devices, as illustrated in Figure 2.1, allow the mirrors to be set in two directions, one position will reflect the incident light at an angle such that it propagates through an optical imaging system, whilst the other position reflects the light out of the system. Thus the pixels appear light or dark. Various pixel drive schemes have been considered, including Charge Coupled Device (CCD) technology and Static Random Access Memory (SRAM) technology [15].

Digital micromirror technology has been developed by Texas Instruments for use in projector systems. They have demonstrated a 768×576 SRAM pixel device which is capable of displaying PAL (Phase Alternation Line) broadcast quality pictures. Grey scale is made possible by Pulse Width Modulation (PWM) and colour is achieved by using separate red, green, blue light sources and time multiplexing of the image. Despite this being a mechanical device, impressive pixel switching

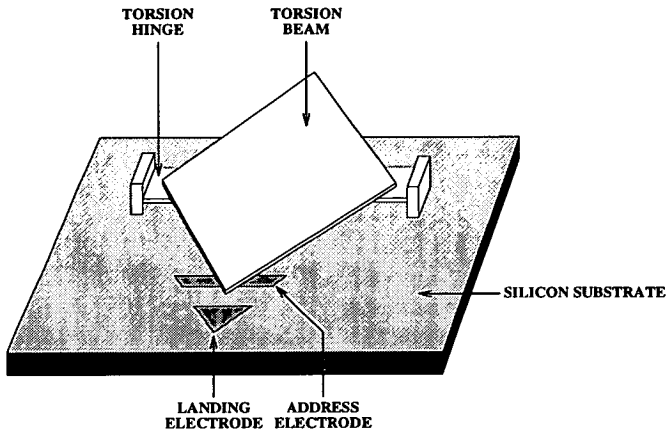

Figure 2.1: Digital Micromirror Device torsion beam pixel schematic.

speeds of 10μs have been achieved with contrast ratios of 50:1. This device and future work is fully described in [18].

Although these devices have been designed and constructed with specific products in mind i.e. projection display systems, they offer considerable promise in the role of general purpose SLMs, due to their high contrast ratio and relatively fast switching speed [19][20].

2.2.2 SEED Devices

These devices are Multiple-Quantum-Well (MQW) structures which make use of a non-linear effect known as the quantum confined Stark Effect (QSE). This effect describes the change in optical properties, particularly absorption, of MQW stacks when an electric field is applied perpendicularly to the stack layers. The MQW stack consists of between 50 and 200 very thin ($\approx$100Å) layers of alternating GaAs and $Al_xGa_{1-x}As$ grown by Molecular Beam Epitaxy (MBE). The QSE causes the absorption spectrum to feature steplike absorption edges. These result from the quantisation of the electrons and holes in the direction perpendicular to the stack layers. Initially the material is transparent to infra-red light of a chosen wavelength. However, when an electric field is applied across the MQW, the

absorption edges shift so that at the selected wavelength, generally 850nm, the material becomes opaque. The theory of MQW structures is explained more comprehensively in [21]. The spectral transmittance of a MQW structure is illustrated in Figure 2.2.

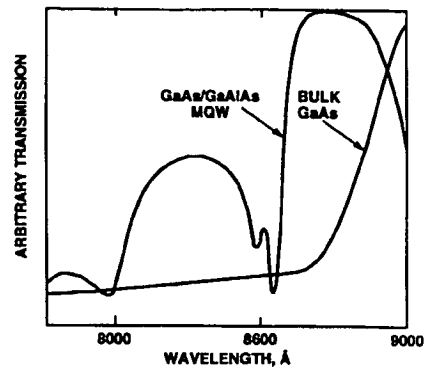

Figure 2.2: Spectral transmittance of a 200 period GaAs/$Ga_{0.72}Al_{0.28}As$ MQW, as illustrated in [21].

The QSE allows MQW structures to be placed inside p-i-n diode structures and act as optical I/O devices, known as SElf Electro-optic Devices (SEEDs). Such devices operate with an external electrical load. When illuminated, the induced photocurrent introduces a voltage drop across the load which in turn reduces the field across the MQW structure and this increases its absorption and photocurrent. This positive feedback reduces the transmittance of the device at one particular wavelength. The effect occurs almost instantaneously (pico-seconds)[21], giving rise to very fast switching times. However the contrast ratios are very poor at approximately 3:1 [22].

To help counteract this low contrast ratio, two SEED devices are often connected back to back as illustrated in Figure 2.3. This configuration is known as a Symmetric SEED (S-SEED). The devices can now switch between two stable states by changing the ratio of the optical inputs P_{in1} and P_{in2}. As the optical output is now a differential rather than absolute output, the low contrast ratio is less of a problem [21].

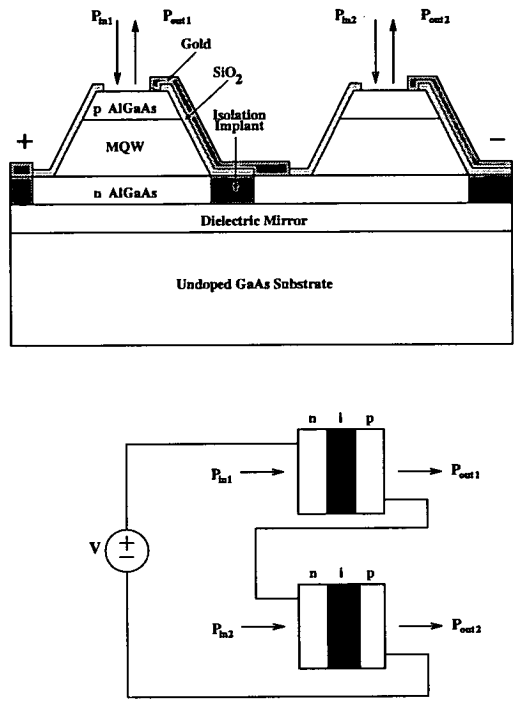

Figure 2.3: Schematic diagram of an S-SEED and the corresponding electrical circuit, as illustrated in [22].

Figure 2.3 also shows how the devices operate, with a dielectric reflector grown underneath the modulating device. Thus a double pass occurs with the MQW structure either absorbing or transmitting the light depending upon its state. It is possible to improve the contrast ratio of these devices by constructing the MQW structures within asymmetric Fabry-Perot cavities [21], although there are considerable fabrication problems with this at present.

Electrical input may be supplied by monolithographically integrating S-SEEDs with GaAs Field Effect Transistors (FET-SEEDs). AT&T Bell Laboratories are one of the major developers of SEED technology, developing them for use in telecommunication switching systems [23][24]. They have demonstrated a 32→16 channel free space switching network implemented using a 5 stage Banyan network. Each stage of the network consists of a 4×4 array of 2×1 multiplexers implemented using FET-SEED technology. This has been demonstrated with channels switching at 155Mbit/sec. [25].

AT&T Bell are also at the forefront of perhaps the most important development of SEED technology, that of *flip-chip bonding* SEED devices onto silicon VLSI substrates. This allows complex logic circuitry to be resident on each pixel, fabricated using the well characterised standard bulk silicon Complementary-Metal-Oxide-Semiconductor (CMOS) processes. The GaAs modulators can then be bonded on top of the silicon substrate using the flip-chip bonding technology and the GaAs substrate etched away, leaving islands of the modulating material. This is illustrated in Figure 2.4. This technology has recently been demonstrated on large arrays with high yields being achieved [26][27].

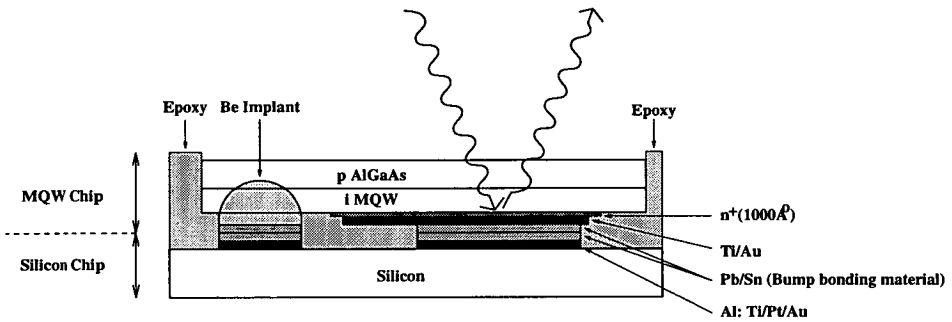

Figure 2.4: *Flip-Chip* bonded SEED devices on a Silicon VLSI substrate, as illustrated in [26].

Finally Martin Marietta Laboratories [28] recently presented a 128×128 pixel array of Flip-Chip bonded SEEDs on a silicon substrate used for providing electrical addressing circuitry. The SEED arrays are grown onto a transparent substrate and feature asymmetric Fabry-Perot cavities which have been optimised using a complex etching technique. This has allowed a contrast ratio of 25:1 to be achieved at a 100kHz frame rate, with a duty cycle of greater than 99%. A 512×512 pixel device has been planned.

It is obvious that the high speed of SEED devices coupled with large array sizes and reasonable contrast ratios makes such devices very suitable for digital optical systems such as telecommunications switching. Furthermore the use of CMOS logic at a pixel level to produce *smart* pixels and flip-chip bonding techniques allow the transition between optics and electronics to be simplified.

2.3 Ferroelectric Liquid Crystals

The development of liquid crystal (LC) materials has mainly been prompted by display manufacturers searching for a replacement for the cathode ray tube. Liquid crystal materials are suitable materials for flat panel displays due to their high birefringence, low switching energies, and low drive voltage requirements. From their name it is obvious that LC materials bridge the gap between the solid phase of matter and the liquid phase, with some short range positional ordering of the molecules. The molecules with the most interesting optical properties tend to be long stick-like molecules. The most common LC to be used in displays is the nematic LC. This material has no direct positional ordering, but the molecular axis does have a preferential direction so the molecules tend to lie with their long axes parallel. The optical switching properties of nematic LCs are well characterised and a full description of how optical modulation is achieved can be found in [29][30]. As nematic LCs rely on elastic relaxation to return to their unswitched state their switching speeds are too slow (10-100ms) for most SLM applications, but sufficient for display systems operating at less than 100Hz. However some work has been performed using adapted liquid crystal displays as spatial light modulators [31]. By removing the diffusing screen on the display and using the device as a transmissive element, or replacing the diffuser with a mirror and using it in reflection, high contrast ratios are possible. However the pixel fill-factor can still limit the performance, along with the switching speed.

This slow switching speed is overcome by using Ferroelectric Liquid Crystals (FLCs). These materials were first demonstrated in 1975 by Meyer [32] and exhibit a permanent non-zero electric polarisation known as the Spontaneous Polarisation (P_s). The orientation of this spontaneous polarisation can be changed by the application of an applied electric field resulting in fast (10-100μs) optical switching in which bistability can be observed [33]. These materials have been developed for high speed display applications [34]-[38], but are also extremely suitable materials for SLMs.

The most commonly used FLC material is the smectic C mesophase, which is chiral in structure and is denoted by SmC*. These molecules exhibit short range positional ordering and also long range orientational ordering. This results in characteristic smectic layers being observed, with the molecules possessing a molecular tilt angle of ϕ to these smectic planes. The ordering of smectic C and nematic LCs are illustrated in Figure 2.5, being compared to the isotropic liquid phase. The structure of the SmC* LC is shown in more detail in Figure 2.6. The chirality of the molecule results in the precession of the molecular director through the smectic layers, which is the lowest energy state of the bulk material, i.e. the vector describing the average direction of molecular orientation (director) forms a helix through the material. In order to optimise the optical properties of the material, the helical nature must be suppressed, otherwise the P_s of the bulk material would be zero.

Figure 2.5: Isotropic, Nematic and Smectic C LC phases.

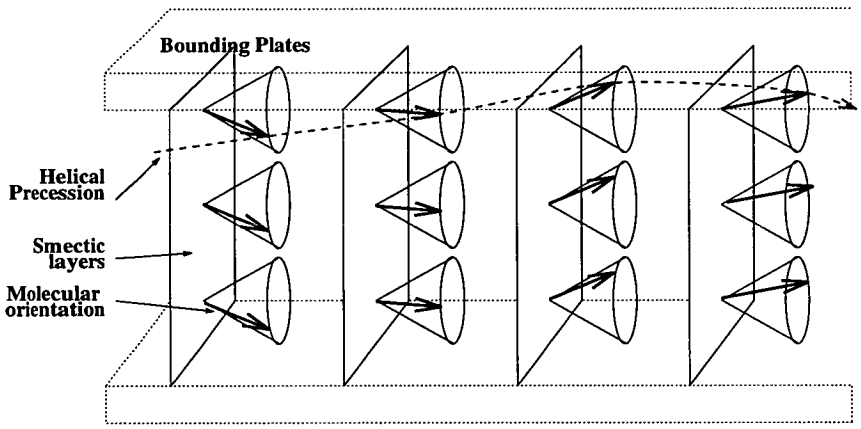

Figure 2.6: Structure of SmC* LC, illustrating the smectic planes and helical director precession.

The most common way of achieving this is the Surface Stabilised FLC (SSFLC) which was first demonstrated by Clark and Lagerwall in 1980 [39]. A transmissive

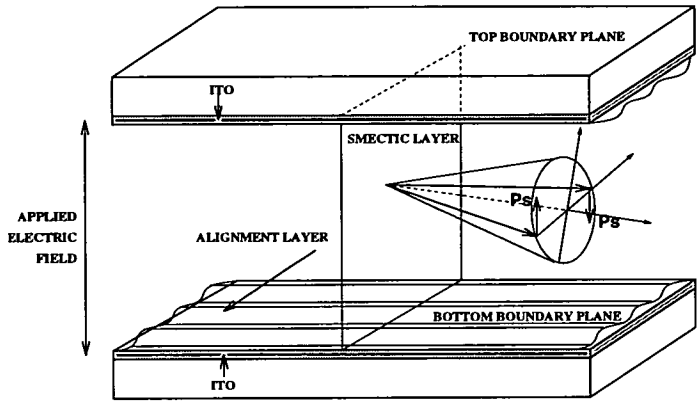

Figure 2.7: Schematic diagram of SSFLC cell, illustrating the two bistable FLC molecular orientation.

SSFLC cell is illustrated in Figure 2.7. It consistes of two parallel glass plates sandwiching a thin layer (1-3μm) of FLC material. The thin cell gap suppresses the helical precession between the smectic planes. This results in two degenerate molecular states in which the directors can exist. These lie at $\pm\phi$ to the layer normal. ϕ is generally close to 22.5°. The LC molecules are macroscopically aligned by thin layers deposited on the glass surfaces. Thse are generally films of obliquely evaporated SiO_x or rubbed polyamide/PVA/nylon, which preferentially align the LC molecules in one direction [40][41]. An electric field can be applied across the cell via transparent Indium-Tin Oxide (ITO) electrodes. This is illustrated in Figure 2.7.

The application of a voltage pulse of the correct polarity across the cell causes the director of the FLC to switch between the allowed states, rotating the optic axis of the FLC by 2ϕ. Provided sufficient switching energy is supplied and the molecular alignment is good enough, bistability is achieved and the FLC will remain in that state until a pulse of the opposite polarity is applied. This rotation of the optic axis can be used to produce either binary amplitude or phase modulation. The physical and optical properties of FLCs are described more thoroughly in [42]-[51].

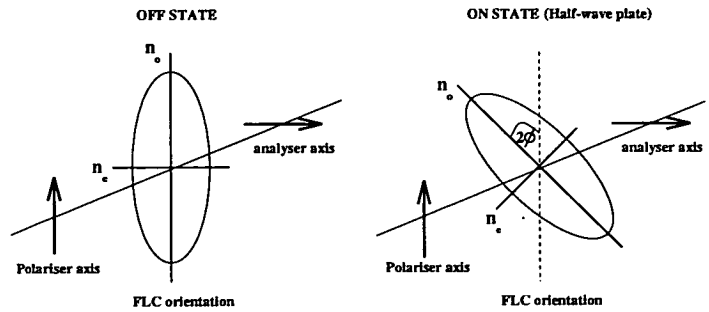

Figure 2.8: Amplitude modulation, ϕ is the FLC tilt angle, n_e and n_o are the extraordinary and ordinary refractive indices.

2.3.1 Amplitude Modulation

As described, the optic axis of the birefringent FLC can be switched between two states separated by 2ϕ, were ϕ is the molecular tilt angle of approximately 22.5^o. Thus the optic axis is rotated by 45°. Amplitude modulation can be achieved as illustrated in Figure 2.8, with the SSFLC cell being placed between crossed polarisers. The input polariser ensures that incident light has its polarisation vector aligned to either the ordinary (n_o) or extraordinary (n_e) axis of the FLC. In this (OFF) state no light will be transmitted through the output analyser. By switching the FLC to the other state, the optic axis is rotated by 45°. Thus the incident light has its polarisation rotated by 90° and so passes through the analyser, the (ON) state. The FLC acts as a switchable half wave plate whose transmission between crossed polarisers is described by Equation 2.1,

$$I = I_o \sin^2(2\varphi) \sin^2\left(\frac{\Delta n d \pi}{\lambda}\right) \tag{2.1}$$

where I is the output intensity, I_o the input intensity, φ the angle of alignment between the FLC and the polariser, d is the thickness of the FLC cell, Δn the birefringence of the FLC, and λ the wavelength of the incident light. It can be seen from this equation, which defines a half wave plate, that for a particular thickness d the transmission is optimised for a particular wavelength. For the He-Ne wavelength of 633nm a transmissive FLC cell using the Merck SCE13 FLC

mixture (Δn=0.14) is optimised when d is 2.26μm, and reflective cells at $d = 1.13$ or 3.39μm. However, due to the availability of spacer balls, the thickness of the cells used in the work presented in this thesis is 3μm. This decreases the optical throughput by approximately 25%.

2.3.2 Phase Modulation

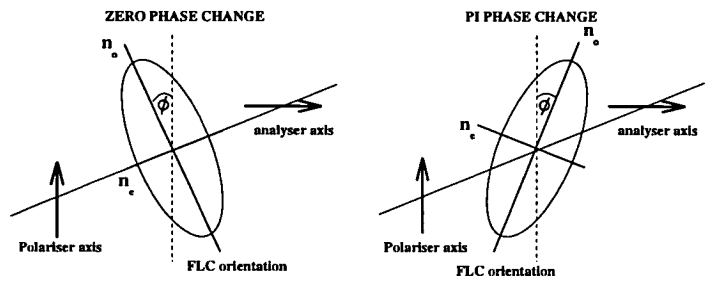

Figure 2.9: Phase modulation using a SSFLC device.

Although phase modulation can be achieved using the same arrangement as illustrated in Figure 2.8, Figure 2.9 illustrates a more useful method of achieving phase modulation.

The polarisation vector of the input light is set to bisect the two switchable optical axes of the FLC. As the light propagates through the FLC, it becomes elliptically polarised, with the sense of polarisation being set by the state of the FLC, e.g. (ON) produces clockwise elliptical and (OFF) produces anticlockwise. When these elliptically polarised beams pass through the analyser they are reduced to linearly polarised beams exhibiting a relative phase difference of π. This is extremely useful as the ability to produce π phase modulation is very powerful, as will be illustrated in the following chapter.

It can be seen, using a Jones matrix analysis [52], that for the SCE13 FLC, with its 22.5^o switching angle, an attenuation of $\frac{\sqrt{2}}{2}$ is observed when used as a phase modulator, due to the elliptical polarisation of the modulated light. It should be noted that if the FLC had a tilt angle of 45°, the optic axis would switch through

90°, producing linearly polarised light in each state with the required π phase change. In this case no analyser would be required and 100% transmission would be achieved.

In practice both the optical throughput and contrast ratio are limited by quality of the FLC alignment, defects occuring within the FLC, and the polariser efficiencies. The causes of these problems are discussed in detail in [53] and are outwith the scope of this thesis.

2.4 FLC Over Silicon SLMs

The marriage of FLCs and silicon CMOS provides a powerful technology for fabricating SLMs. The technology was first developed by Underwood et al. [54][55] at the University of Edinburgh, initially using nematic LCs, and is now being exploited by several research groups around the world [56][57][52]. The switching voltage requirements of the FLC materials and the complex addressing strategies required for large arrays are easily achievable through standard CMOS processes. The basic structure of a FLC over silicon SLM (FLC/Si SLM) is illustrated in Figure 2.10. The silicon chip carries of an array of metal mirrors. Voltages can be supplied to these mirrors via CMOS driving circuitry located at each pixel and on the periphery of the array. A voltage is also supplied to the front electrode which consists of a transparent ITO layer deposited onto an optically flat glass substrate. Thus the FLC lying over individual pixels can be switched "ON" or "OFF" depending upon the electric field between the mirror and the front electrode. The thickness of the FLC cell is chosen so that the FLC acts as a switchable half waveplate on reflection, as described in the previous section.

In order to interrogate these devices optically, some form of crossed polarisers must be used. This is commonly achieved using a Polarising Beam Splitting cube (PBS), which transmits p-polarised light and reflects s-polarised light at the design wavelength. A simple optical system used for modulating a coherent beam is illustrated in Figure 2.11. The half waveplate (HWP) is rotated to optimise the performance of the device.

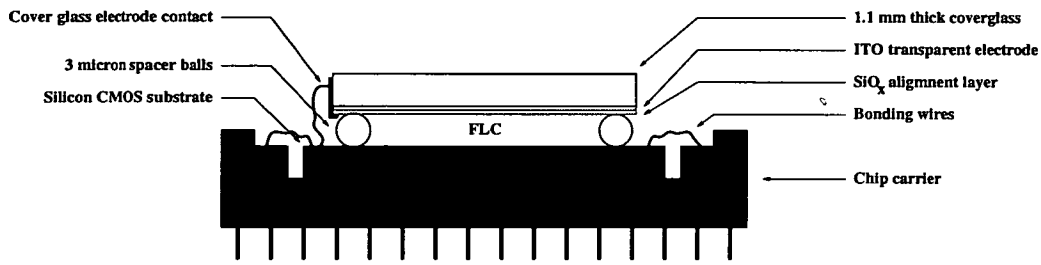

Figure 2.10: The structure of a FLC/Si SLM.

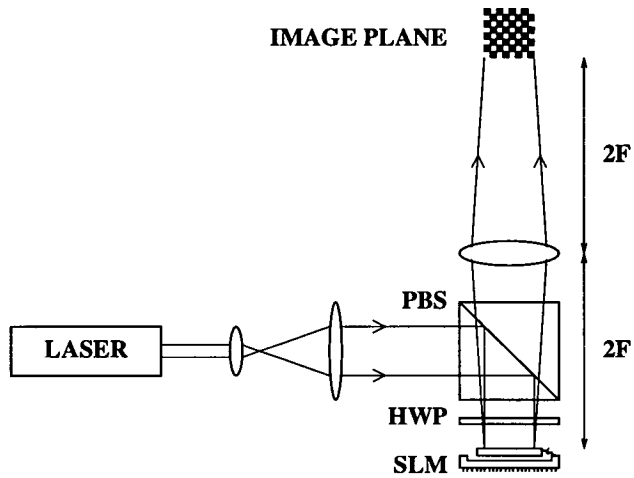

Figure 2.11: Optical system for imprinting spatial amplitude information on a coherent beam.

At present there are two common electrical addressing schemes. The first is based on Dynamic Random Access Memory (DRAM) technology, and utilises a single transistor at each pixel [56][58]. This allows extremely small pixel sizes to be achieved ($15\mu m \times 15\mu m$), along with fast frame rates. However, a drawback of this type of addressing is that the data needs to be constantly updated, which leads to complex electrical interface requirements. The architecture relies on the bistability of the FLC to retain the image between the refresh signals, otherwise pulsed illumination is required [2]. At present DRAM addressing schemes are more common in devices which are used for display applications rather than optical processing.

The second type of addressing utilises static memory (SRAM), in conjunction with an XOR gate. This will be described in more detail in Section 2.6. It allows driving voltages to be applied to the FLC at all times by storing the pixel data within the pixel itself. Thus it is not necessary to continually refresh the data and LC bistability is not essential for achieving a high duty cycle.

Both of these addressing schemes need to take into account the D.C. voltage balancing requirements of the LC. For every voltage pulse across the FLC, a similar voltage pulse of opposite polarity needs to follow. This prevents degradation of the FLC through migration of ionic impurities to the electrode surfaces. The requirement of voltage balancing significantly affects the duty cycle of the devices. In section 2.6 the architecture and operation of a 256×256 pixel SRAM device will be considered. For a more comprehensive discussion of the various devices available, and the LC over single crystal silicon technology in general, the reader is directed to two review papers available on this subject [2][59].

2.5 Planarisation

In order to improve the optical performance of FLC/Si SLMs some form of planarisation is required, as the basic devices have low pixel fill-factors and optically rough mirrors. The technique used at the University of Edinburgh has been developed by O'Hara et.al. [60][61] through the SCIOS collaborative project [62]. Figure 2.12 illustrates the difference between a planarised and unplanarised device. Once the 4 inch diameter wafers return from the silicon foundry which performs the CMOS processing, a 4μm thick layer of SiO_2 is deposited onto the wafer using an Electron-Cyclotron-Resonance Plasma Enhanced Chemical Vapour Deposition (ECR-PECVD) system. The deposited layer conforms to the underlying circuitry. The SiO_2 is then polished to a high degree of optical flatness using chemical-mechanical polishing. After this procedure the SiO_2 is approximately 2μm thick. Contact holes are then etched through to the underlying mirrors and aluminium is sputtered onto the surface. The final step is to etch a pattern of electrodes and mirrors in the top layer of metal to provide new high fill-factor, optically flat pixels.

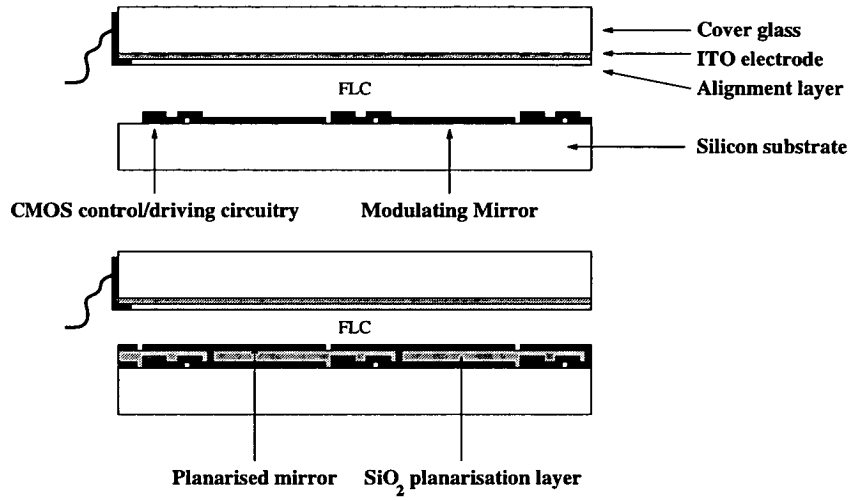

Figure 2.12: Comparison of planarised and unplanarised FLC/Si SLMs.

The advantages of this planarisation can be summarised as follows.

- Increase in mirror fill-factor within a pixel e.g. 23% to 85%.
- Optically flat mirror surfaces, 100Å rms over 250μm.
- Better FLC alignment due to the decrease in surface roughness.
- Less photo-induced charge leakage on DRAM devices.
- Prohibition of spurious FLC switching over interconnect/bus lines carrying voltage signals.
- Smaller pixels can be fabricated as the mirrors lie over the pixel circuitry.

Figure 2.13 shows Scanning Electron Microscope (SEM) pictures of the planarised and unplanarised 256×256 pixel device, which clearly illustrate the improvements in fill-factor and mirror flatness. The optical effects of the inter-pixel gap and the contact hole will be considered in Chapter 5.

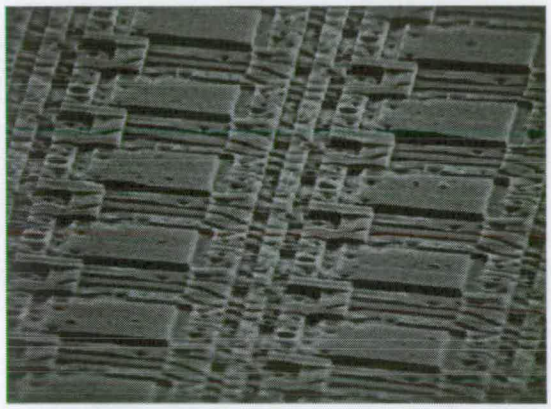

(a)

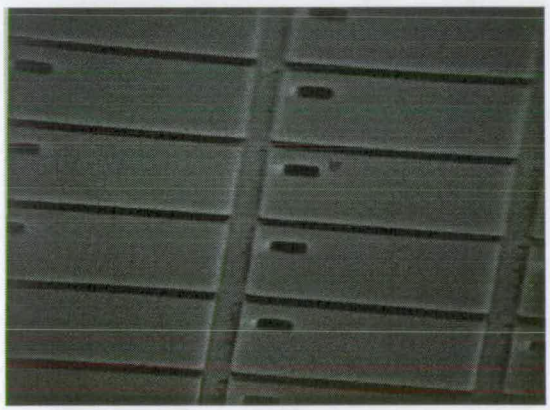

(b)

Figure 2.13: SEM images of a (a) unplanarised 256×256 device, and (b) a similar planarised device.

2.6 The Planarised 256X256 Pixel SRAM SLM

This device, along with its interface and driving software, have been designed, constructed and written by D. C. Burns. The reader is directed to his thesis [63] and publications [64][65][66] for a full description of the device. However as this device has been used in the experimental work described in Chapters 4 & 5, a brief description is presented here.

The specifications of the device are as follows.

- Fabricated using a 1.2μm 5.5V n-well CMOS double-metal process, at Austria Micro Systems (AMS).
- 256$\times$256 pixels on a 40μm pitch, giving an array size of 10.24mm$\times$10.24mm.
- Each pixel contains an SRAM latch and an XOR gate to provide easy D.C. voltage balancing.
- D.C. voltage balanced frame rate of 3-4kHz.
- Basic 19μm$\times$19μm mirror, increased to 37μm$\times$37μm after planarisation.
- Row addressing using 32 parallel 8-bit 25MHz static shift registers.
- Column addressing using a 8-to-256 line decoder.
- pixel clocks skewed off-chip to allieviate potential current spike problems.

A circuit diagram of the SRAM XOR pixel is illustrated in Figure 2.14. Once the data is loaded into the latch it is held there as long as the chip is powered up, thereby simplifying the interface design as an image only needs to be downloaded once onto the chip and will remain optically valid until the next image is downloaded. The XOR gate allows easy D.C. voltage balancing by toggling the front electrode voltage (connected to the clock), as illustrated in Table 2.1. This results in a 50% duty cycle, with the image being present for half the time and all pixels being turned off for the other half.

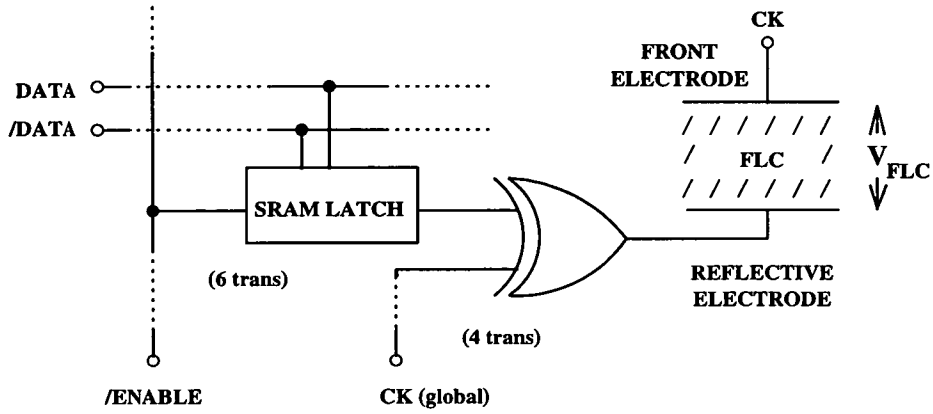

Figure 2.14: Schematic layout of the 256×256 SRAM-XOR pixel, Burns[63].

Inputs to XOR gate LATCH	CK	MIRROR	FRONT ELECTRODE	V_{FLC}	FLC RESPONSE
0	0	0	0	0	UNCHANGED
0	1	1	1	0	UNCHANGED
1	0	1	0	−1	DRIVE OFF
1	1	0	1	+1	DRIVE ON

Table 2.1: Truth table and response of the 256×256 pixel, Burns[63].

The final devices contained Merck SCE13 FLC in a 3μm thick cell. The SLMs are mounted directly on a slow speed interface card which allows clock rates of up to 100Hz, although it takes considerably longer to download different patterns from the PC which drives the interface. A faster interface with on-chip memory has been constructed [63], but was not available for this work. Figure 2.15 shows an image displayed on the 256×256 device.

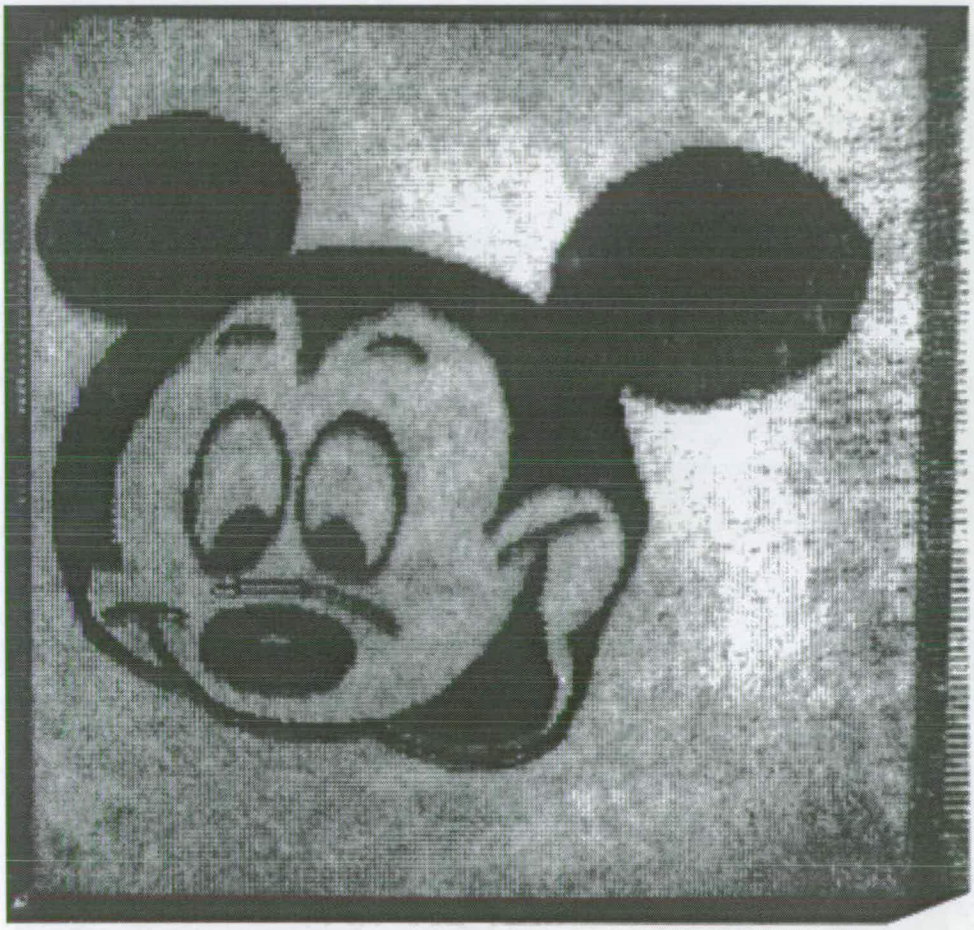

Figure 2.15: Image produced from a planarised 256×256 SLM, produced by Burns [63].

2.7 Summary

In this chapter various SLM technologies have been described. In particular, the performance of DMD and SEED devices have been discussed, along with the FLC/Si SLM used in the work presented in this thesis. The performance of the types of spatial light modulator described in this chapter are summarised in Table 2.2, with approximate values of switching speed, contrast ratio, and drive voltage being presented. It can be seen from this table that FLC/Si SLMs offer considerable potential in applications were a high degree of parallelism is required, however the switching speed of SEED devices is much faster.

MODULATOR	SWITCHING SPEED (Single Pixel)	CONTRAST RATIO	ARRAY SIZE	DRIVE VOLTAGE	COMMENTS
Magneto-optic	30nS	<100:1	128X128	22V	High heat dissipation (needs cooling)
Si/PLZT	<100nS	>500:1	1X16	40V	Smart pixel applications
DMD	10uS	50:1	768X576	<10V	Larger arrays being planned
SEED	10pS	25:1	128X128	<20V	Operates in the IR
FLC/Si	10uS	25:1	256X256	<10V	Larger arrays being constructed

Table 2.2: Summary of the performance of the major SLM technologies.

The optical modulation properties of FLCs have been described, in particular the properties of the surface stabilised FLC cell which allows bistable amplitude and phase modulation to be achieved with switching speeds of the order of 10-100μs. The marriage of FLCs and silicon CMOS backplanes has been discussed, and how these complementay technologies can be used to manufacture reflective, pixellated, EASLMs. The optical performance of these devices can be significantly improved by planarising the silicon substrates, which results in better quality, higher fill-factor mirrors. A 256$\times$256 pixel SRAM FLC/Si SLM has been described. This device has been used in two optical systems which will be discussed in later chapters. The systems use both the amplitude and phase modulation capabilities of this device.

Although fully working devices have been fabricated, there are still several problems which affect the optical performance of these devices, limiting the switching speed, contrast ratio, and uniformity. These will also be discussed in Chapters 4 & 5, when discussing the performance of the optical systems.

Chapter 3

Computer Generated Hologram Fabrication

3.1 Introduction

Computer Generated Holograms (CGHs) are versatile optical components which are now used in many coherent optical systems. They are used in a wide range of applications including focusing [67], beam shaping [68], and fanout [69]-[72]. In recent years advances in computer processing power and fabrication technology have allowed highly complex CGHs to be designed and manufactured. Most of the research into fabrication methods has revolved around optimising the efficiency of the holograms, often at the cost of reducing the yield and manufacturability of the optical elements.

In this chapter a technique which has been used to fabricate large numbers of CGHs showing near optimal performance will be presented. The technique is based on the accurately controlled deposition of silicon nitride on a sapphire substrate which is subsequently patterned and etched, using the sapphire as an etch stop [73]. This process results in optically smooth transmissive phase gratings with a variation in phase depth of less than 1% across a 76mm diameter wafer. Optical results obtained from CGHs will be presented which produce (1) Arrays of equally intense spots, and (2) Spot arrays/images consisting of spots of varying intensities (grey levels). Two of the CGHs presented in this chapter have been designed for use in an optical system which will be described in Chapter 4. The efficiency

of these elements has been found to compare extremely favourably with other fabrication techniques which have much lower yields. The software and algorithms for designing the CGHs used in this work has been developed by Samus [74].

3.2 Theory of Diffractive Optical Elements

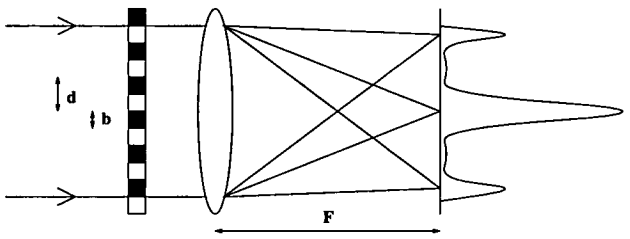

Figure 3.1: Simple Diffraction Grating.

Consider the simple amplitude diffraction grating illustrated in Figure 3.1. When illuminated by planar coherent light of wavelength λ, the Fraunhofer diffraction pattern appears at the focal plane of the lens of focal length F. This is the Fourier transform of the complex amplitude transmittance of the diffraction grating. The spacing between the diffracted peaks is given by;

$$x = \frac{\lambda F}{d} \tag{3.2}$$

i.e. it is dependent upon the pitch d of the grating. However the relative intensities of the diffracted orders are proportional to the ratio b/d i.e. they are dependant on the structure of the grating, the mark-space ratio [75][76].

In its simplest form a CGH consists of a replicated unit cell of period d, however many transition points are contained within this period, rather than the single transition point in a simple grating (see Figure 3.2). By altering the positions of these points the intensities of the light in different diffracted orders may be controlled, maximising the light in some orders and minimising the intensity in others. Thus a one dimensional CGH can be designed to produce an array of diffracted spots of equal intensity, with each spot corresponding to a different

diffracted order, and most of the light being focussed into these desired orders rather than any other diffracted orders.

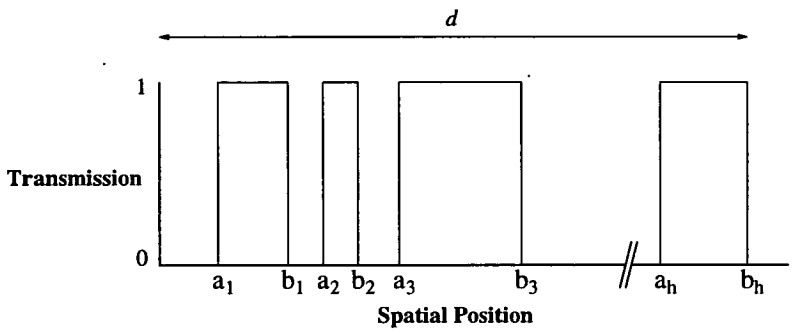

Figure 3.2: CGH Transition points within the unit cell of size d.

The positions of the transition points ($a_1..a_h$ & $b_1..b_h$) are chosen by a computer algorithm such as "Simulated Annealing" [72][77]. The number of transition points is manually chosen, or chosen by the algorithm [74], taking into account that the number of transition points required to reconstruct the hologram effectively increases with the number of spots in the output plane. The algorithm then randomly adjusts the position of the transition points and analytically calculates how close the output of the hologram is to the required spot array, with re-adjustments occuring if no improvement is made. This process continues until the analytical performance of the CGH is good enough to satisfy a specified cost function.

Once a linear CGH has been designed to produce an array of s spots say, the transition points may be used to produce an array of $s \times s$ spots by simply constructing a 2-dimensional array from the transition points in the same way as a simple grating may be used to produce a chequerboard pattern. This type of CGH is known as a *Dammann Grating* [69][70][72][77]. An example of a 16×16 Dammann grating is illustrated in Figure 3.3, with the transition points given in Table 3.1. This unit cell is then replicated into a square array which forms the hologram of N×N cells. The effect of this replication will be considered in Section 3.5.

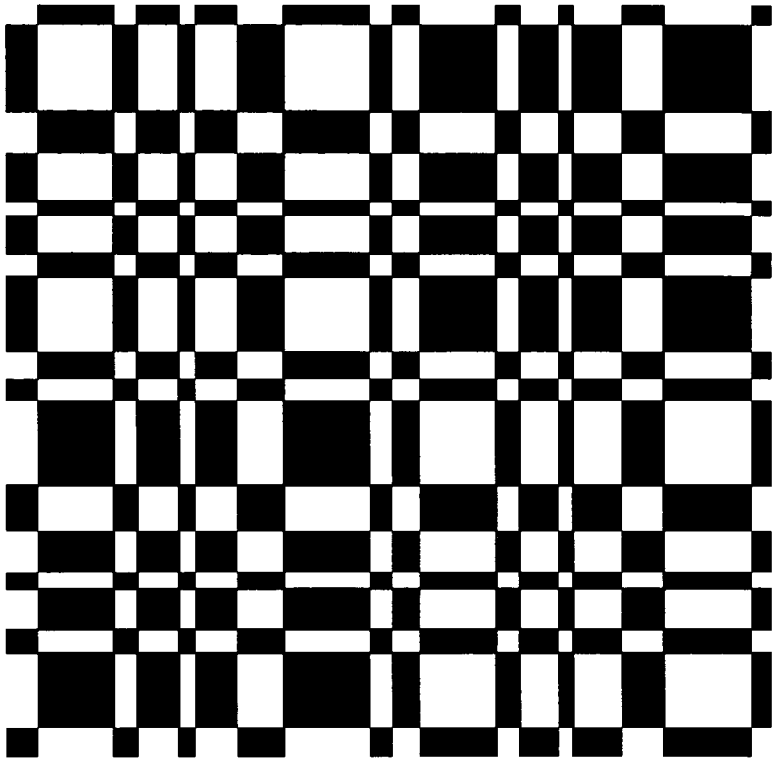

Figure 3.3: Unit cell of 16×16 Dammann Grating.

$0 \rightarrow 1$ Transition ($a \rightarrow b$)	$1 \rightarrow 0$ Transition ($b \rightarrow a$)
0.000000	0.039035
0.138932	0.170173
0.224478	0.245961
0.301181	0.361458
0.474307	0.503317
0.538810	0.638775
0.670051	0.720332
0.740412	0.802904
0.858767	0.974260

Table 3.1: CGH Transition points for a 16×16 Dammann Grating, Samus[74].

3.2.1 Phase Only Elements

The discussion so far has centred around binary transmission gratings. These are actually of little practical use as only 50% of the incident light is transmitted through the grating into the designated diffracted orders, resulting in a low optical efficiency. The Fourier properties of amplitude gratings mean that the diffraction efficiency is also low as a high percentage of the diffracted light is focussed into the central (0th) diffractive order. This unwanted D.C. term, known as the D.C. spot may or may not (in the case of an even numbered array) overlap with a desired spot. In order to reduce the intensity of the D.C. spot, and hence improve the efficiency of the CGH, phase modulating elements are used. By changing the opaque or reflective areas of the grating to areas which are transparent, but which introduce a π phase change of the incident light, the optical efficiency is improved as all of the light is transmitted through the hologram. Furthermore, the DE is improved as the Fourier Transform (FT) of a perfect phase grating does not contain the large D.C. term.

This may be explained in the following way. A binary phase grating is described by a function f(x) which can take values [-1,1]. The Fourier Transform of f(x) is denoted by F(u). A binary amplitude grating takes values [0,1] and so the grating function is specified by $\frac{1}{2}$(f(x)+1). The Fourier Transform of this function is $\frac{1}{2}$F(u)+δ(u), with δ(u) specifying the D.C. spot [78].

The quality of a CGH is measured by its *Diffraction Efficiency* (DE). This is defined as

$$DE = \frac{\text{light diffracted into desired spots}}{\text{light transmitted through hologram}} \tag{3.3}$$

and often quoted as a percentage.

The maximum theoretical DE of a $(0, \pi)$ phase modulating CGH is 83-84% [79]. This is because the desired output spot pattern is defined on a finite square array, but the actual optical output consists of an infinite array of diffracted orders, thus the finite array used to define the output is replicated in the optical output plane, in a wrap-around manner. As a result of this the optical output contains the desired output spot array surrounded by an infinite array of much lower in-

tensity spot arrays, placing a limit on the amount of light falling into the desired spots. Furthermore the binary nature of the hologram means that the diffracted pattern will have at least one axis of symmetry about the central order. Assymmetric patterns may be realised by fabricating phase holograms with a larger, but finite, number of discrete phase levels [71][80][81]. However, although this allows holograms with a higher DE to be designed, the fabrication process is much more complex and expensive, and in the case of the simple array generators used here is not worthwhile [82].

In order to characterise fully the performance of a CGH, two further measurements are required. The *Optical Efficiency* (OE) takes into account the optical transmission of the CGH and is thus defined as

$$OE = DE \times \text{optical transmission of CGH material} \tag{3.4}$$

In the case of CGHs which are used to produce spot arrays, the uniformity of the output spots across the array is also of interest, this is given as

$$\Delta U = \frac{\text{(maximum spot intensity) - (minimum spot intensity)}}{\text{(maximum spot intensity) + (minimum spot intensity)}} \tag{3.5}$$

Both of these measurements are often quoted as percentages. There are two main factors which reduce the efficiency of Binary Phase Holograms (BPHs). If the thickness of the phase modulating layer is incorrect a phase change of greater or less than the required π is introduced. This increases the amount of light diffracted into the central D.C. spot. Also positional errors of the transition points result in a deterioration of ΔU and light again propagating into the central spot. Thus the light in the D.C. spot results from an error in the phase modulation depth and positional errors of the transition points. In the case of even numbered spot arrays the intensity of this spot is easy to measure and provides a means of assessing the quality of the BPH. A thorough study of the effect of fabrication errors on the BPH efficiency is given in [83], and also considered in [72][84][85].

Separable CGHs such as Dammann Gratings can only be used to produce square or rectangular symmetrical spot arrays, which limits their applications. Furthermore their DE is limited as their transition points are only calculated for one dimension. The resulting "chequerboard" cell is not fully optimised for producing a uniform 2-dimensional spot array. For example, the 16×16 Dammann Grating illustrated in Figure 3.3 has a theoretical effieciency of 79.5% in one dimension, leading to an efficiency of only 63% for the two dimensional array.

In order to overcome the limitations of separable CGHs, the design algorithm has been extended to optimise the CGH in two dimensions [71][74]. Thus the target and transition point data take the form of two 2-dimensional arrays which represent the image plane and the hologram plane respectively. The algorithm operates in the following manner.

1. A binary array is constructed which contains the target pattern (1's in the position of required spots, 0's otherwise).
2. A second array (the hologram array) of the same size initially contains a random binary pattern. It is this array which will finally contain the CGH data, with opaque (or phase-shifted) pixels being represented by a 1, and transmissive (or non phase-shifted) pixels being represented by a 0.
3. A random point in the hologram array is flipped (1→0, or 0→1) and the Fast Fourier Transform (FFT) of the array is compared to the target pattern. A decision, based on a cost-function, is made whether to (1) keep the flipped element (if an improvement has been made), or (2) randomly retain the flipped pixel or return it to its original state (if no improvement has occured).
4. 3 is repeated until the FFT of the array is close enough to the target pattern to satisfy the cost-function.

The algorithm also supports the following features;

- As a symmetrical optical output is produced by a binary hologram it is not neccessary for the target array to contain all the spots required in the output plane of the hologram, only those spots required to produce half of the symmetrical output are needed. This is illustrated in Figure 3.4.
- The cost-function may be changed after the CGH pattern has converged in order to optimise either the DE or ΔU.
- Although the CGH is binary, the output diffracted spots may have grey-level values.

Figure 3.4 illustrates the target array for a 4×4 spot array CGH, the annealed CGH, and a simulation of the optical output. This *non-separable* CGH design algorithm allows BPHs of near optimum theoretical efficiency to be designed.

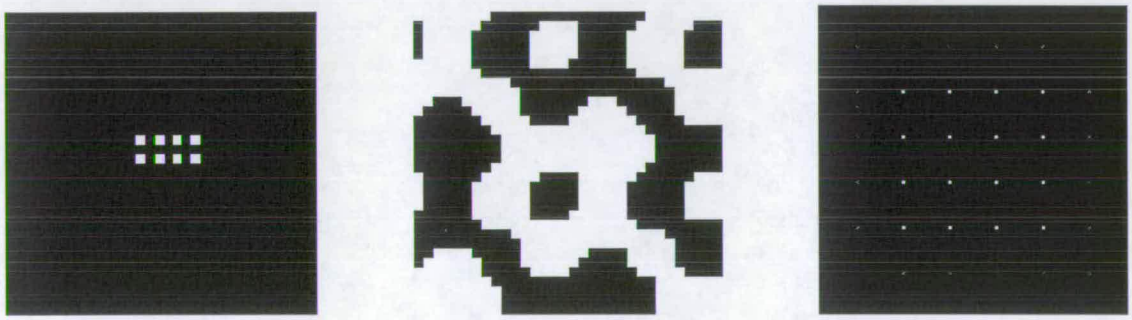

(a) (b) (c)

Figure 3.4: (a) Target array, (b) CGH, and (c) simulated output of the 4×4 CGH.

3.2.2 Fabrication Techniques

Many different techniques have been reported for the fabrication of binary CGHs [86][87]. These include the exposure and bleaching of photographic materials [88], photolithographic or direct-electron-beam patterning of photoresist [80][89][90], the patterning of dichromated gelatin [91], and the controlled etching of bulk substrates [71][72][81]. The viability of these techniques needs to be assessed in terms

of the resulting DE, OE, the cost of fabrication and the yield/reliability of the manufacturing process. The main fabrication technologies will now be considered in more detail.

Photographic Materials

Silver halide photographic emulsion in both film and plate form is a long established medium for the recording of standard interferometric holograms. Commercially available holographic films and plates are characterised by their high-resolution and their thick coating of emulsion. These are also the most suitable films for recording noninterferometric holograms (CGHs) [88].

Once the CGH pattern has been recorded in the emulsion and developed in the same way as an ordinary photographic negative, it may be used as an amplitude CGH. This is frequently done as a cheap prototyping technique to test new holographic designs. In order to produce a BPH the emulsion must be bleached. This may be performed using potassium dichromate based solutions [92] which replace the opaque clusters of silver molecules with transparent salt molecules. As these salt molecules are large with respect to the molecules of the emulsion, once the emulsion dries and shrinks, the CGH pattern is imprinted in the form of a transparent surface relief structure as depicted in Figure 3.5. The problems with this technique are that the optical transmission of the emulsion/film is not very high, the phase shift is unknown and cannot be easily controlled, and there is a slight difference in absorption between developed and undeveloped areas. However this technique is relatively cheap and easy to perform, which makes it suitable for fabricating medium quality prototype BPHs.

Photoresist

Photoresist is a photoactive material widely used in the semiconductor industry for providing an etch resistant layer which may be patterned by exposure to either U.V. light or an electron beam. Thus allowing the pattern to be transferred into

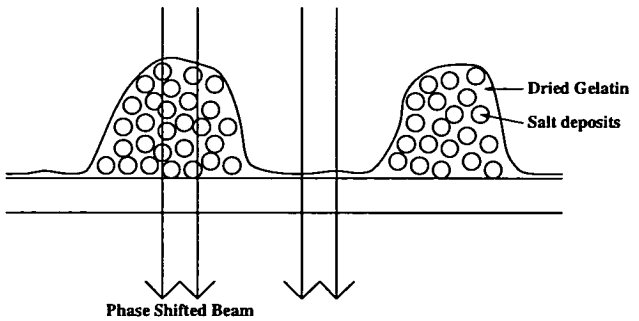

Figure 3.5: Schematic of bleached film BPH.

the underlying layers of metal/insulator/semiconductor as required by the VLSI fabrication process.

Although photoresists, by their nature, have quite a high absorption it is possible to fabricate transmissive BPHs by patterning photoresist on a transparent substrate. The required phase change can be produced by spinning the correct thickness of photoresist onto the substrate, given that the refractive index is ≈ 1.7. Thus from Equation 1.2 it can be seen that for $\lambda = 632.8$nm, a coating of $\approx 0.45\mu$m is required.

Both photoresists and the photolithographic process are well characterised as they are standard in the microfabrication industry, with photolithography allowing 0.7μm resolution to be easily achieved. Using these materials it is possible to fabricate BPHs of good DE, however the following factors need to be considered.

- The thickness of the photoresist can only be controlled to a few percent, and it is difficult to achieve a uniform thickness over large areas. When spun onto a 76mm diameter wafer thickness variations of up to 10% are typically observed.
- The photoresist is partially absorptive to visible light. Thus there is a variation in transmission between the clear and phase-shifted areas which affects the OE and DE.

- After development and hardbaking, the edges of the patterned photoresist are not vertical, but slanted inwards (figure 3.6). The slant angle is determined by the type of photoresist, the coating thickness and the development process. This introduces an error in the DE and ΔU.
- After hardbaking the photoresist is still relatively soft and easily scratched.

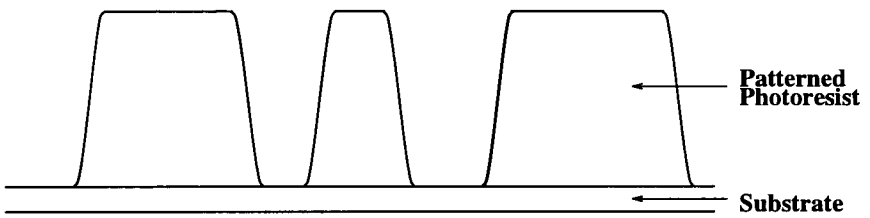

Figure 3.6: Structure of photoresist BPH, showing edge slant.

In order to achieve higher resolution (0.1μm), some photoresists may be patterned by Direct-Electron-Beam (DEB) writing [90]. However, as this is a raster scan type of writing it is not suitable for mass production due to the extremely long writing time required.

Etched Quartz

Quartz, or rather pure silicon dioxide (SiO_2) in amorphous rather than crystalline form, is an extremely suitable material for fabricating BPHs by etching into the bulk of the material. It has high optical transparency and is an extremely hard and rugged material. Due to the chemical composition and high purity (99.99%) of quartz wafers they etch well in a plasma containing He and CHF_3. Figure 3.7 illustrates a typical fabrication sequence for producing a BPH in an SiO_2 substrate. The metal layer is used for two reasons. Firstly, having a reflective rather than transmissive substrate during the photolithographic process allows better focusing of the mask to be achieved, as the focus is controlled by a capacitance meter on the stepper, and also stops the photoresist from being overexposed due to multiple reflections occuring within the substrate. Secondly, it acts as a more resilient etch mask than photoresist during the SiO_2 etch.

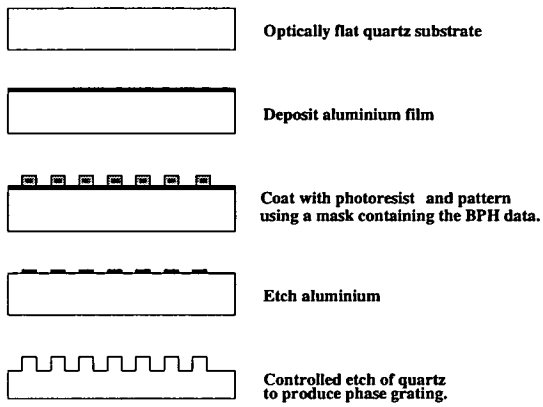

Figure 3.7: Fabrication sequence for etched SiO_2 BPHs.

This fabrication method is the most popular at present for producing high efficiency BPHs [71][72]. However, when this fabrication technique was attempted [93] it was found to suffer from two problems which drastically reduce the yield and increase the production cost. The etch rate of the SiO_2 etch has to be known precisely in order to stop the etch at the required depth. This requires the etcher to be extremely well characterised and maintained. As opening the etch chamber to the atmosphere can result in a subsequent change of etch rate, expensive load-lock configurations are desirable. Also variations in etch rate across a wafer (loading effects) and to a lesser extent across individual die on the wafer (micro-loading effects) may be observed, with the etch rate being higher at the edges of the wafer and die respectively. Such effects occur due to the gas flow over the wafer as illustrated in figure 3.8. The etchant gas mixture at the edge of the wafer/die is rich in free-radicals created by the energy supplied to the gas (RF signal), but as these free-radicals interact with the substrate they become depleted and the gas becomes saturated with etch bi-products. This lowers the etch rate in the centre of the wafer/die. This problem may be overcome to some extent by using more complex *showerhead* type of gas flows, however microloading is often still present. Currently the best results are obtained by only using small substrates which contain a single BPH rather than multiple die. This increases the fabrication cost. Finally, although near optimum BPHs have been fabricated, it often requires several attempts to achieve a sufficiently accurate etch depth, leading to high wastage.

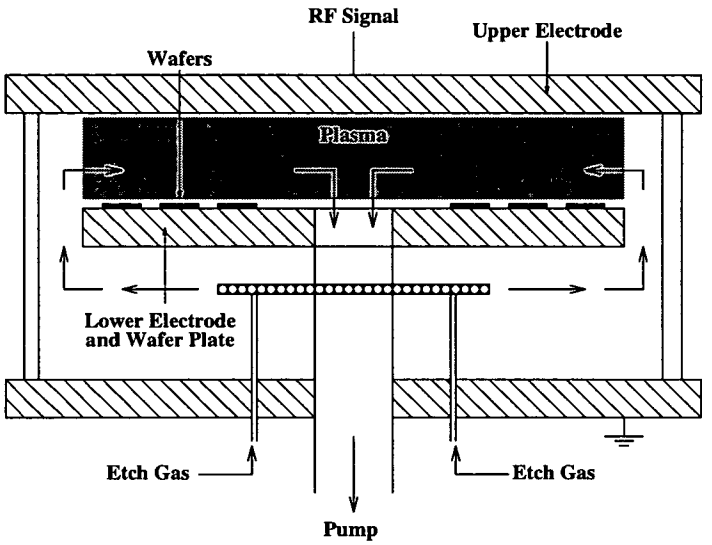

Figure 3.8: Typical plasma etch chamber.

3.3 Silicon Nitride On Sapphire BPHs

This fabrication technique [73] has been developed with two aims in mind. Firstly, a production method was required which would allow high efficiency BPHs to be fabricated without using a large number of complex processing steps or processing uncommon to standard VLSI fabrication. Secondly it was essential to overcome the low yield problems encountered by most other fabrication technologies.

Both of these aims have been achieved by using the Low Pressure Chemical Vapour Deposition (LPCVD) of Si_3N_4 to provide the phase modulating layer, deposited on a sapphire (Al_2O_3) substrate. Once the Si_3N_4 has been patterned using standard photolithographic techniques, the layer can be anisotropically etched back to the sapphire substrate which acts as an ideal etch-stop, thus alleviating the need for strict control of the etch rate and etch uniformity. The materials, process steps and process characteristics will now be considered in more detail before presenting optical results.

Sapphire (crystalline Al_2O_3) has many optical properties which make it a suitable substrate for BPHs.

- It is an extremely hard rigid material, which can be polished to a high degree of optical flatness ($\lambda/60$).
- It has high transmission for e-m radiation with wavelengths in the range 0.2μm to 5μm, (i.e. the complete visible spectrum and all the IR telecommunications wavelengths).
- It exhibits low scatter and chromatic dispersion.
- It has a very low coefficient of thermal expansion ($6.2 \times 10^{-6}/^{o}$C).

It also has physical properties which make it an ideal substrate for processing.

- A high melting point of 2050°C with a softening point of 1800°C.
- Negligible porosity.
- An extremely high resistance to both wet and plasma etches, being effectively unaffected unless the substrate is heated to very high temperatures.

Thus to summarise, sapphire is a transparent material which can be heated to high temperatures, allowing LPCVD films to be deposited, and is impervious to etching, allowing a deposited film to be etched to termination at the sapphire interface.

The only undesirable physical characteristic of sapphire is its birefringence caused by its crystalline structure. It has principal refractive indices of 1.760 and 1.769. This means that when the BPHs fabricated from this material are used in optical systems which use polarised illumination, care must be taken to align either the ordinary or extraordinary optical axis to the axis of polarisation. This is simple to do as the ordinary ray travels parallel to the C-axis of the crystal. The C-axis usually lies at 45° to the flat cut out of the edge of standard wafers, as illustrated

in Figure 3.9. However wafers were purchased with the C-axis perpendicular to the wafer flat, so that the optic axis was parallel to the edge of the die. It was later found (see Chapter 4) that no noticeable detrimental effects were observed, even if the axes were slightly misaligned.

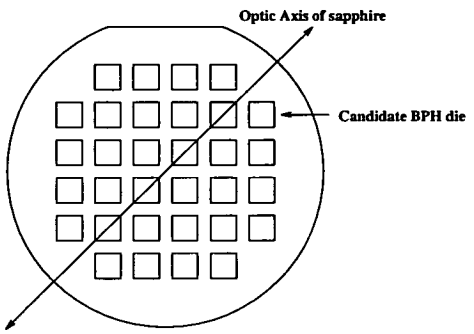

Figure 3.9: Optic axis and die orientation on a standard Sapphire wafer.

Silicon nitride (Si_3N_4) is also an extremely hard material, resilient to surface damage. It has high optical transmission across a broad spectrum, and in the case of the LPCVD films used here, has a refractive index n of 2.00 $\pm$ 0.005. This makes it very suitable for use with a single layer magnesium fluoride antireflective coating which is optimised for materials having

$$\sqrt{n} = 1.38 \tag{3.6}$$

where 1.38 is the refractive index of magnesium flouride [76].

The LPCVD takes place in a quartz furnace as illustrated in Figure 3.10. The tube is evacuated to a pressure of approximately 9 mTorr. The reactant gases flow into the tube from one end at the following flow rates; NH_3 at 90 SCCM (cubic centimetres per minute at standard temperature) and $SiCl_2H_2$ at 20 SCCM. The deposition temperature is nominally 800°C, however as the concentration of the reactant gases decreases as they flow along the tube, a temperature gradient is provided by the 3 zone furnace in order to keep the deposition rate uniform. The deposition reaction is described by Equation 3.7 [94].

$$3SiCl_2H_2 + 4NH_3 \xrightarrow{800^oC} Si_3N_4 + 6HCL + 6H_2 \tag{3.7}$$

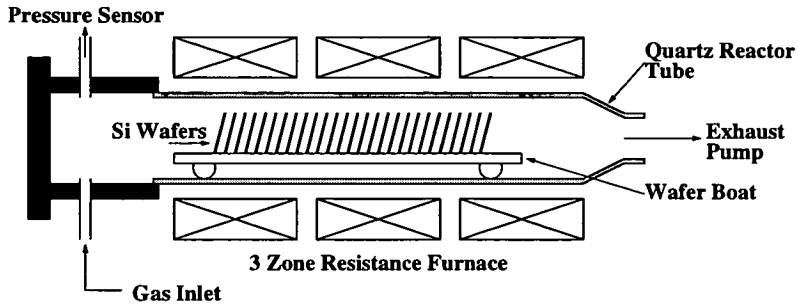

Figure 3.10: Schematic layout of LPCVD deposition system.

3.4 The Fabrication Process

The full BPH fabrication sequence is illustrated in Figure 3.11; however each step will be discussed individually in more detail.

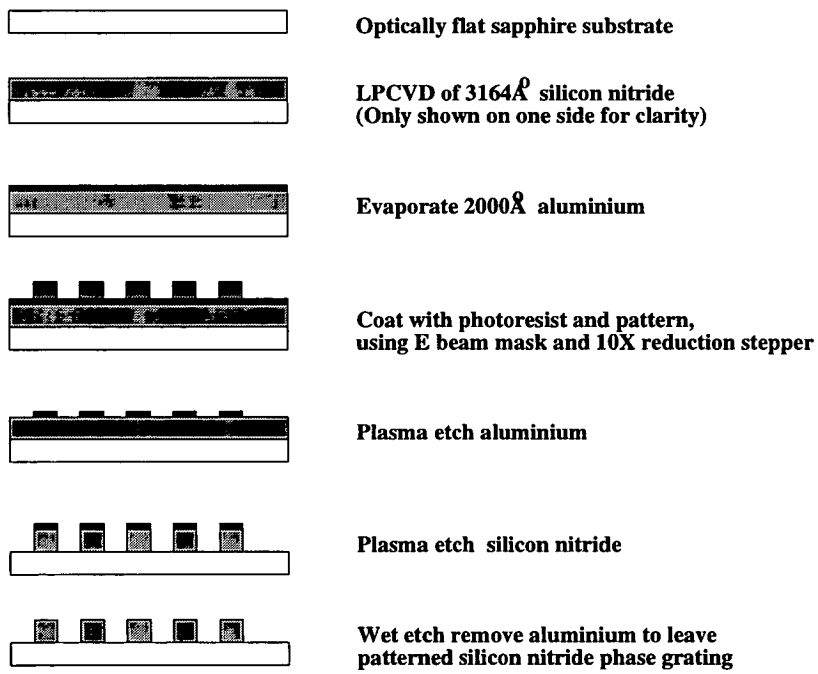

Figure 3.11: BPH Fabrication Sequence.

In order to achieve the required π phase modulation the thickness of the modulating layer t must be such that it introduces an optical path difference of $\lambda/2$. Thus

$$t = \frac{\lambda}{2(n-1)} \tag{3.8}$$

where n is the refractive index of the modulating layer.

For π phase modulation to be realised in transmission a film thickness of $3164A^o$ is required for $\lambda = 633$nm, given a refractive index of 2.00. Due to the low deposition rate ($\approx$ 40 Å/min) a series of three depositions is neccessary, as the maximum deposition time is 30 minutes (due to safety restrictions). However this allows the substrates to be removed from the furnace tube between depositions and the thickness/deposition rate monitored.

As sapphire wafers are transparent and not normally processed in silicon foundaries, it proved difficult to measure the thickness of the silicon nitride film using standard thin film measuring equipment such as ellipsometers and scanning spectrophotometers. Such instruments rely on reflective substrates and are calibrated for silicon wafers. This difficulty was overcome by stacking the sapphire wafers between bare silicon wafers as illustrated in Figure 3.12. This novel idea serves two purposes; firstly, assuming the deposition rate is the same on both silicon and sapphire wafers, the film thickness can be measured on the silicon using a NanoSpec spectrophotometer. Secondly, the silicon wafers act as buffers which aid uniform gas flow over the sapphire wafers, improving uniformity.

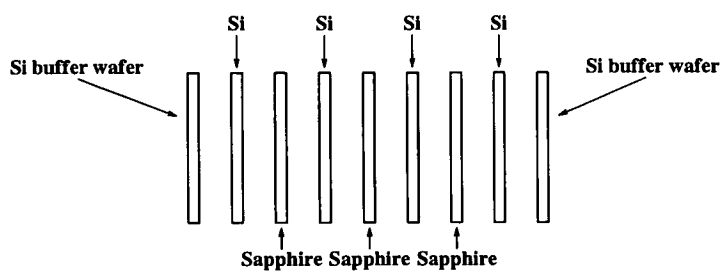

Figure 3.12: Position of wafers in deposition boat.

The film thickness was measured after each of the first two depositions and the deposition rate calculated. The time of the final deposition was then based upon this calculation. Typical deposition times are 30 min./ 30 min. / 24min. 22 sec.

Initially, in order to investigate whether or not the deposition rate was the same for both silicon and sapphire wafers, an area of the film on each wafer was etched off to provide a step. This step height was then measured directly using a Sloan Dektak surface profile contact measurement system. This experiment confirmed that the deposition rates were identical within experimental error. The measurement precision of the Nanospec was found to be ± 3Å, which was found by taking repeated measurements of the same area of film. It was found, once the process had been fully characterised, that films could be deposited with an accuracy of $\pm 1\%$ and a variation of $\pm 0.8\%$ across a 76mm wafer. Finally it should be noted that the deposition occurs on both sides of the substrate. One side may simply be etched off or used as described in Section 3.7.

The metal layer is required to act as a reflective coating to improve the photolithographic processing and to act as a protective layer during the plasma etch of the silicon nitride. Initially, a sputtered aluminium layer of 0.5μm was used. However the aluminium sputtering target contained 1% silicon which left granular deposits once the aluminium was removed. This required a wet silicon etch to displace. In later fabrication runs 2000Å thick layers of evaporated aluminium were used. These were found to perform satisfactorily.

The photolithography was performed using an Optimetrix 10X reduction stepper, with the masks being procured from Compugraphics International Ltd. [95], a company which specialises in fabricating electron-beam written masks. They were fabricated by etching chrome films on a glass substrate, with the pattern being written directly by an electron beam. The data supplied to Compugraphics International Ltd. was prepared using the Cadence EDGE VLSI design tool. This software package allowed data containing the unit cell of the BPH to be imported, scaled to the correct size, and replicated into an array to form a BPH of approximately 8mm^2. The resolution of the final electron-beam mask was 0.1μm.

As previously discussed, the unit cell of the BPH consists of a 2-dimensional array of pixels. By increasing the number of pixels in the cell the quality of the BPH is improved. However, the improvement must be traded against the increased computation time required for designing the BPH and the detail in the cell with respect to the resolving power of the stepper. This was found to be 0.7μm. Holograms have been fabricated with pixel sizes varying from 0.7μm to 5μm.

Photoresist type OCG 6512 spun at 5000 rpm was used to give a thickness of 1μm. The exposure time on the stepper was 1000mS with a focus offset of $+1.5\mu$m. The BPH pattern was replicated over the entire wafer to give thirty two 8mm^2 BPH candidate die on a 10mm pitch.

For BPHs with large pixel sizes a wet aluminium etch could have been used. However, in order to reduce transition point errors a STS Multiplex plasma etcher was used. The etch took place in a plasma of Ar (20 SCCM), Cl (5 SCCM), and $SiCl_4$ (50 SCCM) at an RF power of 200W for approximately 3 minutes. This ensured that the unwanted areas of aluminium were completely removed.

With the sapphire acting as an etch-stop, overetching was not a problem unless the etching time was so long as to destroy the aluminium and etch into undesired areas. It was important to ensure that the Si_3N_4 was completely etched back to the sapphire. The silicon wafers used as dummies during the LPCVD were also etched at the same time, and used to monitor the process. The etch took place in a plasma of CF_4 (60 SCCM) and H_2 (10 SCCM) at an RF power of 750W. The etching process took approximately 16 minutes to complete.

Finally the Si_3N_4 layer was removed from the underside of the substrate, the aluminium was removed by a wet etch, and the wafer diced using a diamond saw to produce the individual BPHs which can be AR coated if required. Figures 3.13 and 3.14 illustrate the chequerboard pattern and edge structure of a 16×16 Dammann grating fabricated using this technique, and imaged using a Scanning Electron Microscope (SEM). Figure 3.15 shows the structure of a 16×16 non-separable BPH imaged using an Atomic Force Microscope (AFM). This illustrates the excellent flatness of both the substrate and the silicon nitride film.

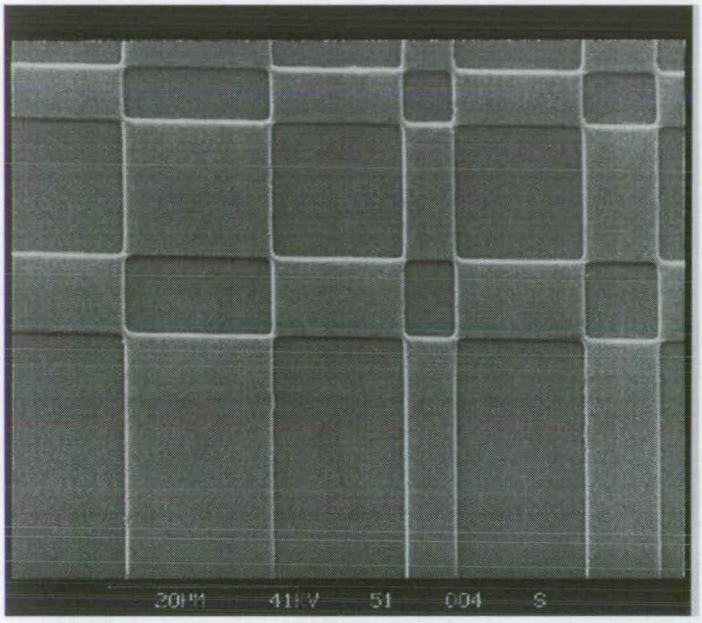

Figure 3.13: SEM Image of gold coated 16×16 Dammann Grating.

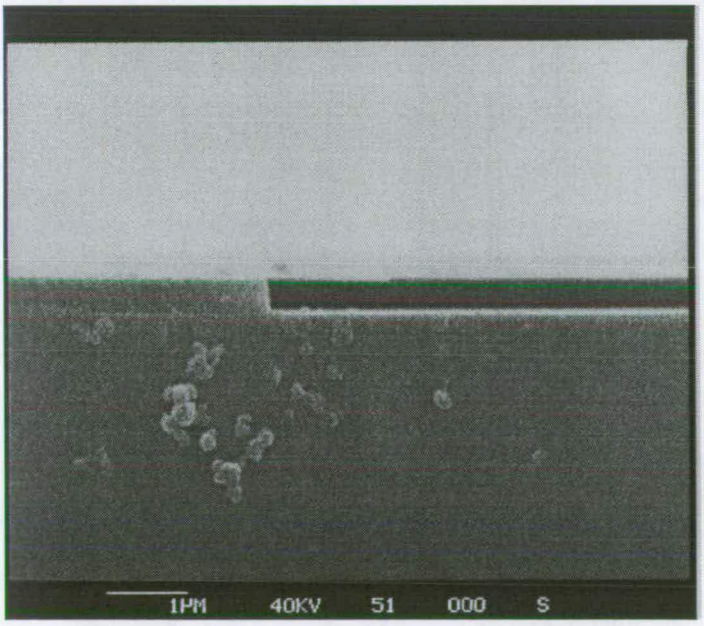

Figure 3.14: SEM Showing edge structure of grating.

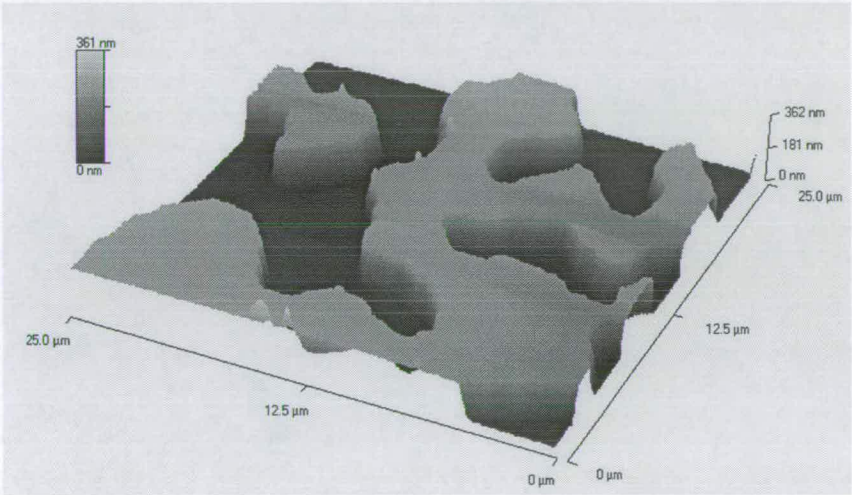

Figure 3.15: AFM Image of a 16×16 non-separable BPH.

3.5 Optical System Considerations

In this section a mathematical description of the formation of spots produced by a BPH in a coherent optical system is presented. This is descibed fully in [96], but summarised here and conclusions drawn about the requirements of the optical system elements.

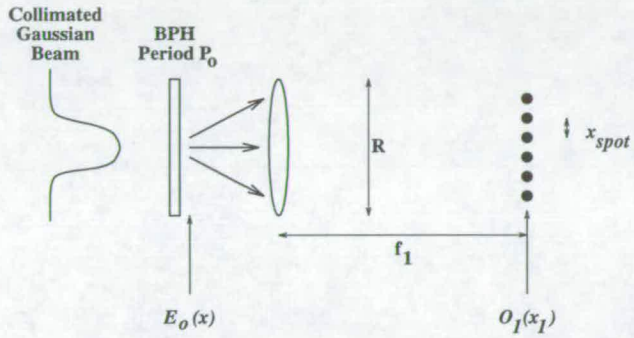

Figure 3.16: Optical system for producing spots from a BPH.

Consider the optical system illustrated in Figure 3.16. A collimated laser beam of wavelength λ with a Gaussian intensity profile is incident on the BPH which has a cell period of P_0.

The following amplitude distribution (in 1D) is produced behind the grating;

$$E_0(x) = \left[h_0(x) \odot \text{comb}\left(\frac{x}{P_0}\right)\right]\left[\text{gaus}\left(\frac{x}{A}\right)\Pi\left(\frac{x}{R}\right)\right] \tag{3.9}$$

The subscripts refer to the various planes in the optical system, as illustrated in Figure 3.16. The convolution operator is denoted by $\odot$.

$h_0(x)$ = binary grating pattern function repeated every grating period P_0.

$\text{comb}\left(\frac{x}{P_0}\right) = \sum_{i=-\infty}^{\infty} \delta(x - iP_0)$

$\text{gaus}\left(\frac{x}{A}\right)$ = A Gaussian envelope, $\exp\left(\frac{-\pi x^2}{A^2}\right)$ of half width $\frac{A}{\sqrt{\pi}}$ at the 1/e points.

$\Pi\left(\frac{x}{R}\right)$ = size of grating, R = grating/system aperture. $\Pi\left(\frac{x}{R}\right) = 1$ when $|x| \leq \frac{R}{2}$, and is equal to zero in all other cases.

Assuming that all the rays entering the lens are within the paraxial region, and that the BPH is the limiting aperture of the system, we obtain a Fourier Transform $O_1\left(\frac{x}{\lambda f_1}\right)$ of the distribution $E_0(x)$ in the back focal plane of the lens of focal length f_1.

$$O_1\left(\frac{x}{\lambda f_1}\right) = (A)(R)(P_0)\left[\text{gaus}\left(\frac{xA}{\lambda f_1}\right) \odot \text{sinc}\left(\frac{xR}{\lambda f_1}\right) \odot \text{comb}\left(\frac{xP_0}{\lambda f_1}\right)\right] H_0\left(\frac{x}{\lambda f_1}\right) \tag{3.10}$$

$H_0\left(\frac{x_1}{\lambda f_1}\right)$ This function now specifies the number and uniformity of spots in the array.

$\text{comb}\left(\frac{xP_0}{\lambda f_1}\right)$ represents an infinite train of 1D Delta functions of period $\left(\frac{\lambda f_1}{P_0}\right)$. This function now specifies the spot period.

$\text{gaus}\left(\frac{xA}{\lambda f_1}\right)$ This function, along with the sinc function specifies the spot size.

$\text{sinc}\left(\frac{xR}{\lambda f_1}\right)$ = FT of $\Pi\left(\frac{x}{R}\right)$

Thus in the back focal plane of the lens we get an array of spots whose number and uniformity is determined by the function H_0, and whose intensity is determined by the square of the magnitude of O_1.

$$\text{spot diameter} = 2\left(\frac{\lambda f_1}{A\sqrt{2\pi}}\right) \tag{3.11}$$

$$x_{spot} = \frac{\lambda f_1}{P_0} \quad \text{for an array with an odd number of spots} \tag{3.12}$$

$$x_{spot} = \frac{2\lambda f_1}{P_0} \quad \text{for an array with an even number of spots} \tag{3.13}$$

Thus the diameter of the spots are not a function of the BPH, but are governed by the wavefront characteristics of the input beam and the diameter of the beam propagating through the BPH. At this point a trade-off occurs. In order to optimise the optical throughput of the system, the spatial filter of the laser may be set up to produce a Gaussian beam of similar diameter to the BPH, maximising the optical throughput, as illustrated in Figure 3.17. However in this case the Gaussian profile dominates the convolution which occurs in the output plane, resulting in a spot diameter larger than the diffraction-limited spot size achievable by the lens.

In order to minimise the spot diameter, which may be necessary for the addressing of some EO devices, the spatial filter must be set up to produce a much wider collimated beam. By using an aperture which only lets the flat top portion of the Gaussian beam propagate, this may be approximated to a plane wave. The FT of the plane wave is a delta function in the output plane; thus the diameter of the spots is only restricted by the aperture of the system. This is illustrated in Figure 3.18. It can be seen that some of the light is sacrificed in this case, reducing the optical throughput. In order to make the diffraction-limited spots as small as possible, the focal length of the lens must be as small as possible, given other considerations such as the system architecture and the BPH cell size.

At this point the need for replicating the unit cell of the BPH into a large array becomes apparent. The cell size is a function of the required spot spacing and focal length of lens, and may be small, tens of micrometres, for a particular application. However if the BPG itself was this diameter, the diffraction-limited spot diameter would be intolerably large, due to the small system aperture. By

replication of the unit cell into an array, the aperture can be increased, reducing the diffraction-limited spot diameter. The spots produced by each cell of the BPH simply overlap due to the shift invariant properties of the Fourier Transform. The light transmitted through each cell has a different phase shift allowing the addition in the back focal plane to take place.

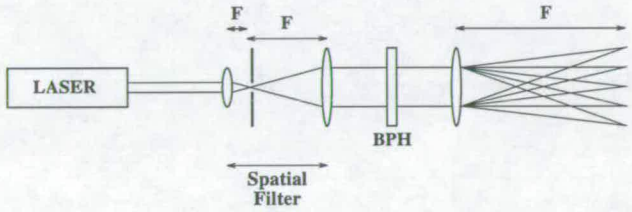

Figure 3.17: Optical system layout for maximising optical throughput.

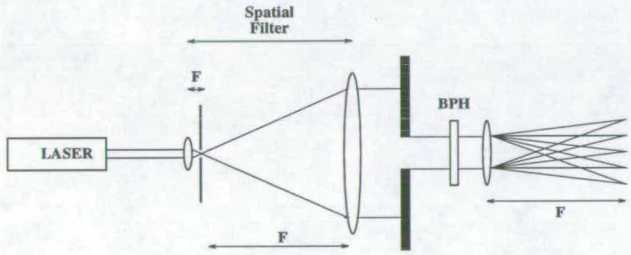

Figure 3.18: Optical system layout for minimising spot diameter.

3.6 Optical Results

Several different BPHs have been fabricated both to assess quality of the fabrication technique and to provide elements for optical systems. In this section optical results of these BPHs will be presented and their optical performance discussed.

In order to assess the quality of BPHs fabricated by depositing Si_3N_4 on sapphire a 16×16 Dammann grating was designed using software developed by Samus [74] and fabricated using this technique [73]. A Dammann Grating was chosen as

its theoretical performance could be accurately calculated using the BPH design program. The DE was calculated to be 79.5% for the 1D array, compared to an ideal maximum of 83% [79]. Thus the DE of the 2D grating is 63.2%, a typical value for a Dammann Grating. ΔU was calculated to be 0.44%. Table 3.2 gives the physical dimensions of the BPH. The optical results are summarised in Table 3.3.

Cell Size	0.25mm
BPH size	8mm^2
Number of die on wafer	32
Si_3N_4 film thickness	$3164A^o \pm 1\%$
Spot Spacing at F=300mm	1.519mm

Table 3.2: Physical characteristics of 16×16 Dammann Grating.

Best Die On Wafer	
Optical Transmission	$91.6\% \pm 0.2\%$
Diffraction Efficiency (DE)	$62.5\% \pm 0.2\%$
Spot Uniformity (ΔU)	1.8%
Optical Efficiency (OE)	$57.25\% \pm 0.4\%$
D.C. Spot Intensity (relative to desired spots)	$\times$ 1.5 $\pm$0.1
Average Across Wafer	
DE Variation	61-62.5%
ΔU Variation	1.8-2.2%
D.C. Spot Intensity (relative to desired spots)	$\times 1.5 \rightarrow \times 2$

Table 3.3: Optical results of 16×16 Dammann Grating.

These results illustrate that the BPHs show near optimum performance in terms of DE, with the intensity of the D.C. spot being consistent with an error in the phase depth of $\approx 1\%$ [83]. There is very little variation in the performance of the 32 BPHs fabricated from the wafer, showing that only a small variation in film thickness occurred. All of the BPHs put at least 56% of the incident laser power into the required spots with an intensity uniformity better than 2%, which compares well

with other fabrication techniques. The measurements were taken using a 300mm focal length Fourier Transforming lens, and scanning a pinhole/photodiode across the array, taking measurements of every spot in order to provide an accurate measurement of ΔU.

Once the fabrication process had been characterised and assessed using the Dammann Grating, several wafers were processed with non-separable BPH designs in order to provide a supply of BPHs capable of being used to address our various pixellated SLMs. Two grey level BPHs were also produced. "*Lena*" was made as a demonstration of the grey level capabilities of BPHs (91 grey levels), and a weighted 16×16 fanout array capable of illuminating our 16×16 pixel SLM was also fabricated. The output spots of this BPH are set at four different grey levels with relative intensities of 1.00, 0.75, 0.50, 0.25. These can be reconstructed to within ±10%. They may be used to provide optical weights in a simple optical neural network, although this has not been pursued at present.

The most important BPHs to be fabricated were two sets of scaled fanout arrays. A pair of 16×16 BPHs with cell sizes varying by a factor of 16 (the BPH pattern is shown if Figure 3.19), and a pair of 4×4 BPHs scaled by a factor of 4 were produced. These reasons for fabricating these will be discussed in both the next section and the next chapter. Table 3.4 gives the physical and optical characteristics of the BPHs which have been fabricated, and the following Figures illustrate the optical results achieved. It can be seen from these pictures that the relative intensity of the D.C. spot increases with the number of spots in the array. The D.C. spot of the 4×4 array having a relative intensity of 0.025, whilst the D.C. spot in the 64×64 being higher at 9.25. This relationship is considered fully in [83], but it can be argued that each transition point contributes towards the D.C. spot due to any positional error; thus as the number of transition points increases, the intensity of light in the D.C. spot increases. The DE measurements were obtained by scanning a photodiode mounted behind a pinhole across the output plane. A point of interest is that the highest DE's observed were obtained from BPHs with very small pixel sizes (0.6μm & 0.7μm). Due to the resolving power of the stepper individual pixels along the edges of the pattern are barely resolved. This has the effect of smoothening the edges of the holographic pattern, removing any noticeable pixellation. It is this effect which is thought to produce the slight increase in

DE.

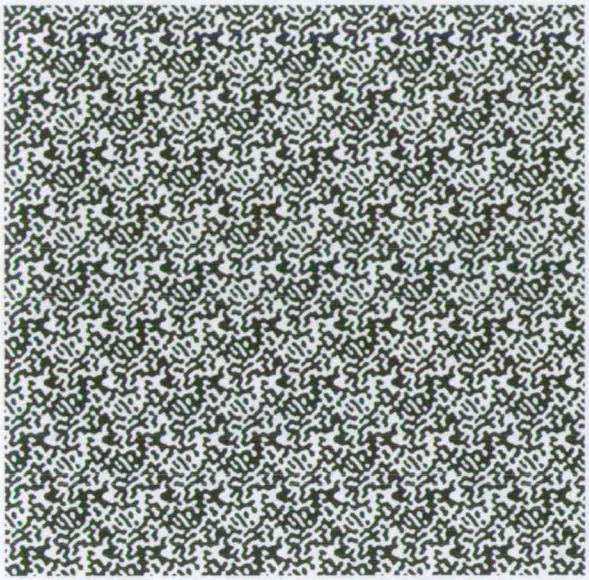

Figure 3.19: 16×16 Fanout hologram, replicated into a 5×5 array.

BPH	Cell Size (um)	Pixel Size (um)	No. of Cells	Spot Spacing (um) for F=50mm	DE (%)	OE (%)	△U (%)
16 X 16	316.4	1.24	14 X 14	200	72±2	66±2	≈1.5
64 X 64	527.3	1.03	8 X 8	120	70±4	64±4	≈7
4 X 4 (1)	316.4	1.24	13 X 13	200	75±1	69±1	1.2
4 X 4 (2)	79.1	0.6	50 X 50	800	77±1	71.5±1	1
16 X 16 (1)	1582	3.1	5 X 5	40	74±2	68±2	≈2
16 X 16 (2)	98.875	0.77	80 X 80	640	77±2	71.5±2	≈2
Neural Net.	316.4	2.5	14 X 14	200	4 Grey Levels		
Lena	506.24	2	9 X 9	125	91 Grey Levels		

Table 3.4: Summary of BPH performance.

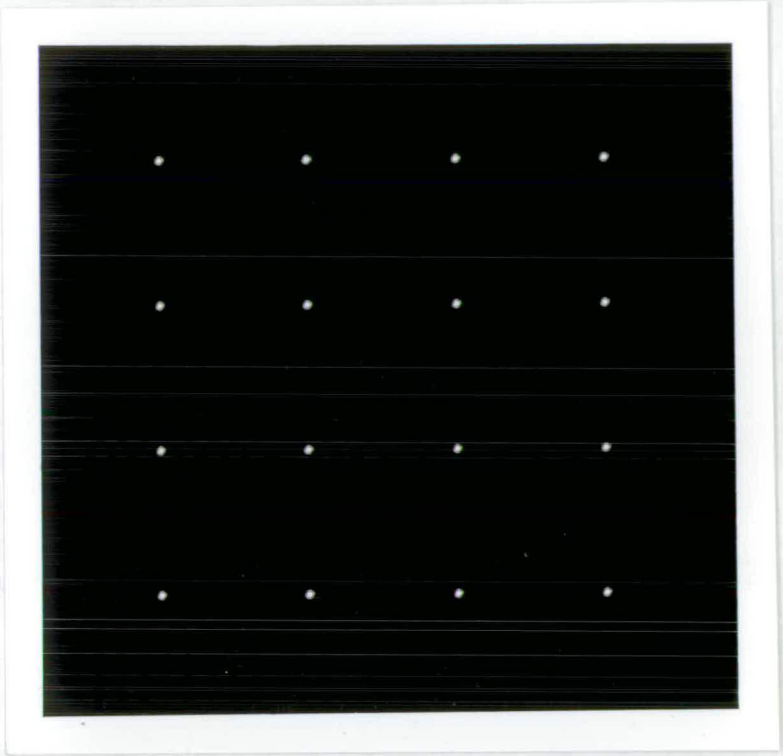

Figure 3.20: Photograph of 4×4 fanout grating.

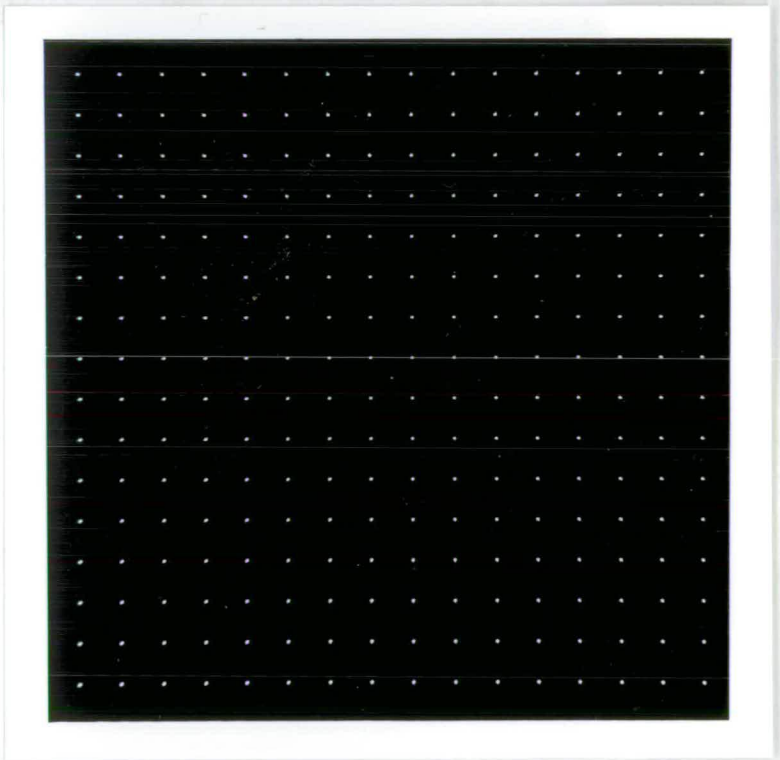

Figure 3.21: Photograph of 16×16 fanout grating.

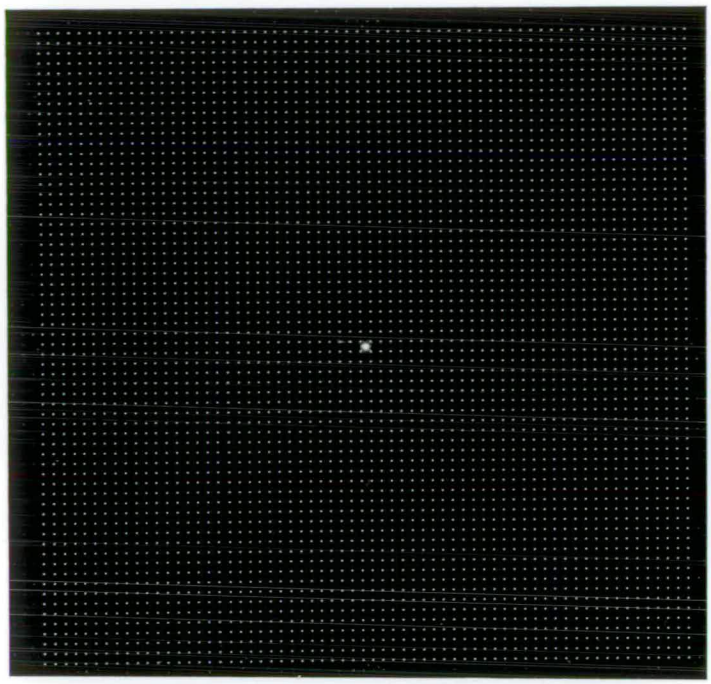

Figure 3.22: Photograph of 64×64 fanout grating.

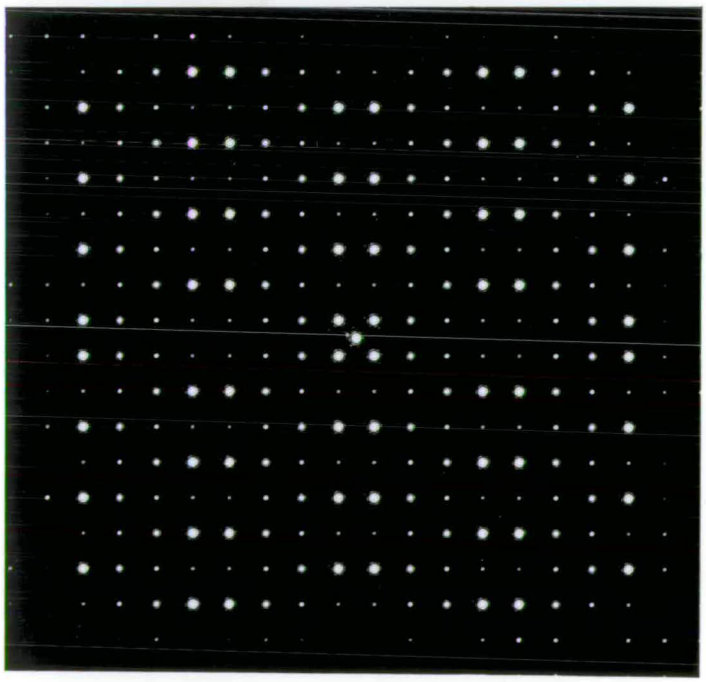

Figure 3.23: Photograph of 16×16 fanout grating, with 4 grey levels.

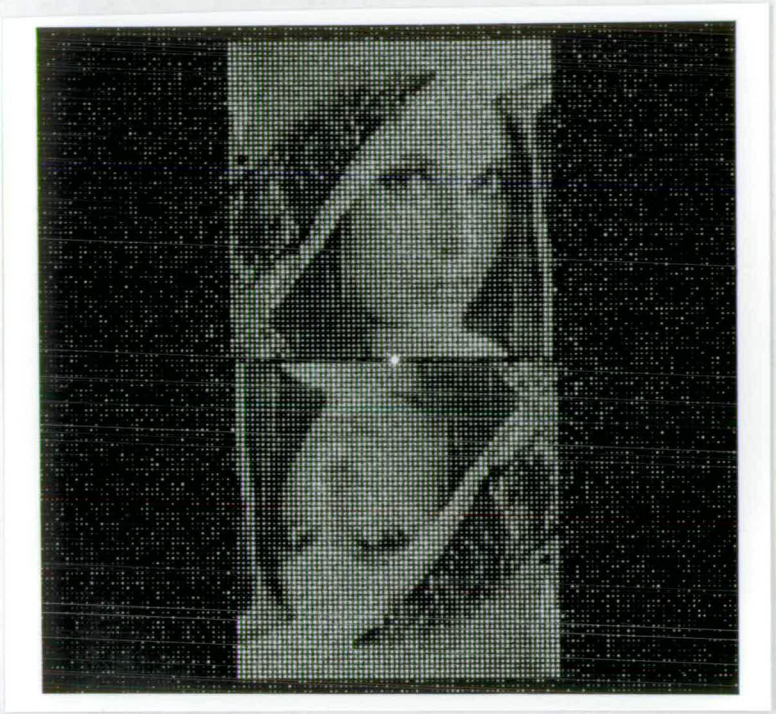

Figure 3.24: Photograph of Lena BPH, based on a 64×64 image with 91 grey levels.

3.7 Cascaded BPHs

As the number of output spots produced by a BPH increases, it becomes computationally difficult to obtain a solution for the CGH pattern due to the large array sizes required. In this section it will be discussed how large arrays of spots (256×256) can be produced by cascading BPHs. Experimental results will be presented and problems discussed.

The first method of producing large arrays is the multiple imaging technique which is discussed in [96]. Consider the optical system illustrated in Figure 3.25, using the same notation as in Section 3.16, the first BPH_1 $G_0(x)$ produces an array of spots $O_1(x)$ in the back focal plane of lens L_1. Each of these spots is re-collimated by lens L_2 to produce an overlapping array of collimated beams incident on the second BPH_2 $G_2(x)$. Each beam travelling though BPH_2 undergoes a FT by lens L_3 and produces a spot array dependant upon $h_2(x)$, the BPH_2 pattern function. However, each spot array undergoes a spatial shift in position due to the spatial variation of the effective point sources in the output plane of BPH_1. Thus the spots

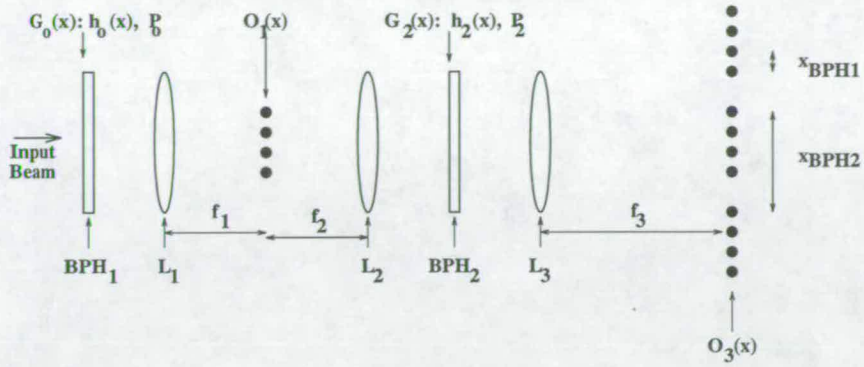

Figure 3.25: Optical system for multiple imaging of BPHs.

in the final output plane $O_3(x)$ are a convolution of the outputs of both BPHs.

This can be described as;

$$O_3\left(\frac{x}{\lambda f_3}\right) = \mathrm{FT}\left\{G_2(x)\mathrm{FT}\left\{O_1\left(\frac{x}{\lambda f_1}\right)\Pi\left(\frac{x}{\lambda f_1}\right)\right\}\right\} \tag{3.14}$$

Thus

$$O_3\left(\frac{x}{\lambda f_3}\right) = g_2\left(\frac{x}{\lambda f_3}\right) \odot \left[\lambda^2 f_1 f_2 O_1\left(\frac{x f_2}{\lambda f_3 f_1}\right)\Pi\left(\frac{x f_2}{\lambda f_3 f_1}\right)\right] \tag{3.15}$$

i.e. the output consists of the array of spots produced by BPH_1, scaled by f_2/f_3 and replicated about an array produced by BPH_2.

Now consider the more simple case were the lenses are all of the same focal length. The spots produced by BPH_1 are on a pitch given by

$$x_{BPH1} = \frac{\lambda f}{P_O} \tag{3.16}$$

replicated on an array of pitch

$$x_{BPH2} = \frac{\lambda f}{P_2} \tag{3.17}$$

It can easily be seen from this that if both BPHs produce an output array of $n \times n$ spots, with the cell sizes of the BPHs scaled by a factor of n, then the output at O_3 will be an array of $n^2 \times n^2$ spots.

There are two points to note: (1) This architecture allows the first spot array to be modulated or spatially filtered at the first image plane O_1. (2) The cell sizes of the BPHs can be controlled to a high degree of accuracy, but the system is dependent on the focal lengths of the three lenses being matched exactly. In practice lenses may have low tolerances in their focal length specification ($\pm 2\%$). Any difference between the focal lengths of the lenses will result in a scaling error in the output array.

This problem may be overcome by a slightly different approach as illustrated in Figure 3.26. In this case only a single lens is used to perform the FT of both BPHs and it can easily be shown that the output is again a convolution of the Fourier Transforms of the BPHs as in the previous case. However as only one lens is used, there is no scaling error between the individual BPH spot arrays, so a cascaded array of equal spot spacing is always produced, if the BPH cell sizes are correctly scaled.

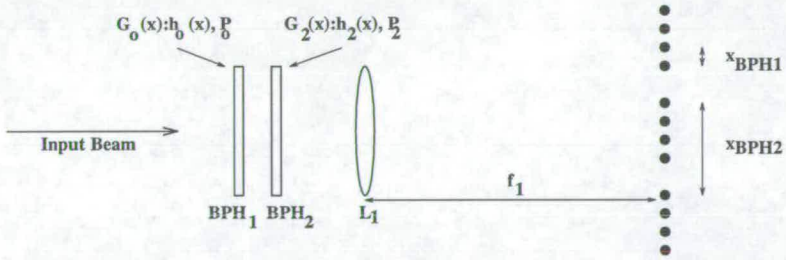

Figure 3.26: Cascaded BPH optical system.

As described in the previous section, two 16×16 fanout BPHs have been fabricated with cell sizes scaled by a factor of 16 (98.875μm and 1.582mm). They were placed into the optical system illustrated in Figure 3.26 and the output (a 256×256 array) produced as illustrated in Figure 3.27.

The DE of this cascaded BPH is simply the DEs of the individual BPHs multiplied together, so in this case the DE is $\approx 57\%$. It can be seen from Figure 3.27 that the central block of 16×16 spots is more intense. This is due to the spots overlapping with an array of 16×16 D.C. spots generated by the second BPH. There are also D.C. spots in the centre of each block of 16×16 spots. These are due to the D.C. spot from the first BPH being replicated by the second BPH. Although this is an obvious problem with this technique it will be shown in Chapter 4 that when these cascaded elements are used to provide structured illumination of pixellated SLMs, the D.C. spots are not reflected from the device and so do not propagate through the optical system. However, if odd numbered spot array BPHs were used the output would look much tidier, as the D.C. spot would be part of the array, but would then obviously propagate through the system. Unfortunately this technique does suffer from another problem. If perfect rotational (θ) alignment is reached between the BPH patterns, the uniformity of the spots degrades drastically. This is due to the spots in one 16×16 block overlapping with higher order spots from an adjacent block, with interference occurring between the two. This does not occur if there is even a slight misalignment as illustrated by the high quality of the spots present in Figure 3.27.

An attempt was made to fabricate both BPH patterns on a single substrate, utilising the fact that the LPCVD of Si_3N_4 deposits a film simultaneously on both sides of the substrate. Once one side of the substrate had been patterned and etched, the other side then had the second BPH pattern written into it. This was possible as the x and y alignment tolerances between the BPHs is very low due to the shift invariance of the Fourier Transform. Only the rotational alignment had to be considered. It was found that by carefully placing the wafer in the holder for the photolithography a rotational error of less than 150μm across the 76mm wafer could be achieved. Optically, the double-sided BPHs worked well enough to prove the principle of the idea, with the rotational error being sufficient to prevent any interference effects without producing any noticeable misalignment in the output array. Unfortunately there were problems during the Si_3N_4 etch, resulting in under-etching occuring. This increased the intensity of the D.C. spots to approximately ten times the intensity of the other spots in the array. However this work has illustrated that large spot arrays can be generated by this technique, although it is perhaps more suitable for arrays with an odd number of spots.

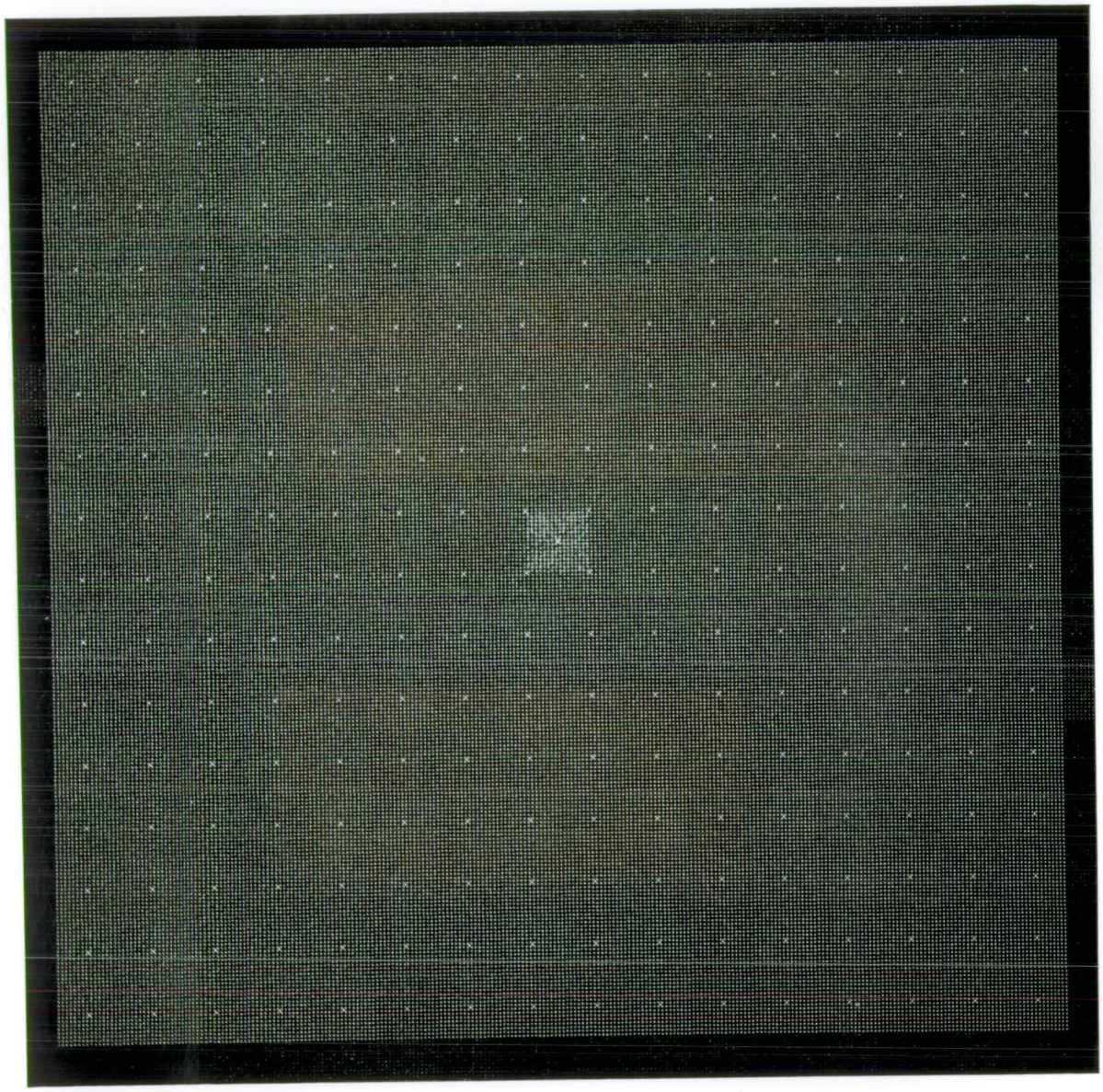

Figure 3.27: Photograph of 256×256 spot array produced by cascading two 16×16 BPHs.

3.8 Summary

In this chapter a technique for fabricating binary phase holograms has been presented. The technique uses the controlled deposition of silicon nitride to produce a uniform, optically flat coating on top of a sapphire substrate. Once patterned with the required holographic pattern, the silicon nitride can be etched back to the sapphire substrate which acts as a perfect etch stop. The thickness of the silicon nitride can be controlled to within 1% of the required thickness to give the π phase modulation. Several binary phase holograms have been fabricated including a 64×64 fanout array and an image containing 91 grey levels. The optical characteristics of the fanout elements have been measured and their performance assessed. The efficiencies achieved by these elements are comparable to BPHs fabricated by etching into quartz substrates. However the yield of this process is much higher with up to 32 BPHs being fabricated simultaneously and only a small variation in efficiency ($\approx$ 2%) being observed. Thus this technique is much more suitable to commercial mass production. Finally a technique has been discussed for producing large spot arrays, with a 256×256 spot array being produced by cascading two 16×16 holograms. Initial experimental work has been performed to produce these large array generators on a single substrate.

An Applied Optics paper [73] describing this work is given in Appendix A.

Chapter 4

A 256 Channel Crossbar

4.1 Introduction

Free-space optical switching systems have applications in a wide range of optical systems such as telecommunications [97], optical computing [98] and optical information processing [99]. Widespread research into the development of these systems has led to a variety of system architectures being demonstrated, using many different modulating or light emitting devices.

In this chapter results of an investigation of a 256 channel crossbar test system will be presented. A 16×16 pixel section of a 256×256 pixel FLC/Si SLM acted as an input plane to the system. This array was optically fanned out by a factor of 16 to illuminate another 256×256 FLC/Si SLM, which acted as a modulation plane. The output from this plane was then interrogated using a CCD camera and pinhole/photodiode arrangement. Although this does not represent the complete switching system, it was used to address specific questions regarding the architecture and performance of the optical components.

4.2 Free-Space Optical Switching Systems and Architectures

Optical switching systems allow optical signals from an input array, which may consist of emitters, modulators, or fibres, to be routed to an output array. It is important that such systems have broadcast (one input to all outputs) and multicast (one input to many outputs) capabilities. In addition the system should be non-blocking; the optical path of input A being routed to output B must not prohibit routing from input C to output D. Other factors which must be considered are the switching speed, attenuation, crosstalk, and Bit Error Rate (BER).

At present there are two approaches to optical switching systems.

(a): One approach is to use devices which can modulate/emit light at the data rate of the optical signals being routed through the system. Many of these type of systems have been developed by groups working in telecommunications applications and the development of optically routed backplanes in large computer systems. McCormick et al. [23][24][25][100] from AT&T Bell laboratories in Illinois have demonstrated a 32→16 channel switching network based on FET-SEED smart pixel arrays. Due to the nature of the Banyan architecture used in the system the routing is performed in five stages, consisting of 2×1 multiplexer nodes, with the routing path at each stage being selected by optical information provided as a header in the data stream. Figure 4.1 illustrates the architecture of this generalised shuffle network with Banyan interconnects, along with the data format including the control data fields. This system has been demonstrated to operate at 50Mbits/s with some stages operating at 155Mbits/s and a BER of 10^{-10}. This test system has been developed for use in telecommunications switching applications. Future systems are plannned which will operate at over 2Gbits/s, to be used with the new Asynchronous Transfer Mode (ATM) protocol. Another research group from McGill University in Canada [101][102][103] has presented results of a FET-SEED based demonstrator system for optically interconnecting Printed Circuit Boards (PCBs) and Multi-Chip Modules (MCMs) within large computer systems. Researchers at the NEC Research Institute [98][104] have recently demonstrated a 64 channel optical interconnection network based on

Vertical Cavity Surface Emitting Lasers (VCSELSs) and photodiodes. Once again this system has again been developed for interconnecting processors/processing boards in large computer systems.

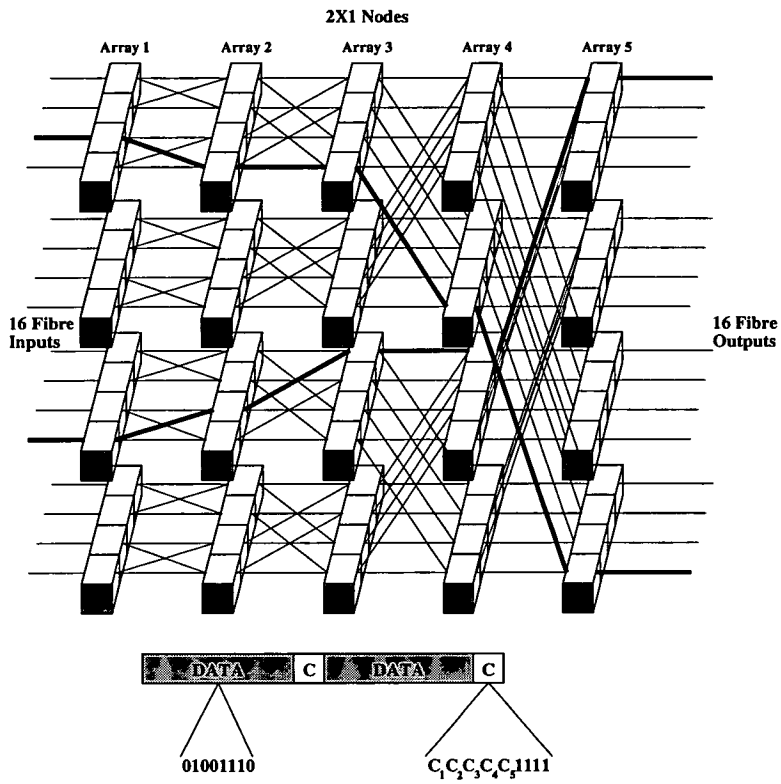

Figure 4.1: Schematic of the AT&T 5-stage generalised shuffle network, and example of the optical data stream showing the control routing data fields, as illustrated in [23].

All of these systems which use VCSELs or SEEDs switching at the optical data rate are multiple stage networks.

(b): The second approach to optical interconnection systems is to use a single stage architecture. This can be achieved using dynamic holographic routing (which will be discussed in Chapter 5) or the free-space crossbar architecture, based on the Stanford optical vector-matrix multiplier architecture [105][106][107] illustrated in Figure 4.2. By fanning out each element of the input vector (X) to a row in the modulation plane which contains an SLM supporting grey-level modulation,

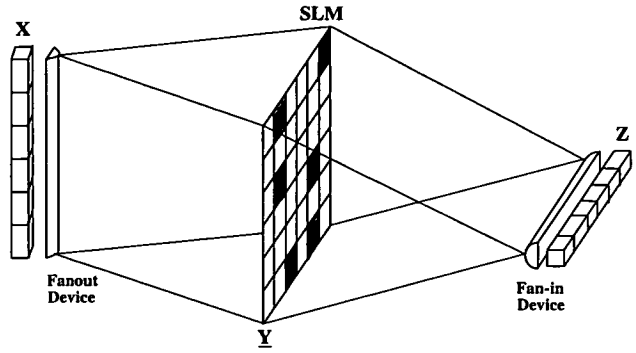

Figure 4.2: Schematic architecture of the vector-matrix multiplier.

matrix($\underline{Y}$), and then fanning in each column to the output vector (Z). It can be shown that Z=$\underline{Y}$.X. In practice this particular architecture is difficult to implement as cylindrical lenses are required which suffer from severe aberrations such as astigmatism. This has led to the more general crossbar architecture being developed [108] in which the input and output vectors are folded into arrays. This architecture is illustrated in Figure 4.3.

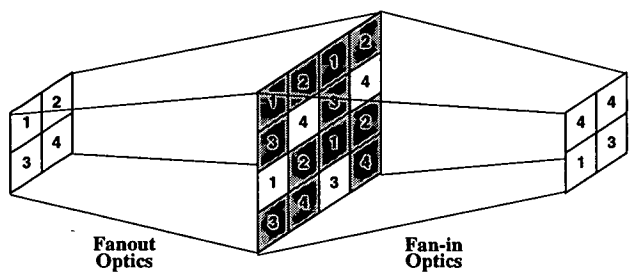

Figure 4.3: Schematic representation of a free-space crossbar.

When this system is used as a digital optical signal interconnection network, the SLM is not required to support grey-level modulation, and acts only as a plane in which *windows* can be closed, blocking the incident data stream, or opened, allowing the data to pass through. Thus binary modulation is sufficient.

The following points should be noted regarding this architecture.

- The modulator array need not switch at the data rate of the input channels as the modulator is effectively invisible to the data stream. It is only required to switch between data packets.
- The architecture allows broadcast and multicast to be easily achieved.
- There is an intrinsic $1 \rightarrow n$ fanout loss. Where n is the number of channels. Thus for each channel there is a loss of $3\log_2 n$ dB.
- Although Figure 4.3 illustrates a transmissive modulator, a reflective device can also be used.

4.3 The OCPM Project

The Optically-Connected-Parallel-Machine (OCPM) project [57] is a collaboration between British Aerospace, Heriot-Watt University, BNR Europe, the University of Bath and Thorn EMI CRL Smectic Technology. The University of Edinburgh is involved as a technical partner to the project. The aim of this project has been to design, fabricate, and characterise a 64 channel crossbar based on the architecture illustrated in Figure 4.3. The layout of the system is illustrated in Figure 4.4. The inputs consist of 790nm laser diodes pigtailed to polarisation maintaining fibres which are arranged into an 8×8 array. The light from these fibres is fanned out to a 64×64 array using a non-separable Binary Phase Hologram (BPH). The spot array is focussed directly onto a 64×64 pixel FLC/Si SLM which acts as the modulating element. The modulated array is then fanned into an array of 8×8 multimode output fibres by two holographic lenslet arrays.

The project has attempted to totally optimise the performance of the system by the custom design of all the components within the system. At the time of writing this thesis, the optical system has been assembled and is awaiting the insertion of the custom FLC/Si SLM. The salient points of interest regarding this system are summarised as follows.

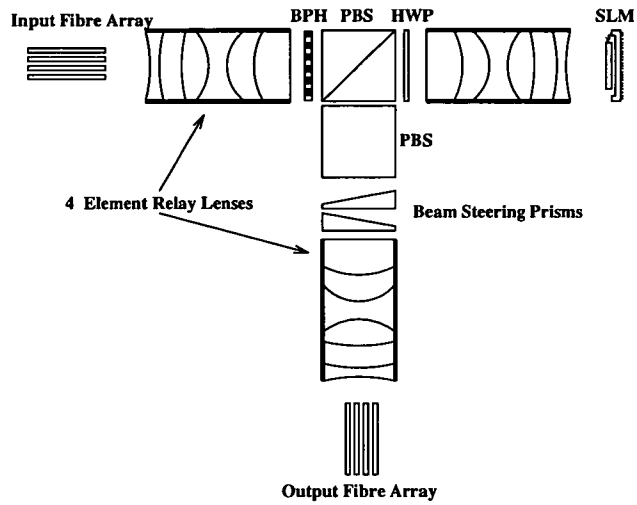

Figure 4.4: Layout of the OCPM 64×64 channel crossbar, as illustrated in [57].

- There is a 1 to 1 imaging relationship between the input fibre array and the SLM. Thus all the relay lenses have the same focal length, reducing distortion and field curvature across the image field.
- The relay lenses are 4-element lenses designed and optimised using the CODE V optical design software package. They have a focal length of ≈40mm with a 16° field of view.
- Two polarising beam-splitting cubes (PBSs) are used in order to increase the extinction ratio between the ON and OFF channels reflected from the SLM.
- The PBSs have been custom designed to optimise the extinction ratio at the correct wavelength over a wide range of input beam angles.
- Beam-steering prisms are used to provide fine manipulation of the optic axis of the output beams.
- The FLC/Si SLM is a custom design which has been developed at the University of Edinburgh. The device has ≈ 70μm×70μm pixels on a 120μm pitch.

- The input fibre array was fabricated by forming holes in a Kevlar substrate by excimer laser ablation [109], which held the fibres securely in place.
- The output fibre array is on a 960μm pitch, using 300μm core multimode fibres, mounted in a holder fabricated from anisotropically etched silicon.

This work has highlighted some of the inherent problems in building this type of system. These include polarisation alignment of the input fibres, wavelength variation between channels which results in positional errors of the spots, and the variation of extinction ratio of a PBS with input angle. Finally, significant work has been performed on optimising the opto-mechanical mountings and system baseplate, so as to allow accurate alignment whilst being stable and vibration tolerant.

4.4 The 256 Channel Crossbar Testbed

The OCPM project aims to build a fully working 64 channel crossbar system, using custom made optimised components to achieve the best possible system performance. However, it has not experimentally addressed the question of scalability. In order to do this a 256 channel test system has been constructed. This system has been designed to attempt to answer the following questions.

- How scalable are crossbars implemented using FLC/Si SLMs, i.e. what is the maximum number of channels that can realistically be achieved in a fully working system, and which elements in the system limit the scalability?
- What are the critical tolerances affecting the system performance, and how do these tolerances scale with the number of channels in the system?

In the rest of this chapter the architecture and optical results of the test system will be discussed and some conclusions drawn. A more general discussion of the results will take place in Chapter 6.

4.4.1 System Design And Architecture

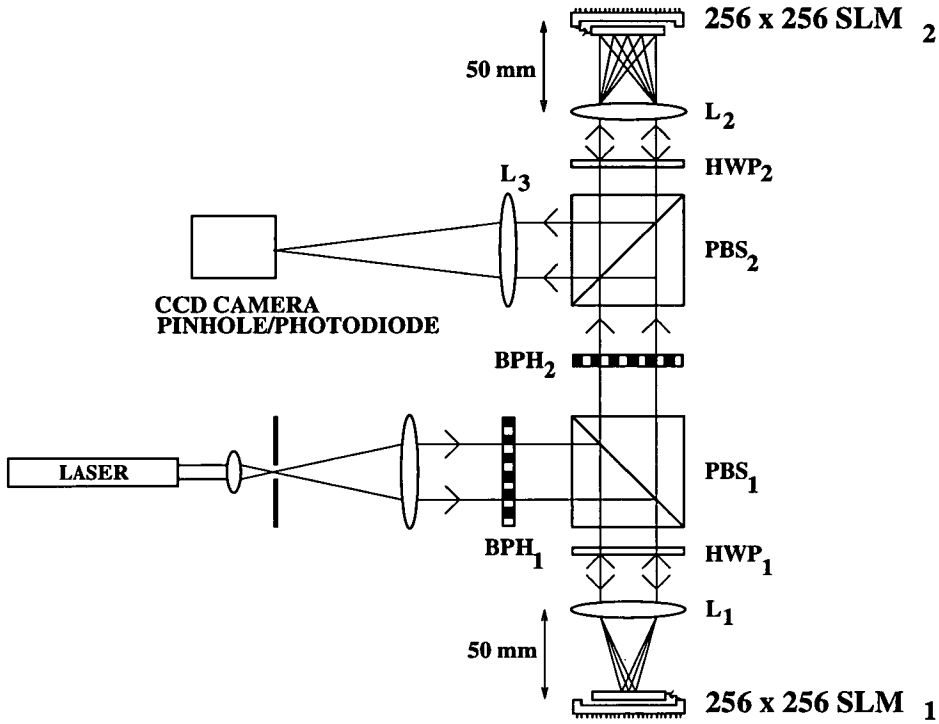

Figure 4.5: Architecture of the 256-channel crossbar test system.

The layout of the optical system is illustrated in Figure 4.5. The 256 input channels are formed by illuminating a 16×16 block of a 256×256 FLC/Si SLM (SLM_1) with an array of spots generated by a 16×16 BPH (BPH_1). The characteristics and performance of the BPHs used in this system are given in table 3.4. The SLM was used to provide an input array rather than a fibre array for two reasons. Firstly, the fabrication of such a large fibre array would be extremely difficult [109] and trying to transmit light through them all would be impractical, due to the large number of lasers required. Secondly, there are many applications for crossbars which have an SLM as the input, such as neural networks, optical data encryption, and optical computing. These applications are more relevant to the research undertaken at Edinburgh University, and hence it made the system of more interest to the rest of the research group. The input array was then fanned out a further 16×16 times by BPH_2 to produce a 256×256 array incident on SLM_2 which acted as the modulating device for the crossbar. If a full system had been

implemented the light reflected from this SLM would be fanned back into a 16×16 array using an array of diffractive/refractive microlenses. However as this type of element has been well characterised [110] and its performance was not expected to be a limiting factor of the scalability of these systems [111] it was not included in this system. Furthermore the exclusion of fan-in optics allows the performance of the modulator to be assessed as the output of individual pixels can be interrogated. This was achieved by imaging the modulating plane onto a CCD camera/pinhole mounted in front of a photodiode. Before considering the individual components in more detail, there are two important points regarding the system architecture which must be noted.

- The architecture is similar to the cascaded hologram system discussed in Section 3.7, with the SLMs being inserted in planes O_1 and O_3 (Figure 3.25).
- As the pitch of both SLMs is the same, lenses L_1 and L_2 have the same focal length, i.e. infinite conjugate imaging is used. This reduces barrel distortion and field curvature of the images.

4.4.2 Optical Components

The laser used in the system was a 15mW He-Ne (632.8nm), however the optical output was measured to be nearer 17mW. The laser emitted a plane polarised beam and was rotated to optimise the intensity reflected by the Polarising Beam Splitter PBS_1 onto SLM_1. The spatial filter/beam expander consisted of a 40X microscope objective, 10μm diameter pinhole, and an achromatic lens to re-collimate the beam. The size of the pinhole was chosen to allow only the light in the Airy Disc to pass through. Thus the pinhole acted as an almost perfect point source. It was calculated that 91% of the light was transmitted through the pinhole. Two different collimating lenses were tried, the first had a focal length of 50mm which produced a collimated beam of 8.5mm in diameter, slightly larger than the open aperture of BPH_1. However, this was found to produce focussed spots of insufficient quality, as described in Section 3.16. A lens with a focal length of 200mm was then used which

produced a beam with a diameter of 3.4cm. An aperture was placed before BPH_1 which allowed a phase-flat, 8mm diameter, collimated beam of almost uniform intensity to pass through BPH_1.

The polarising beamsplitting cubes (PBS) transmit horizontally polarised light (s-polarisation) and reflects vertically polarised light (p-polarisation) at 90°. Both of the PBSs were optimised for use with He-Ne lasers and the following measurements taken.

$$\text{p-state transmission} = 99.20\% \pm 0.05\%$$
$$\text{s-state reflection} = 0.34\% \pm 0.05\%$$
$$\text{Extinction ratio } (292\pm3):1$$

In order for a high extinction ratio to be achieved the light must pass through the PBS at normal incidence as the extinction ratio of the PBS varies with the incident angle of the light. As the beam only began to diverge very slightly after passing through the BPH, with the angle of divergence being governed by the cell size, the extinction ratio was not affected. The lens L_1 performed two functions, it acted as a Fourier Transforming element for BPH_1, as described in Section 3.16, and also re-collimated the reflected spots so they propagated back through PBS_1 as parallel beams. The half waveplate (HWP_1) was used to align the axis of polarisation of the beams to the optic axis of the FLC such that it is optimised for amplitude modulation as described in Section 2.3.1. Once the reflected light returned through the half waveplate it was either in the p-state (mirror ON) or s-state (mirror OFF). It is at this point that the importance of having a high extinction ratio between the transmission of the s and p states becomes apparent as any s-state light transmitted through the PBS is noise and so reduces the contrast ratio of the SLM.

Once the re-collimated light beams from the ON pixels have passed through PBS_1, they pass through BPH_2, which has been designed to replicate each spot by a further factor of 16×16, to produce a 256×256 array. The system is symmetric about this point with the spots being produced and re-collimated by L_2 with the modulation being performed by SLM_2. Light in channels which are turned on by both SLM_1 and SLM_2 is finally focussed by lens L_3 and interrogated by a CCD

camera or pinhole/photodiode. The lens L_3 is chosen to magnify the final output array for examination.

It was found that the BPHs performed very well. Initially there was concern that the birefringence of the sapphire would cause problems by altering the polarisation state of the light. However it was found that once the optic axis of the sapphire had been approximately aligned to the polarisation of the incident light, no noticeable effects were observed. It was also found that the D.C. spots in the BPH output planes did not propagate through the system to any large extent, as they were not directly reflected by the mirrors, being incident on the inter-pixel gap, rather than a reflective mirror.

The lenses L_1 and L_2 are the most important passive elements in the system, as their performance is crucial to the scalability of the system, so at this point both lenses will be discussed in some detail. They must fulfill the following criteria.

- They must be able to produce spots over a large image field without field-curvature and barrel distortion occurring. They must exhibit the"F.sinθ" Fourier Transforming properties of a simple lens, i.e. the diffracted spot spacing must be governed by Equation 3.13. A lens will generally only exhibit this characteristic over a small angular field, unless its design has been carefully constrained. This is described in [112].
- They must be able to produce diffraction-limited spots (this is also a function of the input beam diameter and wavefront characteristics). Although the diameter of the diffraction-limited spots is considerably less than that of the pixel mirrors, if the spots were not diffraction limited, aberrations would become more dominant and the quality of the beams propagating through the system would be adversely affected.

The linear dimension of the image field of L_1 is only 906μm (field-of-view=1.04°), but for L_2 it is 14.48mm (16.5°) which is very large. The two lenses are used back to back in an infinite conjugate system, which should theoretically eliminate field-curvature, however there was concern that field curvature would still reduce the performance of the system.

Initially 50mm f/2.8 achromats were used. The first lens was found to perform satisfactorily, but L_2 was found to suffer from severe field-curvature. Field curvature is the variation of focal length with distance from the optic axis, as illustrated in Figure 4.6. This is a serious problem in systems which use BPHs as it causes the focus of the spots to vary across the array. In the case of this cascaded BPH system, the scaling between the sub-arrays forming the large array is also affected. This is illustrated in Figure 4.7.

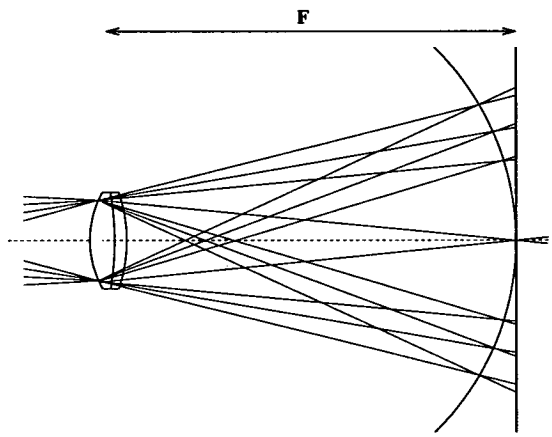

Figure 4.6: Illustration of field curvature, which is the variation of focal length with distance from the optic axis.

This problem was solved by replacing the achromats with Spindler & Hoyer Microprojection lenses [113], which had the following specifications.

- 50mm focal length, f/4.5.
- 5-element compound lenses.
- Optimised for low magnification.
- Optimised for flat/distortion free imaging over wide image fields. Field-of-view = 44°.

These lenses were found to have the correct "F.sinθ" Fourier Transforming characteristics over the entire image field. They produced diffraction-limited spots

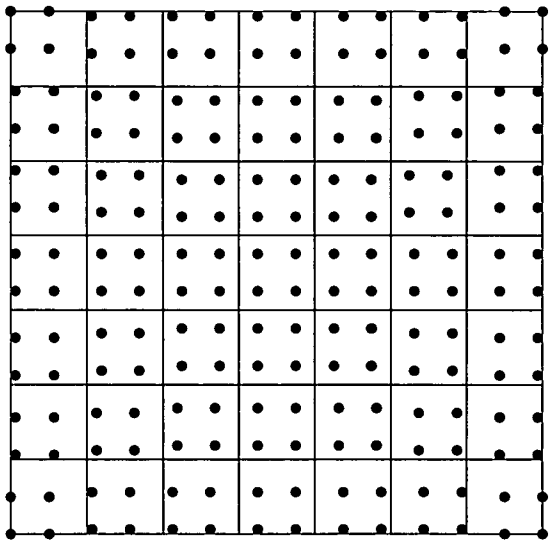

Figure 4.7: Example of how field curvature affects the scaling of cascaded holograms.

(7μm) without any field curvature or barrel distortion being apparent over the whole image field (10.24mm$\times$10.24mm).

The system was designed in such a way that the passive optics could be assembled, aligned and locked into position without the need for any translational adjustment. Only the SLMs required translational movement. SLM_1 required translational adjustment in the x & y planes to align the mirrors onto the spots, and adjustment in the z plane (along the optic axis) to ensure that the mirrors were in the back focal plane of L_1. Rotational alignment of the spots was achieved by rotating BPH_1. The second SLM required the same degrees of freedom along with rotational adjustment. All the translational movement was provided by translation stages with 50mm travel and $\pm 1\mu$m precision adjustment. In order to ensure that both SLMs were in the back focal plane of their respective lenses, a shear plate collimator was used. This instrument gives an accurate picture of the divergence/convergence of a collimated beam.

4.4.3 Optical Results

The performance of the optical system was assessed at three points in the system; the light reflected from SLM_1 (imaged on to a CCD camera), the light incident on SLM_2, and the final imaged output spots. The optical results are presented in this order. All the pictures showing the output from the system have been recorded using a CCD camera, rather than a photographic camera due to the small size of the arrays of spots, which made focusing a photographic camera extremely difficult. As a result of this the pictures have a poorer quality than the actual output due to the low resolution of the CCD camera.

By studying the 16×16 spot array modulated by SLM_1 information is provided about the performance of the SLM. Figure 4.8 shows the array reflected from the SLM with all the pixels turned on. It can be seen that the DC spot of the BPH does not propagate through the system as it is not incident on a mirror, but is scattered within the inter-pixel gap. Figure 4.9 shows two opposite quarters of the array being turned off by the SLM.

The optical performance of the SLM was measured and it was found that the optical throughput was 13%, the contrast ratio was 25:1, and the spot uniformity ± 10%. These results were taken using a pinhole/photodiode arrangement and also by using a software package to interrogate the images obtained from the CCD camera. Both sets of results were found to be in good agreement. Similar measurements were taken from SLM_2. These results are summarised in Table 4.1. The optical throughput measurement is low as structured illumination was not used in this case.

	SLM_1	SLM_2
Optical Throughput	13% ± 1%	15% ± 1%
Spot Uniformity	±10%	±9%
Contrast Ratio (using structured illumination)	(25±2):1	(27±2):1

Table 4.1: Summary of Optical performance of the SLMs.

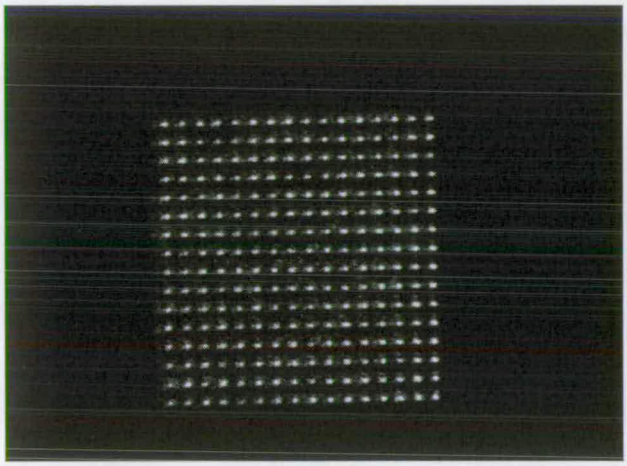

Figure 4.8: 16×16 BPH output reflected off SLM_1 with all the spots turned on.

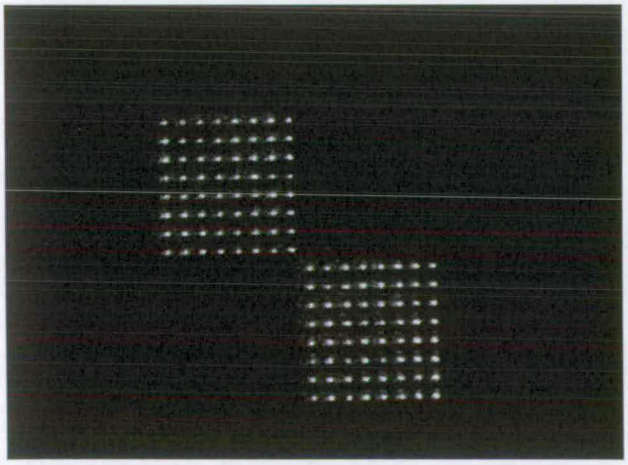

Figure 4.9: As Figure 4.8, but with opposite quarters turned off by the SLM.

The fanned out input array incident on SLM_2 was then examined. The quality of this modulated 256×256 array was critical to the performance of the system and an indication of the performance of lens L_2 in particular. Figures 4.10 and 4.11 illustrate sections of the fanned out 256×256 array. These pictures were taken using a longer focal length lens (200mm) than L_2 in order to resolve the spots on the CCD camera. It can be seen from these pictures that the spot quality is not degenerated by the second BPH and lens. When L_2 was used diffraction limited spots were achieved.

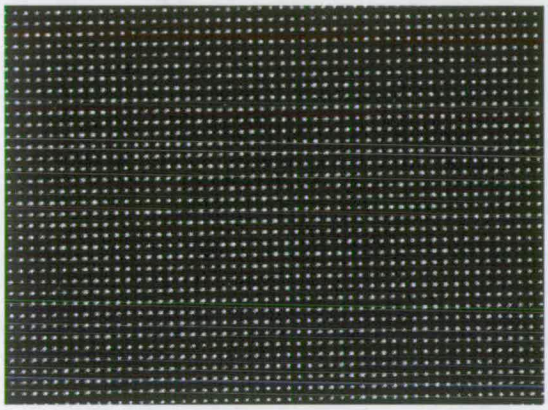

Figure 4.10: Section of the 16×16 array with all spots ON, fanned out to 256×256.

The final output from the system was imaged onto the CCD camera and the following pictures produced. Figure 4.12 shows the output produced when all the spots on both SLMs were turned on. It can be seen from this picture that there are regions in which the contrast ratio is extremely poor. This problem is due to the focal length error in lenses L_1 and L_2 and will be discussed in detail later. Figure 4.13 shows a pattern produced when modulation takes place on both SLMs. The pattern encoded by SLM_1 is as illustrated in Figure 4.9, whilst the pattern encoded by SLM_2 consists of a chequerboard of 4×4 pixels. Thus there are areas in the output pattern which are turned on by one, both, or neither of the devices. This pattern was used for measuring the various contrast ratios which determine the performance of the system. The best results achieved are as follows: (ON-ON Vs. ON-OFF = 7:1) and (ON-ON Vs. OFF-OFF = 75:1). Figure 4.14 illustrates the output of the system when only one channel is turned on by both

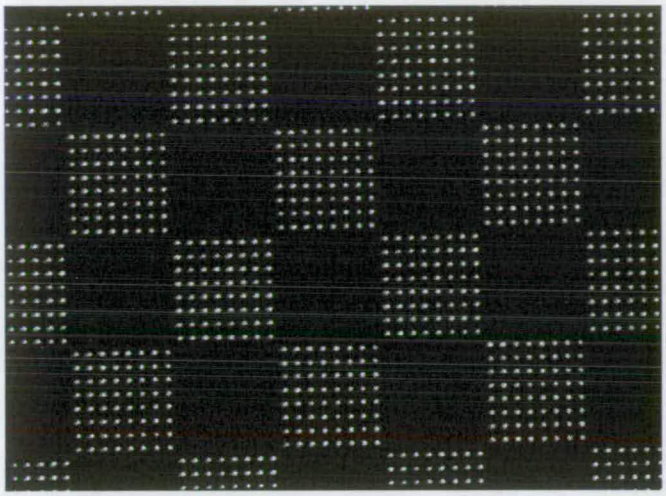

Figure 4.11: Section of the modulated 16×16 array, fanned out to 256×256.

SLMs.

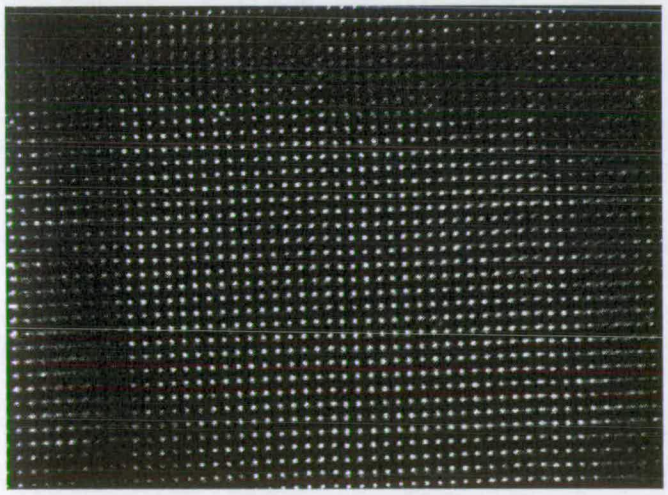

Figure 4.12: Section of the crossbar system output with all the channels turned on.

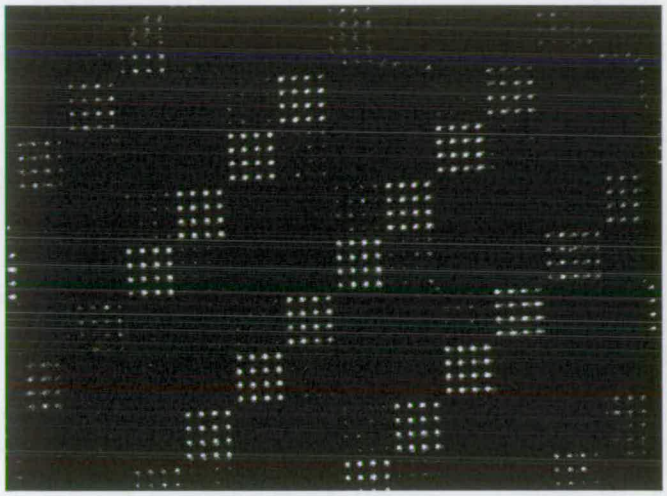

Figure 4.13: Section of the crossbar output with SLM_1 displaying a 8×8 chequerboard and SLM_2 displaying a 4×4 chequerboard.

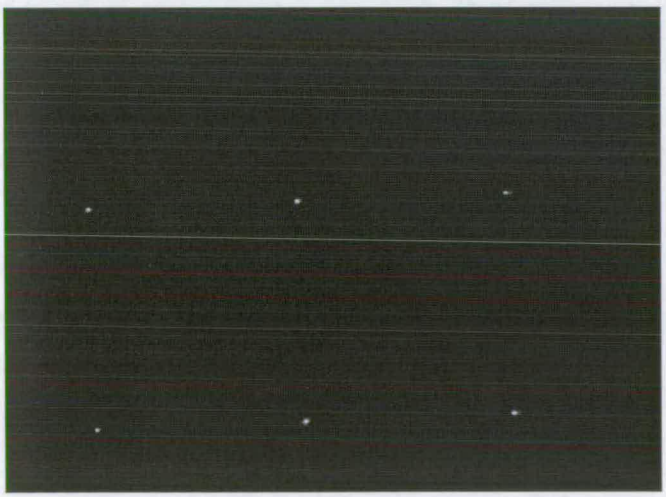

Figure 4.14: Section of the crossbar output when only one channel is turned on by SLM_1 and SLM_2.

4.5 Analysis Of System Performance

The construction of this test system has provided valuable information regarding the scalability of crossbar systems. By assessing the performance of the individual components an analysis can be made of the performance requirements of elements for a full system. In some respects the system has performed much better than initial expectations, as some potential problems did not occur. An example of this was the translational alignment of the SLMs, it was expected that it would be difficult to align the devices initially, and that the alignment would drift-off over a period of time. However by aligning the devices as the system was constructed, with the aid of a CCD camera, it was found that the optimum alignment was achieved without too much difficulty. Once the system had been constructed, it was found that the translational stages did drift slightly, but by viewing the system output it was easy to see how to re-optimise the system without having to dismantle any components. As the positioning stages used in this experiment were not of a high specification, it is believed that using better stages could allieviate this problem altogether.

It is apparent from the previous section that the critical elements of the system are the lenses L_1 and L_2, and the SLMs. These will shortly be discussed in more detail. The performances of the BPHs, PBSs and HWPs were all found to be satisfactory, with the PBSs and HWPs operating well within the manufacturers specifications. It must be remembered however that the performance of these devices is wavelength dependant, and if the system used fibre inputs with laser diode sources, some problems could become apparent due to any wavelength variation between sources. Such problems have been experienced and considered in the OCPM project [57]. This was obviously not a problem in this system.

4.5.1 Lens Performance

The problem of field curvature over large image fields has already been discussed, in this respect however, the lenses were found to perform extremely well, with there being no visible sign of field-curvature or barrel distortion. Although this

application is not what the lenses were designed for, their well-corrected large image fields make them excellent elements for providing structured illumination to large area SLMs. Unfortunately there is one big problem with these lenses and all off-the-shelf lenses, their focal lengths are only precise to an accuracy of ±2%. As the spot spacing is proportional to the focal length of the Fourier Transforming lens (see Equation 3.13), any error in the focal length produces a registration error between the mirrors and the spots. This effect is worsened by using two lenses which have a cumulative error of up to ±4%. This error is illustrated in one dimension in Figure 4.15.

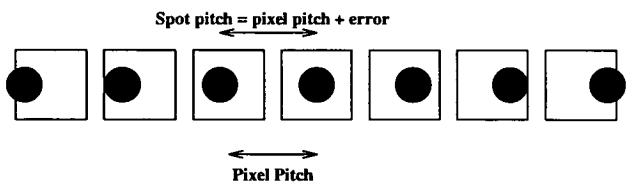

Figure 4.15: Illustration of spot to mirror registration error due to focal length error.

The regions of low contrast in Figure 4.12 are due to the registration error, and the number of pixels illuminated between the fringes can be used to calculate the cumulative error in the focal length of the lenses. This was estimated to be +2.7%, which is within the lenses specification, but obviously severely limits the number of operational output channels. In order for all the 256×256 mirrors to be illuminated by a spot, the cumulative error needs to be $\leq 0.4\%$, leading to an individual lens tolerance of 0.2%, a factor of ten better than the manufacturers specification. There are four possible solutions to this problem:

1. Buy a large number of lenses and test them to select two which when used together, have a cumulative error $\leq 0.4\%$.
2. Buy two lenses, accurately measure their focal lengths, then fabricate the BPHs with their cell-sizes adjusted to compensate for the focal length errors.
3. Custom design lenses which are optimised to reduce focal length variations.
4. Add further optics into the system to allow variable magnification imaging.

Solutions 1 and 2 are infeasible from a commercial point of view due to the time and expense required. Solution 3 is possible [114], but extremely difficult as the lenses also have to be optimised for large image fields etc. Solution 4 is impractical as the introduction of further optics would produce more problems in terms of image distortion. The tight tolerance on the focal length of the lenses is not altered by adjusting either the focal length of the lenses, or the pitch of the SLM pixels.

4.5.2 SLM Performance

The performance of the SLMs is critical to the overall performance of the system. In this system SLM_1 merely acts as an input device, with the optical routing being performed by SLM_2. It is the performance of this device which will now be considered in detail. Referring back to Figure 4.3 it can be seen that each block of 16×16 pixels on SLM_2 corresponds to one output channel, and so only one pixel in that block will be "turned on" at any one time. Thus the signal to noise (S/N) ratio of the output channel is directly linked to the contrast ratio of SLM_2. The other factors which affect the overall system performance are listed below.

- Uniformity of contrast ratio across the device. Any non-uniformity causes variations is S/N ratio for different channels.
- Optical throughput. As there is a high intrinsic fanout loss due to the system architecture, in most applications it is vital to conserve optical power as much as possible.
- Pixel drop out is a serious problem as each pixel corresponds to an output channel.
- The duty cycle of the device has to be taken into consideration. This will be discussed later.
- The device frame rate and liquid crystal switching speed determine the routing latency of the system.

At present the contrast ratio and uniformity of the device are the dominant problems. The contrast ratio is affected by the liquid crystal alignment and cell uniformity.

Uniform alignment is currently proving difficult to achieve over the large areas required by these devices. This has been discussed in detail by Gourlay [53]. Although the device used in this system only has a maximum contrast ratio of 27:1, it is possible that contrast ratios of several hundred to one will be achieved in the future, once the FLC alignment technique has been optimised.

The cell thickness uniformity is, at present, limited by the problem of chip bow. One of the technical problems associated with the planarisation process is the bowing of the silicon which occurs when the wafer is diced into individual chips. This is caused by internal stresses building up between the various layers deposited onto the silicon during the VLSI processing and the planarisation. The various layers have different thermal expansion coefficients. Once the silicon wafer is diced up into chips, this thermally induced stress is released by causing bowing of the silicon substrate. The FLC cell is then made up of an optically flat coverglass and a convex silicon chip, as illustrated in Figure 4.16. When the cell has been filled with FLC, interference rings are visible were the optical path difference on reflection is equal to $\lambda/2$. In these regions the contrast ratio is dramatically reduced as very little light is reflected. When viewed under a microscope with white light illumination, this effect is visible as coloured rings across the device.

In order for FLC/Si SLMs to be improved beyond their present performance, a solution to the problem of chip bow is essential. One possible method of doing this is being investigated by O'Hara [61] and involves the deposition of silicon dioxide pillars across the SLM. These pillars will act as spacers for the FLC cell. The chip can then be pushed hard against the flat coverglass and glued into position. The distribution of the pillars will ensure that the sensitive silicon circuitry/mirrors are not damaged by contact with the coverglass, and that a uniform cell thickness is achieved.

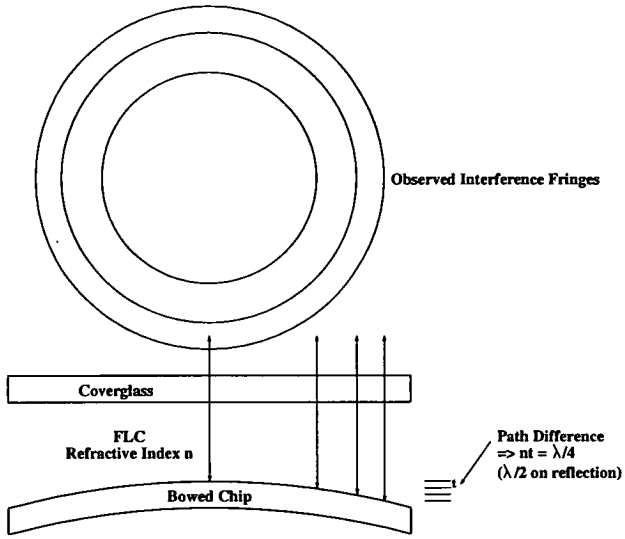

Figure 4.16: Schematic representation of a FLC cell constructed using a bowed silicon chip. The formation of interference rings is illustrated.

In order to estimate the chip flatness required to produce a uniform device, i.e. a device with no interference fringes across the active array as illustrated in Figure 4.17, the following simple mathematical model was used which assumes that the curvature is spherical about the centre of the chip [this has been experimentally verified by O'Hara (private communication)].

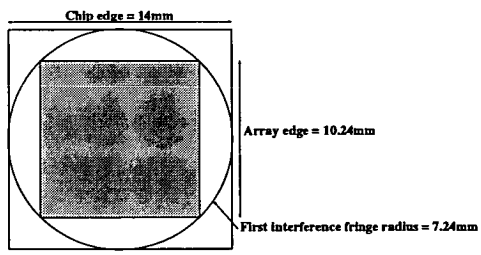

Figure 4.17: Illustration of a uniform device with the first interference fringe occuring outside the active array.

An interference fringe (bright to dark) will occur when the reflected optical path difference $nt = \lambda/2$, where t is the height difference caused by the curvature and n is the refractive index of the FLC. If the maximum height variation along the

diagonal is denoted by a_0 and $2b_0$ is the diagonal of the square chip then it can be shown (from Figure 4.18) that the radius of the first interference fringe is given approximately by

$$b = \left[t \left(\frac{b_0^2 + a_0^2}{a_0} \right) \right]^{\frac{1}{2}} \tag{4.18}$$

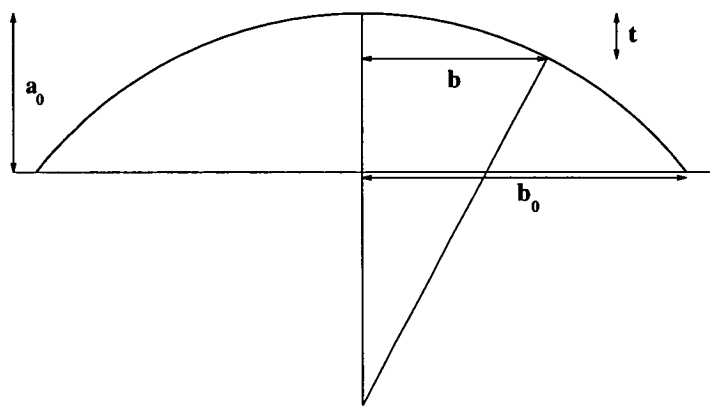

Figure 4.18: Diagram illustrating how the relationship between chip curvature and interference fringe radius can be found.

When the radius, b, of the first fringe is plotted against the chip bow, it is found that a fringe radius of 2mm (uniform circular area of diameter=4mm) corresponds to a chip-bow of approximately 2μm. This deviation value is what has been currently achieved as measured by surface profile measurements taken by O'Hara. It can also be seen that for a uniform device (requiring $b = 7.24$mm), a flatness of 0.175μm is required, as illustrated in Figure 4.19. Thus a significant, but not unachievable improvement is needed.

Once this problem has been solved it may be possible to use 1μm thick cells rather than the 3μm cells used at present. This will have the effect of improving the bistability of the FLC and reducing the switching time. It is also expected that the reduction in cell thickness will increase the optical throughput and improvements will be seen in the contrast ratio. The optical throughput of the device may also be improved by using a material of higher reflectivity than aluminium, such as silver, for the planarised pixel-mirrors, and by using an anti-reflective coating on the front surface of the coverglass.

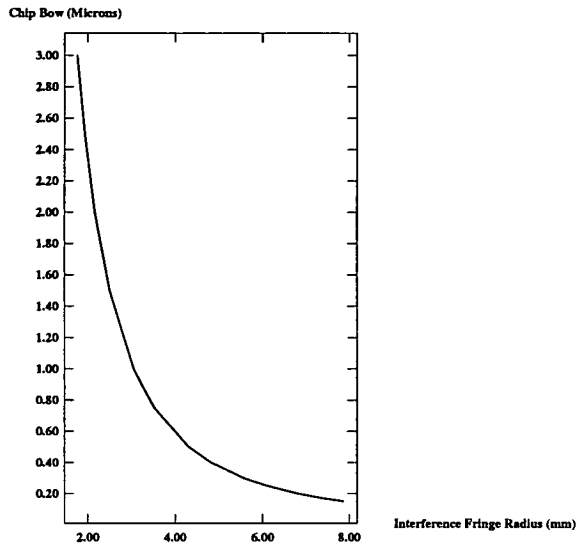

Figure 4.19: Variation of interference fringe radius with chip curvature.

The 256×256 SRAM device has a duty-cycle of 50% due to voltage balancing requirements, so if this device was used in a full system, the transfer of optical data would have to be synchronised with the active phase of the device and information transmitted only 50% of the time. This is obviously an undesirable restriction on the optical data rate. This problem may only be overcome if the liquid crystal exhibits bistability. In which case high duty cycles can be achieved by both SRAM and DRAM addressing schemes.

Finally the problem of pixel drop-out must be considered. As larger arrays are fabricated, smaller geometry CMOS processing must be used. At present this inevitably leads to occasional breaks or shorts occuring in the circuitry. There is little the chip designer can do to improve this, apart from using as large a geometry process as possible. However this has repercussions in terms of the speed and power consumption of the device. As microfabrication technology develops it is hoped that the yield of these devices will improve. At a system level pixel drop-out can only be tolerated if some redundancy is built into the system e.g. two pixels per channel rather than one. This has obvious implications to the system scalability.

4.6 The Scalability Of Crossbar Systems

Although there are several problems with FLC/Si SLMs at present which affect their performance, most are fabrication problems and it is believed that these will be solved as the technology develops. As discussed in the previous section the problem of non-uniform cells is being addressed by O'Hara. It will be assumed in the following discussion that a uniform cell can be produced. The results obtained from the test system show that the following factors directly influence the scalability of the system.

- The tolerance of the focal length of the lenses L_1 and L_2.
- The contrast ratio of the FLC cell.
- Pixel drop-out.

The focal length tolerance is the primary limiting factor, which cannot be allieviated as the tolerance does not change with pixel pitch or lens focal length. It is only proportional to the number of pixels on the SLM. Figure 4.20 illustrates the variation of focal length tolerance with the number of pixels. There is also a compromise to consider regarding the pixel pitch. As larger devices are fabricated it is often neccessary/desirable to reduce the pixel pitch. As the pixel pitch reduces smaller diffraction-limited spots are required to address the device. In order to reduce the spot size, the aperture of the system needs to increase. This implies that the focal length of the lenses also needs to be increased in order to re-collimate the spots up to a large diameter beam. However as the pixel pitch is reduced, the BPH cell size has to be increased to compensate, and as the focal length of the lens is increased, the cell size has to increase further. If the BPH cell size becomes so large that very few replications can be incorporated then the spot quality degenerates. Thus there is a compromise between the number of pixels and the pixel pitch.

The contrast ratio of the SLM is also an important factor which limits the scalability of the system, although to some extent it is dependent upon the specific system

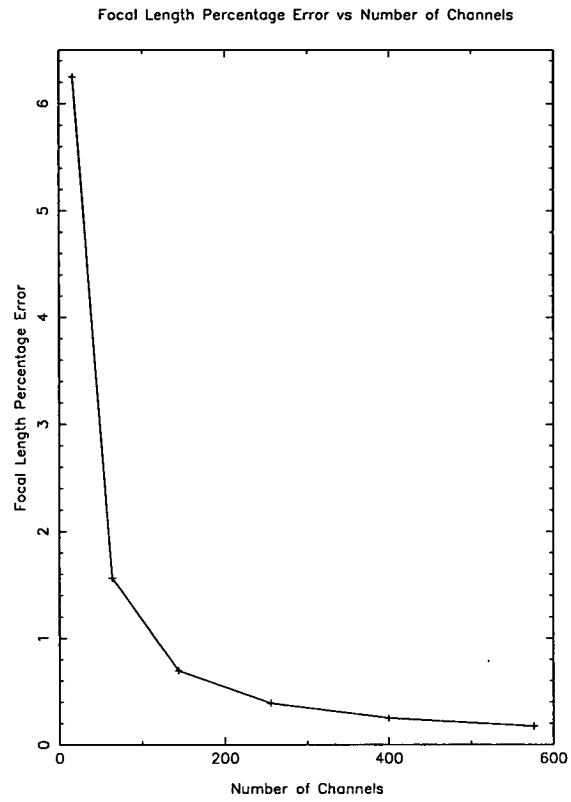

Figure 4.20: Variation in the tolerance of lens focal length error with the number I/O channels.

application. By referring to Figure 4.3 it can be seen that the light incident on an output channel consists of one ON channel plus N-1 OFF channels, where N is the number of input channels. Thus for the S/N ratio of the output to be 1:1, the contrast ratio of the SLM needs to be N-1:1, i.e. for the 256 channel system studied here, a contrast ratio of 255:1 is required for SLM_2. This is well above what can currently be achieved using this SLM technology, but is not unrealistic in the future. However it is possible that this high specification is not necessary if the output of the system is incident upon an electo-optic device rather than a fibre array. In this case it may be possible to apply some electrical/optical thresholding to recover the signal from the noise created by all the channels.

Finally fibre input and outputs must be considered. In such large systems (>100 channels) it may well be infeasible to construct fibre arrays, especially for the input array as the angle of polarisation needs to be aligned between each channel. Due to this, large crossbar systems may be limited to using electro-optical devices or SLMs for the input and output, as illustrated in this test system.

4.7 Summary

In this chapter a 256 channel crossbar test system has been described which has been used to assess the scalability of crossbar systems implemented using FLC/Si SLMs. The fanout has been achieved using two cascaded 16×16 BPHs manufactured using the fabrication technique described in Chapter 2. Optical results have been presented which illustrate that the performance of the system was severely limited by the cumulative focal length error of the lenses used to focus/re-collimate the spots onto the SLMs. This problem has been discussed and it has been shown that this is the most critical tolerance when scaling such systems. Factors such as contrast ratio and cell uniformity have also been considered.

It can be concluded from this work, that given techical improvements in the performance of the FLC/Si SLMs, a fully working system based on the architecture presented in this chapter would be feasible, although it would be difficult to produce on a large commercial scale. The lens focal length error tolerance is very high, but not unachievable using current lens design/fabrication techniques.

Chapter 5

Dynamic Holographic Routing System

5.1 Introduction

In this chapter experimental work will be presented which uses the binary phase modulating properties of FLCs to produce *dynamic* Binary Phase Holograms (BPHs) on the 256×256 SLM. The dynamic holograms are then used in an optical routing system which routes a single input channel into an array of 4×2 output fibres, with multicast and broadcast capabilities. The results from this system are used to consider the design of a full system based on the 256×256 SLM which, it will be shown, can route up to 32 channels. Finally the scalability and performance of dynamic holographic routing systems will be discussed.

5.2 Review Of Other Work

The earliest work in this field was performed using magneto-optic SLMs [115][116] which demonstrated that Fourier and Fresnel holograms could be written onto a pixellated SLM and successfully reconstructed. Adapted liquid crystal displays have also been used to illustrate optical routing using dynamic holograms [31][117]. However the most thorough study of this field has been performed by O'Brien et.al. [118][119][120]. By implementing the BPHs on a transmissive FLC

EASLM they have performed initial studies into the capabilites of these devices for holographic routing networks. They have also shown that the Space-Bandwidth-Product (SBWP) of the BPH can be improved by replicating the holographic pattern from the EASLM onto an OASLM using a static BPH [121] as illustrated in Figure 5.1. The original holographic pattern is written onto an electrically addressed transmissive SLM. The pattern is then replicated into an array of holographic patterns which is incident onto the OASLM. This process allows the cell size to be reduced and a large number of cells to be replicated side by side, increasing the SBWP. The improved holographic pattern on the OASLM is then optically interrogated by a second laser. They have also produced asymmetric fanouts by using a static BPH in conjunction with a transmissive FLC EASLM [122]. Broomfield et.al. [123] have also produced BPHs on a transmissive FLC EASLM. At present the only known published work using reflective FLC/Si SLMs to produce BPHs has been performed at The University of Edinburgh [124][125][126].

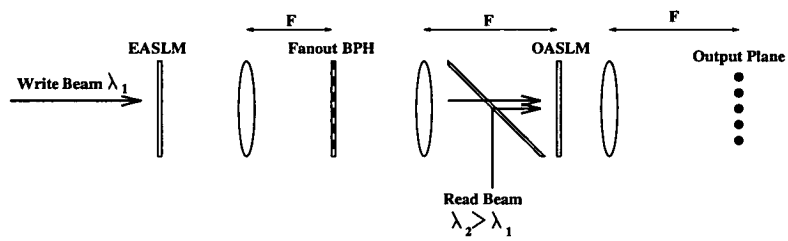

Figure 5.1: Replicating a BPH onto an OASLM as demonstrated by O'Brien et.al.

5.3 Dynamic Holograms On The Planarised 256×256 SLM

In order to assess the quality of the spot arrays produced by writing a BPH pattern onto the SLM, it is important to consider the effect of the device pixellation on the output. Consider the light in the back focal plane of the Fourier Transforming lens in Figure 5.2. If the HWP has been rotated to optimise the device for phase modulation and all the mirrors are turned ON (or OFF) then the lens produces the Fourier Transform of the input plane wave (a Delta function) convolved with a

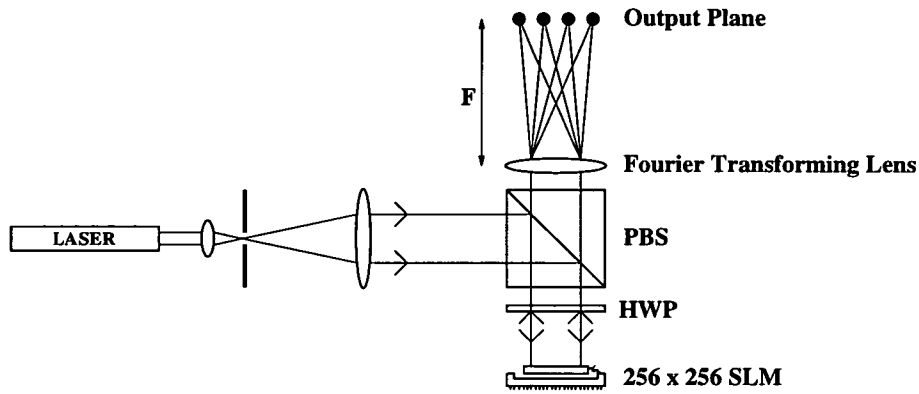

Figure 5.2: Optical System for generating dynamic BPH spot arrays.

function describing the Fourier Transform of the aperture function of the system (a sinc function) and so produces an on-axis spot (DC spot) in the back focal plane. However the pixellated mirrors act as a two-dimensional diffraction grating [127] so the DC spot is surrounded by an infinite square array of diffracted spots. The spacing between the diffracted orders is governed by the pitch of the SLM pixels (see Equation 3.2). The relative intensities of the diffracted orders are a function of the fill-factor of the pixel and can be found by calculating the Fourier Transform of the reflection function of the SLM. If a pixel with reflection function p(x,y) has a square mirror of edge length a, and the SLM consists of N pixels located on a array of pitch d and edge length D ($D = Nd$), then the Fourier Transform, in one dimension is given by;

$$\text{FT of} \left[\left[\text{p(x)} \odot \sum_{j=-\infty}^{\infty} \delta(x - jd) \right] \Pi \left(\frac{x}{2D} \right) \right] \tag{5.19}$$

$$\text{This equals P(u)} \times \sum_{j=-\infty}^{\infty} \delta \left(x - \frac{j}{d} \right) \odot \frac{\sin(\pi D u)}{\pi D u} \tag{5.20}$$

Where $\odot$ denotes the convolution function. In two dimensions P(u,v) is given by;

$$\text{P(u,v)} = \frac{\sin(\pi a u)}{\pi a u} \frac{\sin(\pi a v)}{\pi a v} \tag{5.21}$$

Thus the intensity of the replications is governed by $|P(u,v)|^2$. The relative intensities of the replications compared to the undiffracted image are given by;

$$\left|\frac{\sin(\pi a \frac{m}{d})}{\pi a \frac{m}{d}}\right|^2 \tag{5.22}$$

Where m represents the mth replicated order. Using this equation it has been calculated that the relative intensities of the first and second order diffracted peaks (m=1, m=2) for the 256×256 SLM (N=256, d=40μm, a=37μm) are 0.65% and 0.61% respectively.

However when the intensities of the diffracted spots were measured experimentally, they were found to have the following relative intensities;

0.36%	1.9%	0.42%
4.32%	DC	2.86%
1.17%	3.83%	0.19%

Clearly these measured values are substantially higher than those predicted by this simple diffraction model. Furthermore simple diffraction does not account for the uneven (m=-1 $\neq$ m=+1) diffracted orders observed. However there are two factors which account for these discrepancies. The mirror area is not flat due to a hole over the via connection to the original mirror, as shown in Figure 2.13. This will have the effect of increasing the intensity in the replicated orders as the effective mark-space ratio is reduced. The non-uniformity of the diffracted orders occurs because the via hole and inter-pixel gap are not "black" areas as supposed by the simple theoretical model. Light is reflected from these areas, but undergoes a phase shift relative to the rest of the light because it passes through the silicon dioxide planarisation layer and is reflected from the underlying circuitry. It is thought that

this phase shift causes the uneven intensity distribution in the replicated orders. An example of the diffracted spots due to the pixellation is shown in Figure 5.3. To avoid any confusion arising later, the diffracted orders which are present due to the pixellation of the device will be referred to as replicated orders. Any spot array produced by a BPH written onto the SLM will be reconstructed around each replicated order. However only the 0th order is of use and so it is important to maximise the amount of light present in this order.

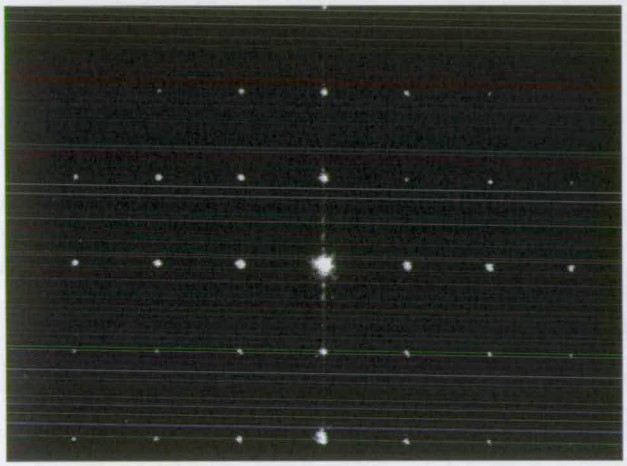

Figure 5.3: DC Spot and replicated orders due to the SLM pixellation.

For the reconstructed BPHs to be optimised it is important that the HWP has been rotated to optimise the performance of the device for binary phase modulation. This can be achieved using the optical system illustrated in Figure 5.2 with a pinhole/photodiode interrogating the DC spot. By viewing the output signal from the photodiode on an oscilloscope and flipping the array of mirrors between their ON and OFF states, the system can be optimised for phase modulation by rotating the HWP until the intensity transmitted into the DC spot from both states is identical (i.e. zero amplitude modulation). This can be achieved to a high degree of accuracy using a digital oscilloscope which provides D.C. offset and scaling facilities. Figure 5.4 illustrates this with the top trace displaying the voltage applied to the front electrode of the SLM and the second trace showing the voltage output signal from the photodiode.

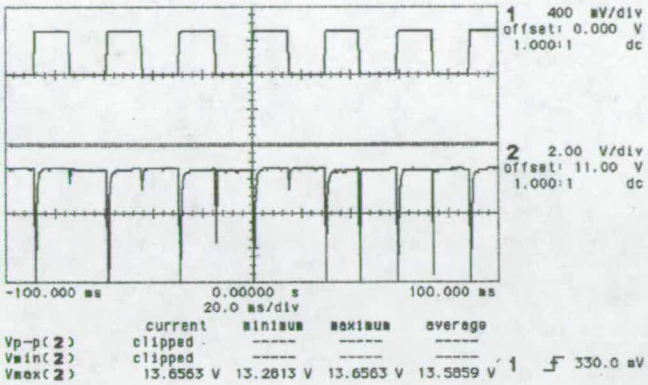

Figure 5.4: Oscilloscope traces showing (top) SLM front electrode voltage and (bottom) output from photodiode interrogating the DC spot.

To assess the performance of the SLM as a phase modulating element a simple grating pattern was used. The grating had a period of four pixels with two columns turned ON, and two OFF. [A grating with a pitch of two pixels could not be used as the diffracted spots from the grating, replicated about the spots generated by the pixellation, would overlap, giving inaccurate measurements]. The system was optimised for phase modulation as previously described and the following measurements taken using a pinhole/photodiode. The incident collimated beam had a diameter of 2mm and was reflected from the most uniform part of the SLM.

- Light transmitted into DC spot (Optical Throughput) = (9.1±0.1)%.
- Diffraction efficiency in 0th order = 85% ± 2%.
- Diffracted spot (ON:OFF) contrast ratio = (305±5):1.
- $\frac{\text{Diffracted spot intensity}}{\text{DC spot intensity}} = (90\pm2):1.$

These results illustrate the large improvement in performance achieved by planarisation [125]. An important consideration is the increase in the fill-factor of the SLM as this directly affects the amount of light which propagates into the 0th replicated order as shown by Equation 5.22. The high diffraction efficiency and

diffracted spot to DC spot ratio confirm that the device exhibits excellent phase modulating properties. The 2mm aperture used for taking these measurements was neccessary due to the non-uniformity of the FLC cell, caused by the bowed silicon substrate as discussed in Section 4.5.2. As the aperture of the incident beam is increased, the quality of the spots in the output plane degenerate, and suffer from coma, which occurs when a parallel beam is reflected from a plane inclined to the optic axis. This leads to a compromise between spot quality and spot size which also will be considered in more detail in Section 5.5. Figure 5.5 illustrates the output from the optical system, with all the mirrors ON (DC spot) and with the grating pattern written onto the SLM (2 diffracted spots).

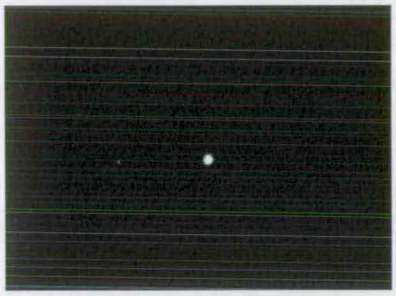

(a)

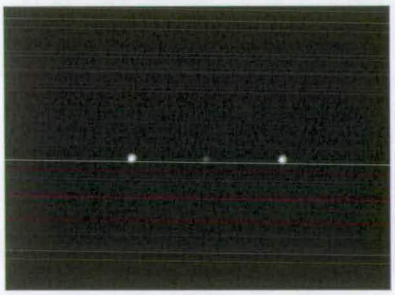

(b)

Figure 5.5: Output from optical system showing (a) 0th order DC spot present when all the mirrors are turned on, and (b) Diffracted spots when a grating is written to the SLM.

There are a number of factors which need to be considered when designing and using BPHs on pixellated SLMs. The first consideration is the number of pixels per hologram cell. A BPH unit cell of $n^2 \times n^2$ pixels is only capable of producing a fanout of up to $n \times n$ spots. Thus a BPH unit cell of 16×16 pixels can only produce arrays of up to 8×8 spots. However a BPH unit cell of 32×32 pixels could produce a 8×8 spot array with better uniformity as the transition points can be more precisely defined. The spacing of the spots would be halved as the cell size was doubled. This can only be counteracted by altering the focal length of the Fourier Transforming lens. A second factor to be considered is the aperture of the incident beam available for illuminating the BPH. In order for the image stored in the BPH to be reconstructed faithfully, at least one whole unit cell needs to be illuminated. So in reality a 2×2 array of cells is the minimum requirement [74]. However if the unit cell is so large that the beam suffers coma due to the warped backplane, then the spot quality is degraded and there is no gain from using more pixels than necessary to define the BPH unit cell pattern. Furthermore as the beam diameter is reduced to improve the spot quality, the diameter of the output spot increases as determined by Equation 3.11, so if the output consists of a large number of spots they may not be individually resolved. Thus it can be seen that there are several compromises regarding the number, size, and quality of the spots in the output plane. Figure 5.6 shows a 4×4 BPH pattern, based on a 16×16 pixel unit cell, written onto the planarised 256×256 FLC/Si SLM. Figure 5.7 shows the output from the optical system when this pattern is written onto the SLM and illuminated with a 2mm diameter beam.

The intensity uniformity of the spots was measured and found to vary by ±14%, with the outer spots being less intense. This is much poorer than the theoretical perfromance of the BPH (±4%), and is again attributed to the pixellation of the SLM. Equation 5.22 shows that the intensity of the replicated orders is controlled by a $\frac{\sin(\pi \frac{a}{d})}{\pi \frac{a}{d}}$ envelope. Thus the intensity of any spots generated by a BPH must lie within this envelope, and so their uniformity is affected. This is illustrated in Figure 5.8. Figure 5.9 shows a 8×8 fanout array, which is the largest array which can be achieved on this device due to the warped silicon substrate. In this case the DC spot is visible as the image stored in the BPH cannot be perfectly reconstructed when based on a 32×32 pixel cell. However the DC spot is of similar intensity to the other spots in the array.

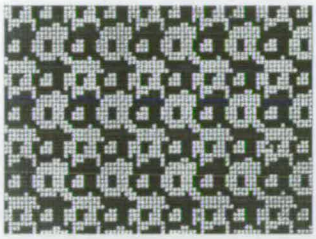

Figure 5.6: A BPH pattern, which produces a 4×4 spot array, written onto the SLM.

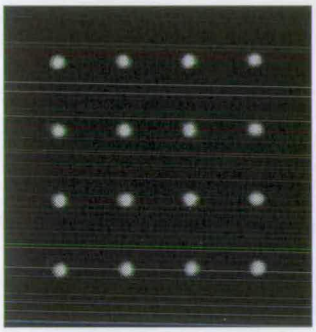

Figure 5.7: 4×4 spot array produced by a 2mm diameter input beam, the DC spot is of such low intensity it cannot be seen.

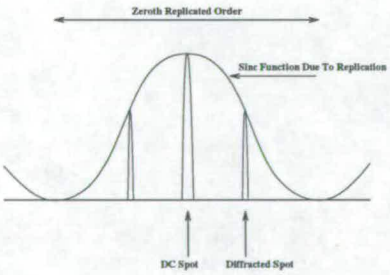

Figure 5.8: Illustration of reduction in diffracted spot uniformity due to Sinc envelope produced by the pixellation

Finally two points must be noted regarding the device and interface. Due to the DC balancing scheme described in Chapter 2, the output is only present for 50% of the time. Also, as only a simple interface was used in this work, the maximum achievable frame rate is 100Hz, with several seconds being required to change the pattern. However, using a more complex interface with on-board memory, different patterns could be displayed on the device at a frame rate of up to 3kHz.

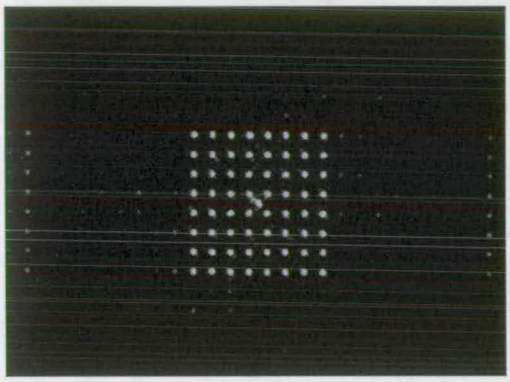

Figure 5.9: 8×8 Dynamic fanout produced by the 256×256 SLM.

5.4 1-To-8 Channel Routing Network

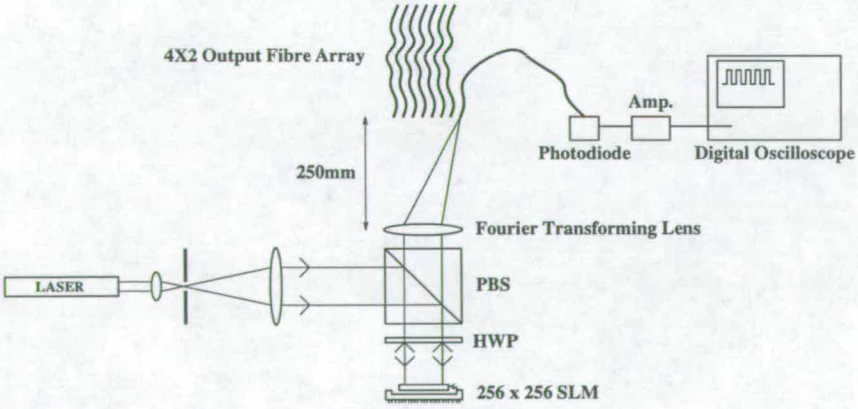

Figure 5.10: 1-to-8 Channel dynamic hologram free-space routing system.

In order to demonstrate the use of dynamic holograms in free-space routing systems, and to assess the scalabilty of such systems, a 1-to-8 routing system has been constructed. The layout of the system is shown in Figure 5.10. A single input beam was routed to an output array of 4×2 output fibres, with mulitcast and broadcast capability. The fibre array was constructed from 250μm plastic fibres on a 500μm pitch mounted in a perspex holder through which holes were drilled. A 4×2 array was used so that the BPHs could be based on a 4×4 fanout array (due to the binary nature of the holograms only half of the 4×4 array could be uniquely addressed). It was decided to use a shifted 4×2 fanout array as illustrated in Figure 5.11 in order to keep the channels as far away from the DC spot as possible.

Holograms were designed which routed the input beam to each individual channel (1-to-1 routing) and to all channels (broadcast). Figure 5.12 shows the hologram pattern and output which routes to all channels, and Figure 5.13 shows the hologram patterns and associated outputs which route to the individual channels. The holograms were based on a 16×16 unit cell which gave a cell size of 640μm. Thus when a 250mm focal length Fourier Transforming lens was used, the resultant spot spacing was approximately 500μm to map onto the fibre array.

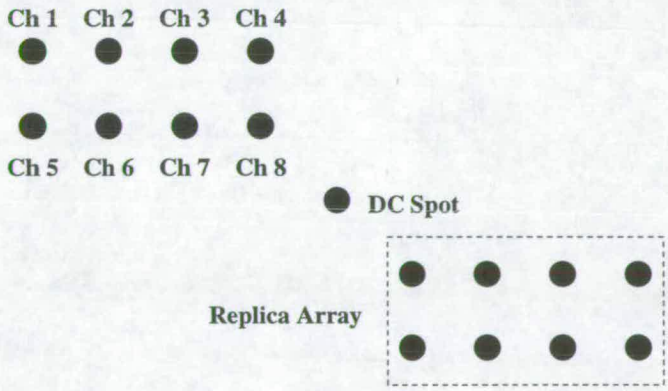

Figure 5.11: Shifted 4×2 Fanout array for use in the routing system.

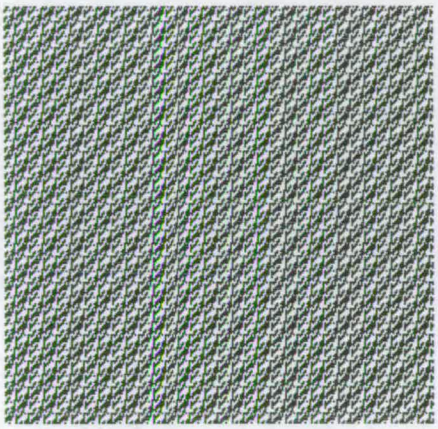

4×2 Fanout BPH pattern

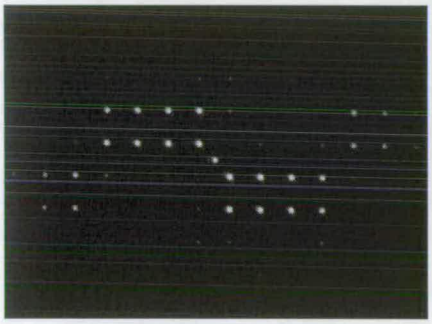

Corresponding optical output

Figure 5.12: Shifted 4×2 BPH and optical output (broadcast mode).

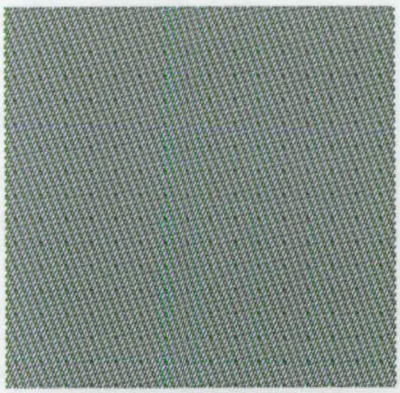

Channel 1 BPH Pattern

Channel 1 Optical Output

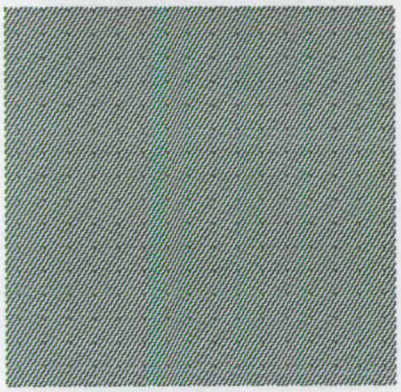

Channel 2 BPH Pattern

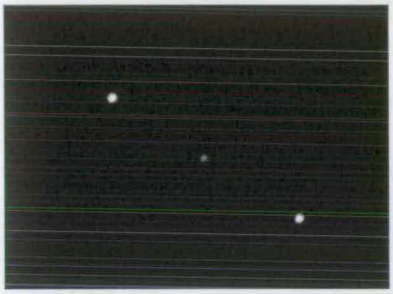

Channel 2 Optical Output

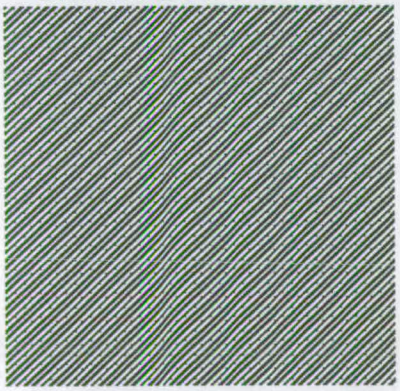

Channel 3 BPH Pattern

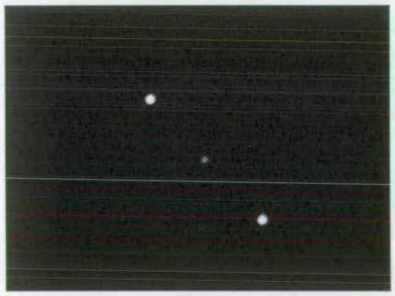

Channel 3 Optical Output

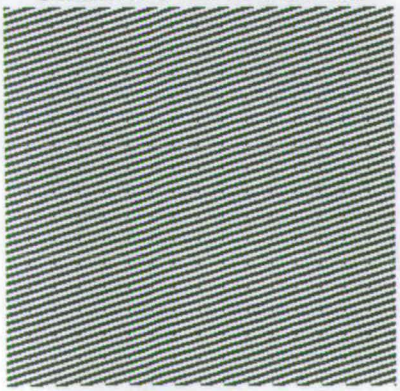

Channel 4 BPH Pattern

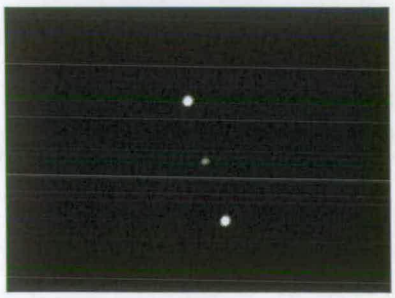

Channel 4 Optical Output

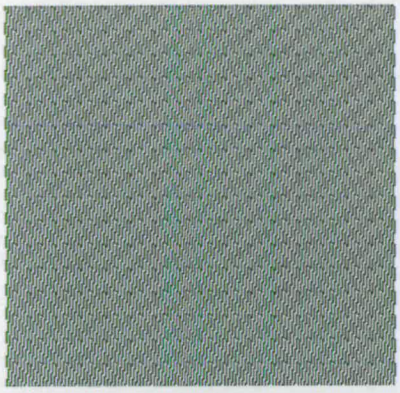

Channel 5 BPH Pattern

Channel 5 Optical Output

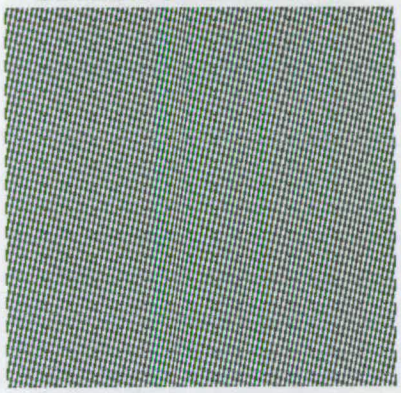

Channel 6 BPH Pattern

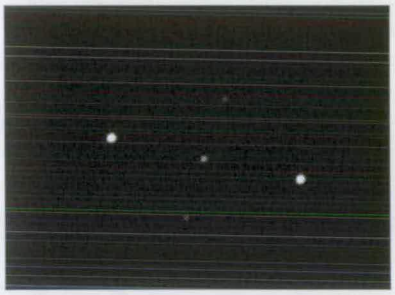

Channel 6 Optical Output

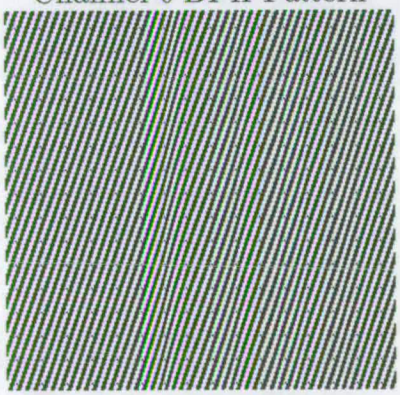

Channel 7 BPH Pattern

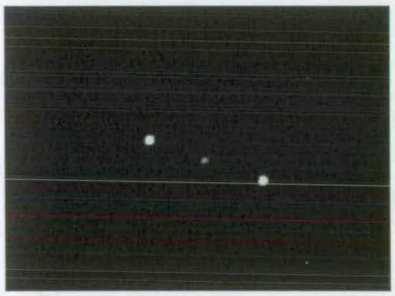

Channel 7 Optical Output

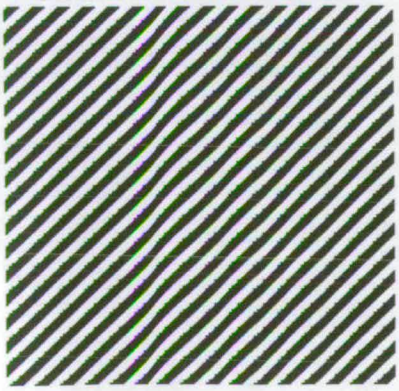

Channel 8 BPH Pattern

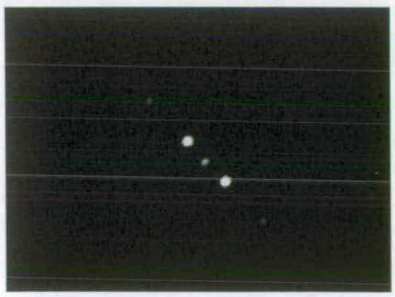

Channel 8 Optical Output

Figure 5.13: Hologram patterns and corresponding optical outputs to route to a single output channel.

To measure the amount of light transmitted into the fibres, a large area photodiode was used. The photodiode was mounted in a black metal container filled with paraffin, which had a hole in the lid through which the fibres could be inserted. The liquid paraffin was used to act as an index matching medium allowing the light to be coupled from the fibre to the photodiode. The output of the photodiode was connected, via an amplifier, to a digital storage oscilloscope, as shown in Figure 5.9. This allowed peak-to-peak voltage measurements and time-averaged measurements to be obtained automatically. Using this apparatus it was found that the optical system produced extremely good results, which are given in Table 5.1. Figure 5.14 show three sets of traces obtained when the system was routing light into channel 4. These traces illustrate the high intensity transmitted into the output channel, the negligable crosstalk occuring into channel 3, and the small but measureable signal apparent in channel 8 due to its close vicinity to the DC spot.

	CHANNEL NUMBER							
	1	2	3	4	5	6	7	8
Channel (ON) 1	6.375	0.035	0.025	0.023	0.044	0.023	0.020	0.260
2	0.020	7.875	0.060	0.023	0.025	0.045	0.028	0.335
3	0.024	0.025	8.685	0.060	0.022	0.026	0.017	0.270
4	0.024	0.022	0.026	8.875	0.020	0.018	0.023	0.262
5	0.042	0.024	0.030	0.020	6.425	0.028	0.022	0.256
6	0.025	0.020	0.020	0.021	0.022	8.155	0.018	0.300
7	0.025	0.033	0.050	0.027	0.023	0.024	8.765	0.260
8	0.022	0.026	0.618	0.056	0.028	0.023	0.024	8.625
Contrast Ratio	200:1	133:1	108:1	90:1	212:1	155:1	94:1	33:1
Average S/N Ratio	105:1	103:1	137:1	157:1	107:1	134:1	139:1	76:1
Diffraction Efficiency (X2) %	56	70	83	85	66	77	86	61

Table 5.1: Table showing the optical measurements taken from the dynamic hologram routing system.

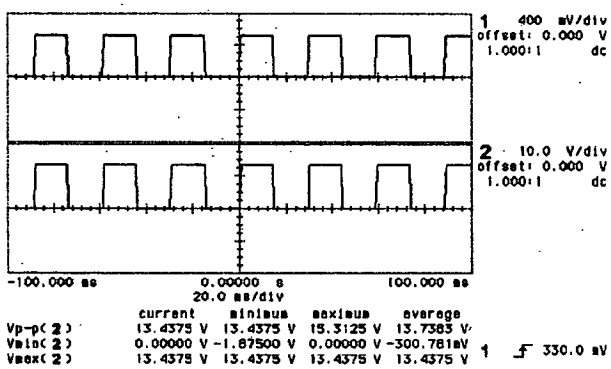

(a)

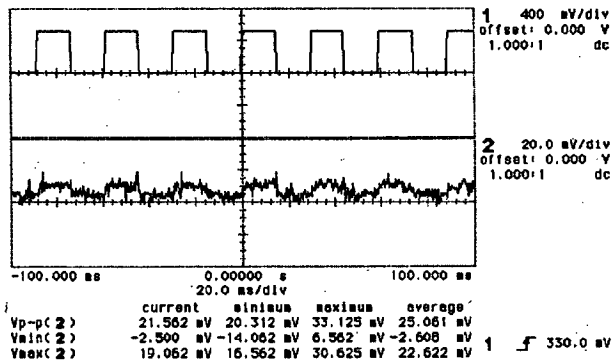

(b)

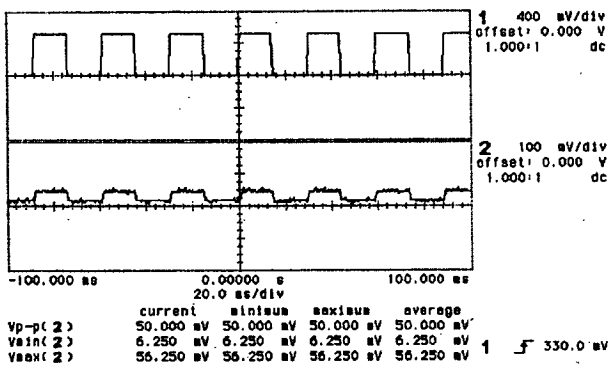

(c)

Figure 5.14: Oscilloscope traces illustrating output photodiode voltages when channel 4 is being illuminated. In each graph the top trace corresponds to the SLM front electrode voltage. Signal from (a)=channel 4, (b)=channel 3, (c)=channel 8.

The following points of interest can be observed from Table 5.1.

- In all cases the noise is higher in channel 8 due to light from the DC spot entering the fibre.
- For all channels the S/N ratio is sufficiently high for the system to be practical, although it would improve considerably to ≈300:1 if less noise was present in channel 8.
- The Diffraction Efficiency measurements illustrate how the spot intensity decreases with distance from the DC spot due to the intensity envelope discussed previously.
- The contrast ratio on all channels is very high, allowing the presence of signals to be easily detected.
- When channel 8 is illuminated, there is a larger than average noise signal in channel 3. This is due to the BPH design, channel 3 is in a position such that it is a higher diffractive order than channel 8 (on the diagonal from the DC spot), and so the BPH also focuses some light into this channel.

In this experiment 250μm fibres were used as there were no facilities for making fibre arrays with smaller fibres. However the use of smaller diameter multimode fibres would have reduced the crosstalk between channels even further. The calculated diffraction limited spot size was 95μm for this system, and the actual spot sizes were found to be 110$\pm$10μm. Thus 150μm diameter fibres could be used without any decrease in optical throughput, although more precise alignment may be needed.

This system has illustrated that optical routing can be performed using dynamic holograms on a FLC/Si SLM. Although this has demonstrated routing between only eight channels, the optical performance of this system implies that a larger system is feasible. Before considering this further the performance of the SLM will be considered in more detail.

The following reflectivity measurements were taken:

- Reflectivity (into DC spot) of bare silicon backplane = (50.6±0.7)%
- Reflectivity from complete SLM = (24.9±0.6)%

Although these measurements are high compared to previous devices and devices fabricated by other research groups [56], they are still by far from optimised. The reflectivity of the backplane could be improved by increasing the pixel fill-factor, as previously discussed, and also using a higher reflectivity metal than aluminium for the planarised mirrors. Silver would be a suitable alternative. The reflectivity drops by 50% once the coverglass and FLC are in place. This loss has two primary sources, reflections from the various interfaces on the coverglass and absorption/scatter by the FLC. It would be difficult to reduce the reflections from some of the interfaces on the coverglass, such as the glass-ITO interface, but an improvement could be made by employing a single magnesium flouride anti-reflection coating on the top of the coverglass. The transmission through the FLC could be improved by reducing the cell thickness from 3μm to 1μm. This would also have the effect of increasing the FLC switching speed. It is possible that better FLC alignment would also reduce scatter.

As in the case of the crossbar system, the chip bow severely hampers the performance of the device, by limiting the aperture of the input beam capable of producing undistorted spots and also the complexity/cell size of the BPHs that can be used. Finally, as mentioned in Chapter 2, significant improvements in optical throughput could be realised by using a FLC with a switching angle of 45°. This would produce linearly polarised light with the required π relative phase change, thus no output polariser would be required and the optical throughput would theoretically be 100%.

5.5 Feasibility Of A Full System Using The 256×256 SLM

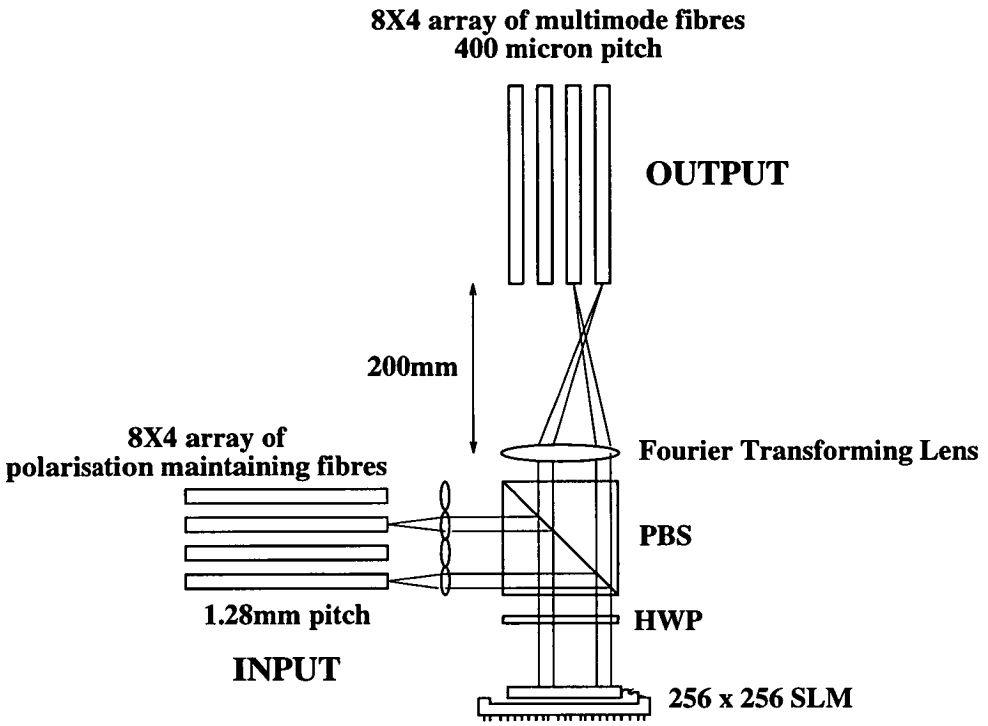

Figure 5.15: Layout of a full optical routing system using the 256×256 SLM to provide dynamic holographic interconnects.

A complete dynamic hologram routing system could be constructed as illustrated in Figure 5.15. Each input fibre is collimated by a micro/mini lens to illuminate a separate block of the SLM. These blocks each display different holographic patterns to route the beams to the requested output channels. Due to the shift-invariance of the Fourier holograms, only a single lens is required to focus the reflected light into the output fibres. It can immediately be seen from this architecture that the system does not suffer from the same intrinsic fanout loss as the crossbar architecture. This architecture was first presented by O'Brien et.al [120].

In order to assess the maximum number of channels that the 256×256 SLM can route using dynamic holograms, the following factors must be considered.

1. The number of pixels per unit cell of the BPHs is related to the number of discrete spots that the BPH is required to address.
2. The input beams must have a large enough diameter so that when focused back down, their diffraction-limited spot size is small enough for the light to enter the output fibre.
3. The BPH cell size must be such that a Fourier Transforming lens of reasonable focal length can be used to focus the spots with a suitable inter-spot spacing.
4. As each BPH produces two spots, this must be taken into account when considering the symmetry of the system.

When all these factors are considered, it can be calculated that the maximum number of individual channels that can be directly routed using the 256×256 SLM is 32. This is based on 8×4 input and output fibre arrays, and allows the BPHs to be based on an 8×8 spot array, solutions for which can be calculated on a 16×16 pixel unit cell. Thus each input channel is required to illuminate at least 32×32 pixels (2×2 cells). Hence all 256 pixels are required in one dimension. In order to satisfy (4) only 4 channels are possible in the other dimension, requiring 128 pixels. In this case the diameters of the input beams will be ≈1.2mm. If a Fourier Transforming lens of focal length = 200mm is used, then 260μm diameter diffraction-limited spots will be produced on a pitch of approximately 400μm. The layout of the beams and BPHs on the SLM is illustrated in Figure 5.16.

The scalability of these systems is not as straightforward as for the crossbar architecture, due to the tradeoff between output spot size and beam diameter. A reduction in the SLM pixel size would decrease the BPH cell size and hence increase the angle of diffraction, resulting in a greater inter-spot spacing. This would reduce crosstalk and make the fibre array fabrication easier. However if the input beam diameter was then reduced in order to increase the number of channels, the diffraction-limited spot size would increase, counteracting any gain.

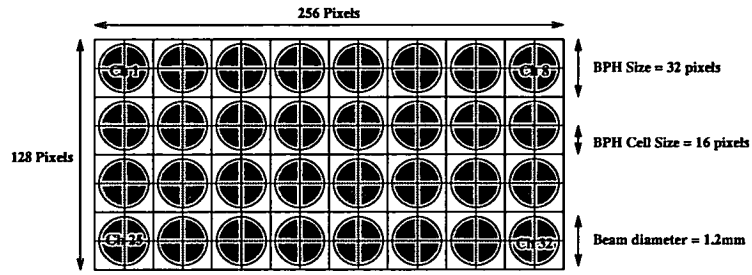

Figure 5.16: Positioning of input beams and holographic patterns on the SLM.

The greatest gain to be made from reducing the pixel size can be achieved as follows. If the pixel size is reduced, by say a factor of 2, then for a given focal length lens, the spot spacing will double. If the input beam diameter is kept constant then the beam will encompass a 4×4 array of cells rather than the minimum 2×2 array. If the focal length of the lens is then halved, the spot spacing returns to its original value, but the diameter of the diffraction-limited spot is half its original value. Thus decreasing the pixel size directly reduces the size of the output spots and also reduces the overall size of the optical system.

In order to increase the number of channels, the number of pixels must increase. This matches an attempt to decrease the pixel size. However as the number of channels increases the number of pixels per channel required also increases. This is illustrated in Figure 5.17 which shows the variation of the maximum number of achievable channels with the number of pixels on the SLM. It can be seen from this graph that a 128 channel system would require 1024×1024 pixels. Such a device is ambitious, but not infeasible using sub-micron VLSI processing and DRAM pixel addressing.

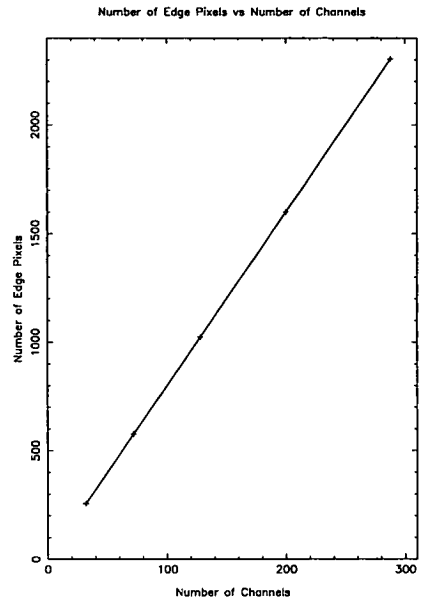

Figure 5.17: Variation of the maximum number of I/O channels of a dynamic holographic routing system with the number N of edge pixels on the SLM with N^2 pixels.

5.6 Summary

In this chapter we have described how FLC/Si SLMs can be used as dynamic holographic elements by writing holographic patterns onto them amd operating them in phase modulation mode. The performance of a 256×256 FLC/Si SLM has been assessed as a dynamic holographic element and been used in an optical system which can route a single input beam into a 4×2 array of fibres. This system has been fully characterised and the low crosstalk of the system illustrated. Finally the results obtained from this system have been used to study the scalability of optical routing systems implemented by pixellated SLMs displaying holographic patterns. It has been shown that the 256×256 device could route up to 32 channels, and 1024×1024 pixels would be required to route 128 channels.

Chapter 6

Discussion And Conclusions

6.1 Introduction

In this concluding chapter the work presented in this thesis will be summarised, and some of the issues that have arisen from this work discussed. In particular the performance of the two routing systems will be compared and conclusions drawn about their applications. Finally some ideas for continuing this work will be described.

6.2 Silicon Nitride On Sapphire Binary Phase Holograms

A fabrication technique for manufacturing binary phase holographic elements has been described. A phase modulating layer of silicon nitride is deposited by low-pressure-chemical-vapour-deposition onto a sapphire substrate. The thickness of this layer can be controlled to a high degree of accuracy and the uniformity of the deposition is excellent. This film is then patterned and etched, with the sapphire acting as an ideal etch-stop, allowing the normally strict etch conditions to be relaxed.

This process results in a high yield of binary phase holograms, all showing near optimum performance. The high yield is of great importance if free-space optical routing systems are to be produced on a large scale for say, telecommunications systems. Optical results of this process have been presented including an image containing 91 grey levels and a 64×64 fanout hologram. Finally a 256×256 fanout has been demonstrated using two cascaded 16×16 fanout elements. This is the largest fanout array published so far as we are aware.

6.3 The 256-Channel Crossbar System

The input and modulation planes of a 256-channel crossbar have been constructed using two 256×256 FLC/Si SLMs and cascaded binary phase holograms. By assessing the performance of this system, the scalability of crossbars has been investigated. It has been found that there are two critical issues which limit the scalability. As the number of channels in the system increases the tolerance on the focal length of the Fourier Transforming lenses is found to become extremely difficult to achieve. For the 256-channel system to work fully, a cumulative focal length error of less than 0.4% is required. When the system is scaled to 576 (24×24) channels, the permissible variation reduces to less than 0.2%. The performance of the SLM also affects the scalability. The performance is severely limited by the problem of chip-bow, which results in poor uniformity of contrast ratio across the device. In order for the 256×256 pixel device to not exhibit unacceptable interference fringes across the active array, a chip flatness of 0.175μm is required. Once a uniform cell thickness can be produced, work can then be undertaken to improve the contrast ratio and switching speed by reducing the cell thickness and improving the liquid crystal alignment. For the 256 channel crossbar to have a signal-to-noise ratio of 1:1, a contrast ratio of 255:1 is required. The crossbar system architecture is susceptible to problems of pixel drop-out as every pixel on the device corresponds to a channel. This also affects the scalability of this system architecture. Finally, the problem of the low optical duty cycle of the pixels also needs to be addressed by first improving the bistability of the ferroelectric liquid crystal and then taking advantage of it by using an addressing scheme which provides D.C. balancing of the liquid crystal whilst retaining a high duty cycle.

Despite these problems it is believed that a fully working 256 channel system would be feasible, but probably not with fibre input channels which would require the orientation of the polarisation of the light leaving the fibres to be accurately specified. Use of an array of multi-mode output fibres would be possible, as they do not need to maintain the polarisation state of the light. However the system would probably have more applications with an emmitter/modulator array as the input, and a modulator/detector array at the output. Vertical-Surface-Cavity-Emitting-Lasers (VSCELs) may provide suitable emmitter arrays for the input, or alternatively FLC/Si SLMs as illustrated in this thesis. Photodiode arrays would provide a simple means of interrogating the output of the system and taking the information back into the electrical domain. However as the system is a large switching network, the use of FLC/Si SLMs at both the input and output would allow the system to be used as a unit inside a larger optical system.

It is doubtful whether or not a system based on FLC/Si SLMs would have applications in telecommunications, due to the high data rates and low latency imposed by the new Asynchronous Transfer Mode (ATM) data format, although specialist communication networks on say a aeroplane or a ship may be feasible. Systems such as optical neural networks, data processing (e.g. data encryption), and highly parallel optical computing provide more suitable application areas for very large (>100 channel) crossbar networks. Smaller crossbar networks with fibre input and output such as the OCPM project are more suited to specialist communications systems. An example of such an application is inter-board communications in large parallel computer systems, where the data rate is vey high, but the long packet lengths and routing latency may allow FLC devices to be used.

6.4 Dynamic Hologram Routing System

An optical system which routes a single input beam to an array of eight output fibres using the 256×256 SLM as a dynamic holographic optical element has been presented. The performance of this system has been assessed and the scalability of routing systems implemented in this manner discussed. It has been argued that the 256×256 SLM can route up to 32 channels in a non-blocking architecture with multi-cast and broadcast capability. Furthermore it has been shown that the maximum number of channels is directly proportional to the number of pixels on the SLM, and that reducing the pixel size can lead to a reduction in both the output spot size and the overall size of the optical system. The test system exhibited a very high signal-noise ratio in the output channels and it is expected that this could be further improved by using smaller diameter fibres. As the SLM is used in the Fourier plane of the system as a holographic element, pixel drop-out does not influence the performance of the system to any extent, a large number of unworking pixels would be required before any increase in the signal-noise ratio was noticed. The increased tolerance against pixel drop-out of the holographic routing system compared to the matrix-matrix crossbar switch is of course achieved by the increased redundancy present in the holographic system. The pattern on the 256×256 SLM is only valid for 50% of the time, with all the pixels being turned off during the other 50%. This is unsuitable for SLMs operating as phase elements. By altering the addressing scheme so that the inverse image was present for the second half of the frame (which is simple to implement electrically) the duty cycle would be significantly increased as the inverse image would have the same optical output. This is because the Fourier Transform of a $0 \rightarrow \pi \rightarrow 0$ relative phase transition has the same amplitude as a $\pi \rightarrow 0 \rightarrow \pi$ transition.

6.5 Comparison Of Routing Systems

In order to compare the performance of the two system architectures, the following factors must be considered:

1. Scalability.
2. Optical throughput.
3. Signal-noise ratio.
4. Ease of construction.
5. Device performance requirements e.g. contrast ratio, uniformity, pixel drop-out, and duty cycle.

In terms of the number of SLM pixels the scalability of the crossbar is much better than that of the dynamic holographic system. The 256×256 SLM can route 256 channels when used in a crossbar architecture, but only 32 channels when used as a dynamic holographic element. However in the case of the crossbar the SLM is not the only critical element and the 256 channel crossbar system is difficult to implement fully due to the strict focal length error tolerance requirements of the Fourier Transforming lenses.

The optical throughput of the crossbar system is extremely poor and worsens as the number of channels increases due to the intrinsic fanout loss. The throughput of the dynamic holographic system does not suffer from this limitation as all the light is theoretically routed to the output channel/s. In practice this is limited by the performance of the SLM. The optical throughput would be improved by using a liquid crystal with a 45° switching angle as previously discussed.

The signal-noise ratio of the crossbar system is very poor due to the architecture, residual light from all the OFF channels is also incident on each output fibre and so the signal-noise ratio is directly related to the contrast ratio of the SLM. As shown by the test system the signal-noise ratio of the dynamic hologram system is much

higher as no light is incident on an output channel unless it is being addressed (providing the holograms are well designed).

A dynamic hologram system appears to be a much simpler system to assemble. It consists of fewer components and the alignment tolerances are not as strict as the crossbar system which requires individual spots to be aligned onto the mirrors of the SLM. In order for both system architectures to operate reliably, they require that the SLM has a uniform contrast ratio across its area. Thus the problem of chip-bow needs to be solved. This is the greatest problem affecting the performance of the devices at present. Once this has been solved it may be possible to make further improvements in contrast ratio, optical throughput, and switching speed, by improved liquid crystal alignment and using thinner (1μm) cell thicknesses. For both systems it is important to achieve a much higher duty-cycle. It is simpler to achieve this for the phase modulating SLM as displaying the inverse pattern has the same effect as displaying the original pattern. However in both cases it is important for good bistability in the liquid crystal to be achieved. Finally the problem of pixel drop-out is of importance to the crossbar system as all the pixels correspond to a specific channel. This may only be overcome by having built-in redundancy in the backplane. However this affects the scalability of the system. This problem does not occur in the dynamic hologram system, which already has redundancy built into the holographic pattern.

It is concluded that for systems which do not require a very large number of channels (<100), the dynamic holographic implementation offers the best overall system performance in terms of optical throughput, signal-noise ratio, and manufacturability. However larger systems are impractical using this architecture and so the crossbar implementation must be used, despite its low optical throughput and poor manufacturability. In comparison to systems implemented using cascaded SEED/VCSEL arrays, the liquid crystal SLM based crossbar and dynamic routing system both offer greater scalability and better manufacturability, but cannot compete with the switching speed of these devices, and so rather than attempting to compete with these devices in the telecommunications industry, it may be better to exploit high parallelism of these systems in areas in which they better suited, such as optical data processing.

6.6 Concluding Remarks

During the 30 months it has taken to complete this work tremendous advances in the performance of FLC/Si SLMs have taken place. Although further work needs to be carried out, specifically solving the chip-bow problem, the devices are now of such quality that systems can be designed and constructed. If optics is to emerge as the dominant information transport medium of the future, it is important that these systems are demonstrated, and shown to solve some of the problems that electronics is encountering. It is hoped that the work presented here is a first step is showing that FLC/Si SLMs can be used in functional optical routing systems and that they will play a major role in future work.

6.7 Proposals For Further Work

The binary hologram fabrication technique only requires slight adjustment in order to fully optimise the process. Several papers have discussed how arrays of 1000s$\times$1000s of spots can be generated using binary phase elements. This technique offers a method of actually making an array of $\approx$ 1000$\times$1000 spots by cascading two 33$\times$33 binary elements.

In terms of optical systems work, a fully working 32 channel dynamic hologram routing system basesd on the 256$\times$256 SLM seems to be the logical step once flat devices can be fabricated. It would make sense to construct this using 850nm laser diodes as the sources and a custom interface to drive the SLM as fast as possible, with the different holographic patterns stored on the interface. It may also be possible to drive the SLM so that the inverse pattern is displayed, rather than a blank frame. The use of a FLC with a 45° switching angle would be an obvious way of improving the performance of the device.

We do not see the point in attempting to construct a full 256 channel crossbar, but it might be of interest to construct a smaller system, with an SLM as the input and the output routed back to a different area of the same device. This

optical feedback may have applications in neural network type systems. The four grey-level fanout hologram presented in this thesis could also be used to provide optical weights in a neural network based system.

A final suggestion would be to attempt to build some sort of multichannel correlator/image recognition system, using either dynamic or static holographic elements to route the input image to several different filters simultaneously or sequentially. This system could be of use when the input scene is compared with many different matched filters to identify a correlation.

Bibliography

[1] C. Mao, K. Johnson, R. Turner, D. Jared, and D. Doroski. Applications of binary and analogue hydrogenated amorphous silicon/ferroelectric liquid-crystal optically addressed spatial light modulators. *APPLIED OPTICS*, 31 No. 20:3908–3916, 1992.

[2] Kristina Johnson, D. J. McKnight, and I. Underwood. Smart spatial light modulators using liquid crystals on silicon. *IEEE JOURNAL OF QUANTUM ELECTRONICS*, 29 No. 2:699–714, 1993.

[3] M. Snook, P. McOwan, W. Hossack, and D. Vass. Smart liquid crystal light modulator for use in real-time image intensity contouring. In *OSA Annual General Meeting: Technical Digest*, 1993.

[4] Applied Optics special issue on Spatial Light Modulators, Volume 31, Number 20, 1992.

[5] Applied Optics special issue on Spatial Light Modulators, Volume 33, Number 14, 1994.

[6] J. C. Kirsch and D. A. Gregory. Video rate optical correlation using a magneto-optic spatial light modulator. *OPTICAL ENGINEERING*, 29 No. 9:1122–1128, 1990.

[7] W. E. Ross and D. N. Lambeth. Fabrication and switching sensitivity of the new magneto optic spatial light modulator. In *Spatial Light Modulators and Applications*, OSA 1993 Technical digest series, Vol. 6, 1993.

[8] B. Mansoorian, G. Marsden, V. Ozguz, C. Fan, and S. Esener. Characterisation of a free space optoelectronic interconnect system based on Si/PLZT smart pixels. In *Technical Digest: International conference on optical computing*, Heriot Watt University, Edinburgh, August 22-25th 1994.

[9] M. S. Jin, J. Wang, V. Ozguz, and S. Lee. Bonding of Si thin films to PLZT substrates for smart spatial light modulator applications. In *Spatial Light Modulators and Applications*, OSA 1993 Technical digest series, Vol. 6, 1993.

[10] Tsen-Hwang Lin, J. Wang, S. Dasgupta, S. Esener, and S. Lee. Two-dimensional spatial light modulators fabricated in Si/PLZT. *APPLIED OPTICS*, 29 No. 11:1595–1603, 1990.

[11] S. C. Esener, J. Wang, T. Drabnik, M. Title, and S. Lee. One-dimensional silicon/PLZT spatial light modulators. *OPTICAL ENGINEERING*, 26 No. 5:406–413, 1987.

[12] R. Lytel, G. F. Lipscomb, J. T. Kenney, and A. J. Ticknor. Applications of electro-optic polymers to optical interconnects. *SPIE OPTICAL ENHANCEMENTS TO COMPUTING TECHNOLOGY*, 1563:122–138, 1991.

[13] I. C. Khoo and Y. R. Shen. Liquid crystals: nonlinear optical properties and processes. *OPTICAL ENGINEERING*, 24 No. 4:579–585, 1985.

[14] D. R. Pape and L. J. Hornbeck. Characteristics of the deformable mirror device for optical information processing. *OPTICAL ENGINEERING*, 22 No. 6:675–681, 1983.

[15] L. J. Hornbeck. Deformable mirror spatial light modulators. *SPIE CRITICAL REVIEW SERIES*, 1150:86–102, 1990.

[16] R. Wilson. Mirror, mirror, on the wall. *ElECTRONICS WEEKLY*, November:p16, 1993.

[17] R. W. Cohn. Link analysis of a deformable mirror device based optical crossbar switch. *OPTICAL ENGINEERING*, 31 No. 1:134–140, 1992.

[18] M. A. Mignardi. Digital micromirror array for projection TV. *SOLID STATE TECHNOLOGY*, 37 No. 7:63–68, 1994.

[19] D. R. Collins, J. Sampsell, L. Hornbeck, J. Florence, P. Penz, and M. Gately. Deformable mirror device spatial light modulators and their applicability to optical neural networks. *APPLIED OPTICS*, 28 No. 22:4900–4907, 1989.

[20] R. M. Boysel. A 128 x 128 frame addressed deformable mirror spatial light modulator. *OPTICAL ENGINEERING*, 30 No. 9:1422–1427, 1991.

[21] Uzi Efron, editor. *Spatial light modulator technology materials, devices, and applications.* Marcel Dekker Inc., 1992.

[22] A. L. Lentine, F. B. McCormick, R. A. Novotny, L. Chirovsky, L. D'Asaro, R. Kopf, J. Kuo, and G. Boyd. A 2kbit array of symmetric self-electrooptic effect devices. *IEEE PHOTONICS TECHNOLOGY LETTERS*, 2 No. 1:51–53, 1990.

[23] F. B. McCormick, T. Cloonan, A. Lentine, J. Sasian, R. Morrison, M. Beckman, S. Walker, M. Wojcik, S. Hinterlong, R. Crisci, R. Novotny, and H. Hinton. Five-stage free-space optical switching network with field-effect transistor self-electro-optic-effect-device smart-pixel arrays. *APPLIED OPTICS*, 33 No. 8:1601–1618, 1994.

[24] F. B. McCormick, F. Tooley, T. Cloonan, J. Brubaker, A. Lentine, R. Morrison, S. Hinterlong, M. Herron, S. Walker, and J. Sasian. Experimental investigation of a free-space optical switching network by using symmetric self-electro-optic-effect devices. *APPLIED OPTICS*, 31 No. 26:5431–5446, 1992.

[25] F. B. McCormick, A. Lentine, R. Morrison, J. Sasian, T. Cloonan, R. Novotny, M. Beckman, M. Wojcik, S. Hinterlong, and D. Buchholz. 155 Mb/s operation or a FET-SEED free-space switching network. *IEEE PHOTONICS TECHNOLOGY LETTERS*, 6 No. 12:1479–1481, 1994.

[26] K. Goossen, A. Lentine, J. Walker, L. D'Asaro, S. Hui, B. Tseng, R. Leibenguth, D. Kossives, D. Dahringer, L. Chirovsky, and D. Miller. Demonstration of a dense high-speed optoelectronic technology integrated with silicon CMOS via flip-chip bonding and substrate removal. In *OSA Technical Digest Series Volume 10*, 1995.

[27] R. A. Novotny, A. L. Lentine, D. Buchholz, and A. Krishnamoorthy. Analysis of parasitic front-end capacitance and thermal resistancein hybrid flip-chip-bonded GaAs SEED/Si CMOS receivers. In *OSA Technical Digest Series Volume 10*, 1995.

[28] T. L. Worchesky and K. J. Ritter. Large arrays of spatial light modulators hybridized to silicon integrated circuits. In *OSA Technical Digest Series Volume 9*, 1995.

[29] M. G. Clark, K. J. Harrison, and E. P. Raynes. Liquid crystal materials and devices. *PHYSICS TECHNOLOGY*, 11:232–240, 1980.

[30] R. S. McEwen. Liquid crystals, displays and devices for optical processing. *J. PHYS. E. SCI. INSTRUM*, 20:364–377, 1987.

[31] H. Yamazaki and M. Yamaguchi. 4 x 4 Free-space optical switching using real-time binary phase-only holograms generated by a liquid-crystal display. *OPTICS LETTERS*, 16 No. 18:1415–1417, 1991.

[32] R. B. Meyer, L. Liebert, L. Strzelecki, and P. Keller. Ferroelectric liquid crystals. *LE JOURNAL DE PHYSIQUE-LETTRES*, 36:69–71, 1975.

[33] Yu. P. Panarin, E. Pozhidaev, and M. Barnik. Bistability in ferroelectric liquid crystals. *MOL. MAT.*, 1:29–42, 1992.

[34] A. Mochizuki, K. Motoyushi, and M. Nakatsuka. A high contrast and high transmittance multiplexing SSFLC display utilising naphthalenebase liquid crystal materials. *FERROELECTRICS*, 122:37–51, 1991.

[35] J. M. Oton, J. Pena, A. Serrano, and F. Olarte. Optical studies of smectic C* displays. *FERROELECTRICS*, 122:293–309, 1991.

[36] M. Ozaki, H. Moritake, A. Tagawa, N. Shigeno, and K. Yoshino. Optical bistable and limiting behaviours in ferroelectric liquid crystal and optical processing. *FERROELECTRICS*, 122:113–125, 1991.

[37] W. Hartmann. Ferroelectric liquid crystal displays for television applications. *FERROELECTRICS*, 122:1–26, 1991.

[38] S. Heeks, A. Mosley, B. Nicholas, P. Rundle, and P. Schlusche. Large area ferroelectric liquid crystal displays. *FERROELECTRICS*, 122:27–35, 1991.

[39] N. A. Clark and S. T. Lagerwall. Submicrosecond bistable electro-optic switching in liquid crystals. *APPLIED PHYSICS LETTERS*, 36 No. 11:899–901, 1980.

[40] S. Kaho, T. Masumi, S. Tahata, M. Mizunuma, and S. Miyake. Alignment and electro-optic porperties of SSFLC cells aligned by obliquely evaporated SiO films. *MOL. CRYST. LIQ. CRYST.*, 199:87–95, 1991.

[41] D. Doroski, S. Perlmutter, and G. Moddel. Alignment layers for improved surface-stabilised ferroelectric liquid crystal devices. *APPLIED OPTICS*, 33 No. 13:2608–2610, 1994.

[42] Alastair R. MacGregor. Method for computing the optical properties of a smectic C* liquid crystal cell. *J. OPT. SOC. AM. A*, 6 No. 9:1493–1503, 1989.

[43] K. Skarp and M. A. Handschy. Ferroelectric liquid crystals. Material properties and applications. *MOL. CRYST. LIQ. CRYST.*, 165:439–509, 1988.

[44] K. Flatischler, K. Skarp, S. Lagerwall, and B. Stebler. Thin ferroelectric liquid crystal cells with surface induced alignment: Optical characterisation and electro-optic performance. *MOL. CRYST LIQ. CRYST.*, 131:21–46, 1985.

[45] R. Shao, Z. Zhuang, and N. Clark. Director structures of a chiral smectic I liquid crystal in the planarised geometry. *FERROELECTRICS*, 122:213–220, 1991.

[46] Xue Jiu-Zhi, M. Handschy, and N. Clark. Electrooptical switching properties of uniform layer tilted surface stabilized ferroelectric liquid crystal devices. *LIQUID CRYSTALS*, 2 No. 5:707–716, 1987.

[47] M. Glogarova, J. Fousek, L. Lejcek, and J. Pavel. The structure of ferroelectric liquid crystals in planar geometry and its response to electric fields. *FERROELECTRICS*, 58:161–178, 1984.

[48] V. Dmitrienko and V. Belyakov. Structure of chiral smectics in an electric field. *SOV. PHYS. JETP*, 51 No. 4:787–792, 1980.

[49] J. S. Patel. Electro-optics of ferroelectric liquid crystals. *OPTICAL ENGINEERING*, 26 No.2:129–133, 1987.

[50] J. W. Goodby and J. S. Patel. Properties of ferroelectric liquid crystals. In *SPIE Vol.684 Liquid crystals and spatial light modulators materials*, 1986.

[51] T. Kurokawa and S. Fukushima. Spatial light modulators using ferroelectric liquid crystals. *OPTICAL AND QUANTUM ELECTRONICS*, 24:1151–1163, 1992.

[52] R. M. Turner, D. Jared, G. Sharp, and K. Johnson. Optical correlator using very-large-scale-integrated circuit/ferroelctric-liquid-crystal spatial light modulators. *APPLIED OPTICS*, 32 No. 17:3094–3101, 1993.

[53] James Gourlay. *Ferroelectric liquid crystal spatial light modulators: Devices and applications*. PhD thesis, University of Edinburgh, 1994.

[54] I. Underwood, D. G. Vass, and R. Sillitto. Evaluation of an nMOS VLSI array for an adaptive liquid-crystal spatial light modulator. In *IEE Proceedings Vol. 133, Pt.J, No. 1*, 1986.

[55] I. Underwood, R. Sillitto, and D. G. Vass. An nMOS addressed liquid crystal spatial light modulator. In *IEE Colloquium on optical techniques in image and signal processing*, 1985.

[56] D. J. McKnight, K. Johnson, and R. Serati. 256 x 256 liquid-crystal-on-silicon spatial light modulator. *APPLIED OPTICS*, 33 No. 14:2775–2784, 1994.

[57] H. J. White, G. Proudley, C. Stace, N. Brownjohn, A. Walker, M. Taghizadeh, B. Robertson, C. Barrett, W. Crossland, J. Brocklehurst, M. Birch, M. Snook, and D. Vass. Performance of an optical free-space crossbar. In *Technical Digest: International conference on optical computing*, Heriot Watt University, Edinburgh, August 22-25th 1994.

[58] I. Underwood, D. G. Vass, R. Sillitto, G. Bradford, N. Fancey, and A. Al-Chalabi. A high performance spatial light modulator. *SPIE DEVICES FOR OPTICAL PROCESSING*, 1562:107–115, 1991.

[59] I. Underwood, D. G. Vass, D. C. Burns, P. McOwan, and J. Gourlay. Improving the performance of liquid crystal over silicon spatial light modulators: Issues and achievements. *APPLIED OPTICS*, 33 No. 14:2768–2774, 1994.

[60] A. O'Hara, J. Gourlay, D. G. Vass, I. Underwood, d. C. Burns, and J. Stevenson. Post-processing of spatial light modulator backplanes to improve their optical performance. *To be submitted to Optical Engineering*, 1995.

[61] A. O'Hara, J. R. Hannah, I. Underwood, D. G. Vass, and R. J. Holwill. Mirror quality and efficiency improvements of reflective spatial light modulators by the use of dielectric coatings and chemical-mechanical polishing. *APPLIED OPTICS*, 32 No. 28:5549–5555, 1993.

[62] Scottish Collaborative Initiative On Optical Sciences (SCIOS), a collaborative project between Heriot Watt University, St. Andrews University, Edinburgh University, and Glasgow University, 1995. Contact Professor A Walker, Heriot Watt University, Department Of Physics, Edinburgh, Scotland.

[63] Dwayne Burns. *Design and characterisation of a ferroelectric liquid crystal over silicon spatial light modulator.* PhD thesis, University of Edinburgh, 1994.

[64] D. C. Burns, I. Underwood, D. G. Vass, and A. Murray. An optoelectronic neural network with temporally multiplexed grey-scale weights. In *Proceedings of the fourth international conference on microelectronics for neural networks and fuzzy systems*, 1994.

[65] D. C. Burns, I. Underwood, D. G. Vass, and A. O'Hara. Electronically addressed ferroelectric liquid crystal over silicon spatial light modulators for optical computing. In *Technical Digest: International conference on optical computing*, Heriot Watt University, Edinburgh, August 22-25th 1994.

[66] D. C. Burns. BHOY-A 256x256 static-RAM ferroelectric liquid crystal spatial light modulator. *Group Report (Private Communication)*, 1993.

[67] T. Beynon, I. Kirk, and T. Matthews. Gabor zone plate with binary transmittance values. *OPTICS LETTERS*, 17 No. 7:544–546, 1992.

[68] Chang-Yuan Han, Yukihiro Ishii, and Kazumi Murata. Reshaping collimated laser beams with gaussian profile to uniform profiles. *APPLIED OPTICS*, 22 No. 22:3644–3647, 1983.

[69] H. Dammann and K. Gortler. High-efficiency in-line multiple imaging by means of multiple phase holograms. *OPTICS COMMUNICATIONS*, 3:312–315, 1971.

[70] H. Dammann and E. Klotz. Coherent optical generation and inspection of two-dimensional periodic structures. *OPTICA ACTA*, 24:505–515, 1977.

[71] M. Dames, R. Dowling, P. McKee, and D. Wood. Efficient optical elements to generate intensity weighted spot arrays: design and fabrication. *APPLIED OPTICS*, 30 No. 19:2685–2691, 1991.

[72] J. Jahns, M. Downs, M. Prise, N. Streibl, and S. Walker. Dammann gratings for laser beam shaping. *OPTICAL ENGINEERING*, 28 No.12:1267–1275, 1989.

[73] A. Stevens, W. Hossack, and S. Samus. Very-large-scale-integration fabrication technique for binary-phase gratings on sapphire. *APPLIED OPTICS*, 34 No. 1:190–193, 1995.

[74] Sergei Samus. *Computer design and optimisation of holographic phase elements.* PhD thesis, University of Edinburgh, 1995.

[75] R. D. Guenther. *Modern Optics.* John Wiley Sons, 1990.

[76] E. Hecht. *Optics.* Addison-Wesley, second edition, 1989.

[77] H. Lupken, T. Pauka, R. Brauer, F. Wyrowski, and O. Bryngdahl. On the design of dammann gratings. *OPTICS COMMUNICATIONS*, 100 No. 5,6:415–420, 1993.

[78] W. J. Hossack. Modern Optics Lecture Notes, 1995, University Of Edinburgh.

[79] U. Krackhardt, J. Mait, and N. Streibl. Upper bound on the diffraction efficiency of phase-only fanout elements. *APPLIED OPTICS*, 31 No. 1:27–37, 1992.

[80] M. Ekberg, M. Larsson, S. Hard, J. Turunen, M. Taghizadeh, J. Westerholm, and A. Vasara. Multilevel grating array illuminators manufactured by electron-beam lithography. *OPTICS COMMUNICATIONS*, 88 No. 1:37–41, 1992.

[81] S. Walker and J. Jahns. Array generation with multilevel phase gratings. *J. Opt. Soc. Am. A*, 7 No. 8:1509–1513, 1990.

[82] C. W. Stirk. Cost models of components for free-space optically-interconnected systems. *SPIE PHOTONIC NEURAL NETWORKS*, 1773:231–241, 1992.

[83] A. Vasara, M. Taghizadeh, J. Turunen, J. Westerholm, E. Noponen, H. Ichikawa, J. Miller, T. Jaakkola, and S. Kuisma. Binary surface-relief gratings for array illumination in digital optics. *APPLIED OPTICS*, 31 No. 17:3320–3336, 1992.

[84] D. Pommet, M. Moharam, and E. Grann. Effects of fabrication errors on the performance of binary gratings. In *Diffractive Optics: Design, Fabrication, and Applications*, OSA 1994 Technical digest series, Vol. 11, 1994.

[85] R. L. Morrison and S. L. Walker. Design issues for beam array generation gratings. In *Technical Digest: International conference on optical computing*, Heriot Watt University, Edinburgh, August 22-25th 1994.

[86] M. Taghizadeh, J. Wilson, J. Turunen, A. Vasara, and J. Westerholm. Optimisation and fabrication of grating beamsplitters in silicon nitride. *APPLIED PHYSICS LETTERS*, 54 No. 16:1492–1494, 1989.

[87] M. Heibmeier, U. Krackhardt, and N. Streibl. A dammann grating with diffraction orders of arbitrary intensity etched into aluminium oxide. *OPTICS COMMUNICATIONS*, 76 No. 2:103–106, 1990.

[88] H. Ichikawa, M. Taghizadeh, and J. Turunen. Noninterferometric fabrication of computer-generated phase holograms on silver halide photographic emulsion. *OPTICAL ENGINEERING*, 30 No. 12:1869–1877, 1991.

[89] S. Shank, M. Skvarla, F. Chen, and H. Craighead. Fabrication of multi-level phase gratings using focused ion beam milling and electron beam lithography. In *Diffractive Optics: Design, Fabrication, and Applications*, OSA 1994 Technical digest series, Vol. 11, 1994.

[90] M. J. Verheijen. E-beam lithography for digital holograms. *JOURNAL OF MODERN OPTICS*, 40 No. 4:711–721, 1993.

[91] B. Robertson and M. Taghizadeh. High-efficiency, wide-bandwidth optical fanout elements in dichromated gelatin. *OPTICS LETTERS*, 15 No. 12:694–696, 1990.

[92] N. Phillips, A. Ward, R. Cullen, and D. Porter. Advances in holographic bleaches. *PHOTOGRAPHIC SCIENCE AND ENGINEERING*, 24 No. 2:120–124, 1980.

[93] A private communication with Alan Gundlach,
Department of Electrical Engineering,
University of Edinburgh 1993.

[94] S. M. Sze. *VLSI Technology*. McGraw-Hill, 1983.

[95] Compugraphics International Ltd. Eastfield Industrial Estate, Glenrothes, Fife, KY7 4NT. Tele : 01592 772557 Fax : 01592775359.

[96] F. B. McCormick. Generation of large spot arrays from a single laser beam by multiple imaging with binary phase gratings. *OPTICAL ENGINEERING*, 28 No. 4:299–304, 1989.

[97] S. Hinton and D. Millar. Free-space photonics in switching. *AT&T TECHNICAL JOURNAL*, Jan.:85–91, 1992.

[98] S. Araki, M. Kajita, K. Kasahara, K. Kubota, K. Kurihara, I. Redmond, E. Schenfeld, and T.Suzaki. Massive optical interconnections (MOI): Interconnections for massively parallel processing systems. In *OSA Technical Digest Series Volume 10*, 1995.

[99] M. Fukui and K. Kitayama. High-throughput optical image crossbar switch that uses a point light source array. *OPTICS LETTERS*, 18 No. 5:376–378, 1993.

[100] T. Cloonan, G. Richards, A. Lentine, F. McCormick, and J. Erickson. Free-space photonic switching archtectures based on extended generalised shuffle networks. *APPLIED OPTICS*, 31 No. 35:7471–7492, 1992.

[101] D. V. Plant, B. Robertson, H. S. Hinton, W. Robertson, G. Boisset, N. Kim, Y. Liu, M. Otazo, D. Rolston, and A. Shang. 16 channel FET-SEED based optical backplane interconnection. In *OSA Technical Digest Series Volume 10*, 1995.

[102] D. V. Plant, B. Robertson, H. S. Hinton, W. Robertson, G. Boisset, N. Kim, Y. Liu, M. Otazo, A. Shang, and L. Sun. A FET-SEED based optical backplane demonstrator. In *Technical Digest: International conference on optical computing*, Heriot Watt University, Edinburgh, August 22-25th 1994.

[103] T. H. Szymanski. Intelligent optical backplanes. In *OSA Technical Digest Series Volume 10*, 1995.

[104] I. Redmond and E. Schenfeld. Experimental results of a 64 channel, free-space optical interconnection network for massively parallel processing. In *Technical Digest: International conference on optical computing*, Heriot Watt University, Edinburgh, August 22-25th 1994.

[105] B. Clymer and S. A. Collins. Optical computer switching network. *OPTICAL ENGINEERING*, 24 No. 1:74–81, 1985.

[106] Demetri Psaltis. Two-dimensional optical processing using one-dimensional input devices. *PROCEEDINGS OF THE IEEE*, 72 No. 7:962–974, 1984.

[107] A. A. Sawchuck, B. K. Jenkins, C. S. Raghavendra, and A. Varma. Optical crossbar networks. *COMPUTER*, pages 50–60, 1987.

[108] A. G. Kirk, W. A. Crossland, and T. J. Hall. A compact and scalable free-space optical crossbar. *SPIE PROCEEDINGS*, 1574:137–141, 1991.

[109] G. Proudly, C. Stace, and H. White. Fabrication of two-dimensional fiber optic arrays for an optical crossbar switch. *OPTICAL ENGINEERING*, 33 No. 2:627–635, 1994.

[110] D. Daly, R. Stevens, M. Hutley, and N. Davies. The manufacture of microlenses by melting photoresist. *MEAS. SCI. TECHNOLOGY*, 1:759–766, 1990.

[111] P. Blair, M. Taghizadeh, J. Turunen, and B. Robertson. Output array fan-in for a matrix-matrix crossbar using diffractive micro-lenses. In *Topical meetings technical digest series: Volume 2 Microlens Arrays*, National physical laboratory, 13-14 May 1993.

[112] W. J. Smith. *Modern optical engineering.* McGraw Hill, second edition, 1990.

[113] Spindler and Hoyer Ltd. 2 Drakes Mews, Crownhill, Milton Keynes, Bucks. Tele : 01908 262525 Fax : 01908 262526.

[114] A private communication Steven Dibner, Melles Griot Ltd.
Brookmount Court,
Kirkwood Road,
Cambridge. Tele : 01223 420071 Fax : 01223 425310.

[115] J. N. Mait and G. S. Himes. Computer generated holograms by means of a magneto-optic spatial light modulator. *APPLIED OPTICS*, 28 No. 22:4879–4887, 1989.

[116] D. M. Cottrell, J. Davis, T. Hedman, and R. Lilly. Multiple imaging phase-encoded optical elements written as programmable spatial light modulators. *APPLIED OPTICS*, 29 No. 17:2505–2509, 1990.

[117] T. Ishida and M. Ishikawa. Reconfigurable space-variant optical interconnection using binary CGH. In *OSA Technical Digest Series Volume 10*, 1995.

[118] D. C. O'Brien, W. A. Crossland, and R. J. Mears. A holographically routed crossbar: Theory and simulation. *OPTICAL COMPUTING AND PROCESSING*, 1 No. 3:233–243, 1991.

[119] D. C. O'Brien, T. Wilkinson, R. Mears, and W. Crossland. Generalised dynamic holographic interconnects using spatial light modulators. In *SLM's and Applications: OSA Technical Digest Series Volume 6:*, Palm Springs, March 15-17th 1993.

[120] D. C. O'Brien, R. Mears, T. Wilkinson, and W. A. Crossland. Dynamic holographic interconnects that use ferroelectric liquid-crystal spatial light modulators. *APPLIED OPTICS*, 33 No. 14:2795–2803, 1994.

[121] D. C. O'Brien and G. Moddell. Ferroelectric liquid-crystal optically addressed spatial light modulators for binary phase gratings. In *OSA Technical Digest: Spatial Light Modulators And Applications*, Salt Lake City, Utah, March 14-16th 1995.

[122] T. Wilkinson, D. C. O'Brien, and R. Mears. Dynamic asymmetric binary holograms using a ferroelectric liquid crystal spatial light modulator. *OPTICS COMMUNICATIONS*, 109:222–226, 1994.

[123] S. E. Broomfield, M. Neil, E. Paige, and G. Yang. Programmable binary phase-only optical device based on a ferroelectric liquid crystal SLM. *ELECTRONICS LETTERS*, 28 No. 1:26–28, 1992.

[124] J. Gourlay, S. Heddle, A. O'Hara, S. Samus, and D. G. Vass. Optical interconnect using pixellated spatial light modulators. In *Technical Digest: International conference on optical computing*, Heriot Watt University, Edinburgh, August 22-25th 1994.

[125] J. Gourlay, A. O'Hara, A. J. Stevens, and D. G. Vass. A comparative investigation into a planarised liquid crystal over silicon spatial light modulators, 1995. Accepted for publication in JOURNAL OF MODERN OPTICS.

[126] A. J. Stevens, J. Gourlay, S. Samus, W. J. Hossack, D. G. Vass, and D. C. Burns. Experimental investigation of free space optical interconnects. In *OSA Technical Digest: Spatial Light Modulators And Applications*, Salt Lake City, Utah, March 14-16th 1995.

[127] W. J. Hossack, D. G. Vass, and I. Underwood. Fourier processing with binary spatial light modulators. In *SPIE Volume 1564: Optical Information Processing Systems and Architectures III*, San Diego, California, July 23-26th 1991.

Appendix A

Applied Optics Paper

Very-Large-Scale-Integration Fabrication Technique
For Binary Phase Gratings On Sapphire.

A. J. Stevens, W. Hossack, S. Samus.

APPLIED OPTICS Vol. 34 No. 1 pp 190-193.

a reprint from Applied Optics

Very-large-scale-integration fabrication technique for binary-phase gratings on sapphire

Andrew J. Stevens, William J. Hossack, and Sergei Samus

An efficient, high-yield process for the production of binary-phase holograms is presented by controlled deposition of silicon nitride over a sapphire substrate with the binary structure formed by plasma etch of the silicon nitride. Optical results are presented for a 16 × 16 transmission fanout element that shows near-optimal performance.

Key words: Phase-only gratings, binary diffractive optics, computer-generated-hologram fabrication, array generators.

Introduction

Binary diffractive optics are important holographic elements in monochromatic optical systems. They are utilized in a range of applications that includes focusing,[1] beam shaping, and fanout.[2] These elements have a high optical efficiency, are easily designed, and are relatively easy to fabricate, and because they operate on axis they are easily incorporated into optical systems. A range of techniques has been used to fabricate binary optics, including controlled exposure and bleaching of photographic materials,[3] lithographic or electron-beam exposure of photoresist,[4] controlled deposition of SiO_2,[5] and controlled etching into solid material. The most successful technique to date appears to be the controlled plasma etching of fused silica.[6,7] This etching technique requires careful calibration of the etch rate, and uniformity across large substrates is difficult. In addition the etched regions tend to be rough, which contributes to light scattering. We present an alternative fabrication technique for binary diffractive optics based on accurately controlled deposition of silicon nitride on a sapphire substrate that is subsequently patterned and etched with the sapphire as an etch stop. This process results in optically smooth transmissive phase gratings with a phase thickness with a maximum variation of 1.5% across a wafer 75 mm in diameter. Results are presented for a 16 × 16 fanout element with an optical transmission of 91.6% and diffraction efficiency of 62.5% compared with a theoretical design efficiency of 64%. All processing operations in this fabrication technique are standard in very-large-scale integrated (VLSI) fabrication, and all patterning and etching were performed with unmodified fabrication facilities normally used for standard 3-μm CMOS (complementary metal-oxide semiconductor) processing.

Materials and Fabrication

Sapphire has optical properties that make it a good substrate for binary holograms; in particular it has a low scatter and absorption in the visible spectrum, is very hard and rigid, can be polished optically flat, and has a low-thermal-expansion coefficient. Its physical properties of a high melting point, zero porosity, and extreme resistance to both wet and plasma etches make it an ideal material for processing. Note, however, that sapphire is a birefringent material with refractive indices of 1.760 and 1.769; so if it is used with polarized illumination, the axis of polarization must be aligned with either the ordinary or extraordinary optical axis. Silicon nitride can be accurately deposited by low-pressure chemical vapor deposition.[8] Typical parameters for deposition are 800 °C with an atmosphere of NH_3 [90 cubic centimeters per minute at standard temperature (SCCM)] and $SiCl_2H_2$ (20 SCCM). Note that the need for high-temperature deposition prevents the use of prepatterned liftoff techniques.[5] With these flow rates the deposited silicon nitride film was measured at 39 Å/min with an index of 2.00. These films were found to be extremely rugged and optically flat, because they do not contain significant quantities of hydrogen that increase porosity. The sapphire substrates, which

The authors are with the Department of Physics, the University of Edinburgh, King's Buildings, Edinburgh, EH9 6JZ, Scotland, UK.

Received 23 November 1993; revised manuscript received 6 July 1994.
0003-6935/95/010190-04$06.00/0.

were in the form of 75-mm-diameter wafers, with a surface flatness of 1/60th of an optical wavelength over a 1-cm^2 region of the wafer, were found to be completely unaffected by this deposition. In addition it was found that the silicon nitride deposition rate was identical to the deposition rate onto bare silicon, which permitted silicon wafers to be used to monitor the film thickness. This permitted standard ellipsometry film thickness monitoring to be used that relies on the film being deposited on an optically reflective substrate.

The deposition technique results in a film of the same thickness being deposited on both sides of the wafers. This film can be easily etched off the unused side.

Diffractive Fanout Elements

The diffractive element chosen for fabrication was a 16 × 16 fanout grating of Dammann and Gortler.[9] The properties of these elements are well known; in particular any errors in phase depth show up as an undiffracted central spot, and these designs are critically dependent on an accurate phase-edge location to obtain good uniformity and diffraction efficiency.[10] The grating design was formed by simulated annealing,[11] and the theoretical diffraction efficiency as calculated for the one-dimensional grating was 79.5% compared with an ideal maximum of 81.1%.[12] The theoretical efficiency of the two-dimensional grating is thus 63.2%, which is typical for such elements. The transition points of a unit cell are in Table 1. The calculated grating transition was used to form a 32 × 32 replicated pattern with Cadence Edge VLSI tools and an industry standard ×10 chromium-on-glass mask with a geometric accuracy of ~0.25 μm. The grating was designed to operate in He–Ne illumination, so a silicon nitride film of 3164 Å is necessary to produce the required phase shift on transmission. This film was produced by two depositions of 30 min and one of 20 min, 8 s. The film thickness was monitored after each deposition by ellipsometry and an interferometric thin-film measure of silicon wafers placed adjacent to the sapphire substrate. With this technique it was possible to produce films that were on average within 1% of the required thickness and with a maximum variation of 1.5% across the 75-mm wafer.

Table 1. Binary-Phase Transition Point for a Unit Cell of a 16 × 16 Fanout Element with a Diffraction Efficiency of 79.5% in One Dimension

$0 \rightarrow \pi$ Transition	$\pi \rightarrow 0$ Transition
0.000000	0.039035
0.138932	0.170173
0.224478	0.245961
0.301181	0.361458
0.474307	0.503317
0.538810	0.638775
0.670051	0.720332
0.740412	0.802904
0.858767	0.974260

The wafer was then coated with photoresist and patterned with an Optimetrix ×10 wafer stepper that gave 32 patterned dies of 8 × 8 mm on each sapphire wafer, which gave a unit cell size of 0.25 mm. The wafer was then etched in a Plasma-Therm dry etcher with a hydrogen and CF_4 plasma for 16 min, which etched all the exposed silicon nitride back to the sapphire substrate. Owing to the physical properties of the sapphire, the etching uniformity is not critical, because the sapphire operates as an impervious etch stop. Using this process, we can determine the phase thickness of the holograms by the original wafer scale deposition and not the final etch conditions. The accuracy of 1% that is obtained is comparable with what can be obtained by controlled etching over small areas. Finally the back of the wafer was etched clear of silicon nitride by the above processes, and the back of the wafer was coated with an antireflection coating of MgF for the He–Ne wavelength.

Optical Results

The optical transmission of the wafer was measured at 91.6%. The diffraction pattern from a typical dye is shown in Fig. 1. It was constructed with a 300-mm lens that gave a spot array with a separation of 1.5 mm. The measured spot intensity uniformity is 1.8%, compared with a theoretical uniformity of 0.44%, and the diffraction efficiency is 62.5%, compared with a theoretical efficiency of 63.5%. The undiffracted spot is ~1.5 times that of the diffracted elements. This result is consistent with an error of ~1% in the phase depth.[13] Over the entire wafer of 32 gratings the diffraction efficiency varied by ~1%, and the largest undiffracted central spot was twice that of the diffracted spots, showing a slight lack of uniformity in film thickness across the wafer. All the gratings produced optical fanout elements, putting at least 56% of the total incident laser power into the required 16 × 16 array with an intensity unifor-

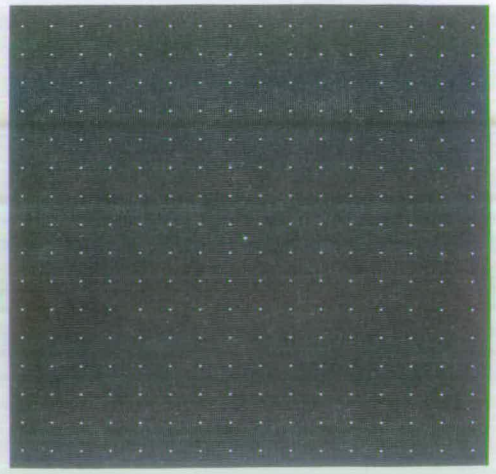

Fig. 1. Optical diffraction pattern from a Dammann grating.

mity of better than 2%, which compares favorably with other fabrication techniques.

Microscopic Examination of the Grating Structure

One of the gratings was coated with 100 Å of gold and examined under scanning electron microscopy. Figure 2 shows a 20° image of a 70 μm × 70 μm region of the grating. It shows that both the silicon nitride surface and the sapphire surface are smooth and there is no granularity or etch attack. The edge profile is shown in Fig. 3. This profile shows that the silicon nitride has been etched with near vertical edges with little rounding of the top edge and no undercut. The total edge spread is ~50 nm. Again both the silicon nitride and the sapphire show no evidence of etch attack and retain their smooth surfaces.

Extension to Multiphase

Unlike the deposition of SiO_2 at low temperature, which can be prepatterned,[5] the silicon nitride is deposited at a temperature at 800 °C, well above the temperature at which photoresists can operate. Consequently conventional multiphase processing cannot be applied.

We can, however, extend the technique to four phase levels by using the fact that the same thickness of silicon nitride is deposited on both sides of the wafer, which requires an asymmetric deposition with a depth of π on one side and $\pi/2$ on the other. Then by patterning and etching both sides, we can obtain four phase levels. The asymmetric deposition can be obtained by an initial deposition of $\pi/2$ on both sides. One side is then etched back to the sapphire to give a single-sided deposition of $\pi/2$. A second deposition is then performed to lay down a second $\pi/2$ layer, giving the required asymmetric deposition. The resulting four-level hologram would permit asymmetric diffraction patterns but may be limited in space bandwidth because of the diffraction effects between the two faces of the wafer.

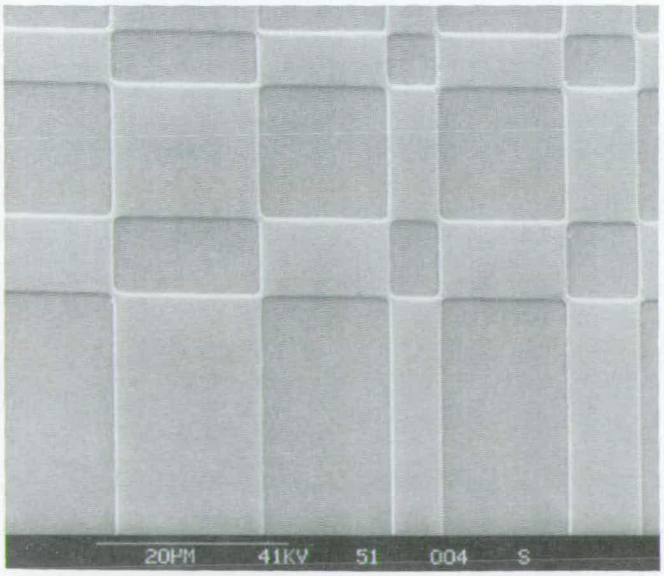

Fig. 2. Scanning electron micrograph of a coated grating structure.

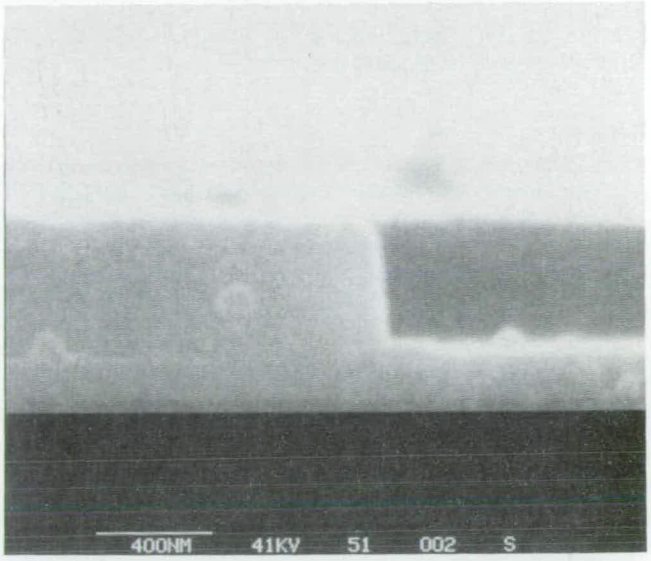

Fig. 3. Scanning electron micrograph showing the edge structure of a grating.

Conclusion

This fabrication technique permits accurate and reproducible production of binary transmission optics with a high yield and excellent uniformity. All processes used are standard in the VLSI production industry and do not require modification of any equipment available in a facility capable of high-resolution CMOS fabrication; in particular the fact that the deposition rates can be monitored on silicon wafers adjacent to the sapphire wafers permits ellipsometry to be used. Because of the birefringence of the substrate, care must be taken when these elements are used in polarized illumination. This restriction can be removed by coating the relief structure in aluminum or silver to form a reflective grating.

This fabrication technique is directly applicable to the fabrication of two-dimensional binary phase structures.[14] These design techniques permit arbitrary symmetric fanouts with diffraction efficiencies as high as 81%. The fabrication of a range of such two-dimensional gratings is currently being undertaken.

The authors thank the staff of the Edinburgh Microfabrication Facility, The University of Edinburgh, for advice and use of equipment. The scanning-electron-microscopy images were prepared by the Faculty Electronmicroscope Unit, The University of Edinburgh. Two authors (A. Stevens and S. Samus) are supported by Science and Engineering Research Council (SERC) studentships, and the research was partially supported under the SERC-

funded SCIOS (Scottish Collaborative Initiative on Optoelectronic Sciences) project.

References

1. T. D. Beynon, I. Kirk, and T. R. Mathews, "Gabor phase plate with binary transmittance values," Opt. Lett. **17,** 544–546 (1992).
2. R. L. Morrison, S. L. Walker, and T. J. Cloonan, "Beam array generation and holographic interconnections in a free-space optical switching network," Appl. Opt. **32,** 2512–2518 (1993).
3. H. Ichikawa, M. R. Taghizadeh, and J. Turunen, "Noninterferometric fabrication of computer-generated phase holograms on silver halide photographic emulsion," Opt. Eng. **30,** 1869–1877 (1991).
4. M. J. Verheijen, "E-beam lithography for digital hologams," J. Mod. Opt. **40,** 711–721 (1993).
5. J. Jahns and S. J. Walker, "Two-dimensional array of a diffractive microlens fabricated by thin-film deposition," Appl. Opt. **29,** 931–936 (1990).
6. J. Jahns, M. M. Downs, M. E. Prise, N. Streibl, and S. J. Walker, "Dammann gratings for laser beam shaping," Opt. Eng. **28,** 1267–1275 (1989).
7. J. M. Millar, M. R. Taghizadeh, N. Ross, E. Noponen, and A. Vasara, "Kinoform array illuminators in fused silica," J. Mod. Opt. **40,** 723–732 (1993).
8. S. M. Sze, *VLSI Technology* (McGraw-Hill, New York, 1988), Chap. 6, pp. 260–262.
9. H. Dammann and K. Gortler, "High efficiency in-line multiple imaging by means of multiple phase holograms," Opt. Commun. **3,** 312–315 (1971).
10. M. R. Taghizadeh, J. I. B. Wilson, J. Turunen, A. Vasara, and J. Westerholm, "Amorphous silicon nitride optical grating beam splitters," J. Non-Cryst. Solids **115,** 165–167 (1989).
11. J. Turunen, A. Vasara, S. Westerholm, G. Jin, and A. Salin, "Optimization and fabrication of grating beam splitters," J. Phys. D **21,** 102–105 (1988).
12. U. Krackhardt, J. N. Mait, and N. Streibl, "Upper bound on the diffraction efficiency of phase-only fanout elements," Appl. Opt. **31,** 27–37 (1992).
13. A. Vasara, M. R. Taghizadeh, J. Turunen, J. Westerholm, E. Noponen, H. Ichikawa, J. M. Millar, J. Jaakkola, and S. Kuisma, "Binary surface-relief gratings for array illumination in digital optics," Appl. Opt. **31,** 3320–3336 (1993).
14. M. P. Dames, R. J. Dowlings, P. McKee, and D. Wood, "Efficient optical elements to generate intensity weighted spot arrays: design and fabrication," Appl. Opt. **30,** 2685–2691 (1991).